Department of Precision and Microsystems Engineering

Linear induction machines for planar positioning

T.H.E. Scheepers

Report no : MSD 2017.008
Coach : ir. J.W. Spronck
Professor : Prof. dr. ir. J.L. Herder
Specialisation : Mechatronic System Design
Type of report : Master Thesis
Date : 9 March 2017

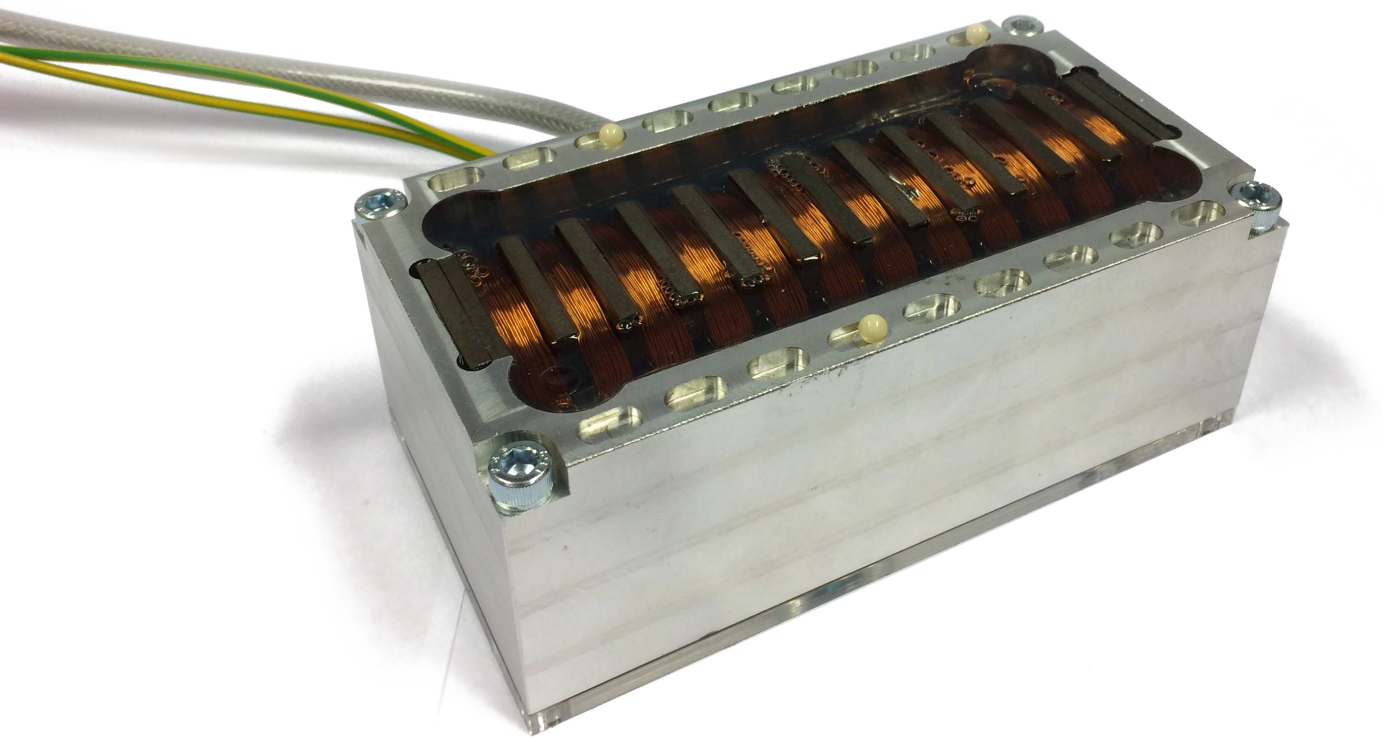

TU Delft Delft University of Technology

Challenge the future

Linear induction machines for planar positioning

by

T.H.E. Scheepers

in partial fulfillment of the requirements for the degree of

Master of Science
in Mechanical Engineering

at the Delft University of Technology,
to be defended publicly on Tuesday March 9, 2017 at 13:45

Student number: 4115570
Thesis committee: Ir. J.W. Spronck, TU Delft, supervisor
Prof. Dr. Ir. J.L. Herder, TU Delft
Dr. Ir. J.F.L. Goosen, TU Delft

TU Delft

Preface

Over the past 12 months the work done during my thesis has taught me more than I could have ever expected at the start. The project turned out to cover many fields that are only partly described by the classical definition of mechanical engineering. And would have been a far more cumbersome road without the great Mechatronic System Design group at the Delft University of Technology. Hereby I present the results of my year long research, made possible by a great group of people that have supported me throughout.

First and foremost I would like to thank my supervisor Jo Spronck, for all the support and freedom given to me throughout the project. Our weekly meetings often lasting way too long and covering lessons both on life and engineering. Ron van Ostayen, Hassan HosseinNia and Henk Polinder for their feedback and advise in their respective field of expertise being mechatonic systems, control and electrical drives. And Chetan Kumar for his advise on the real-time embedded system.

Also the rest of the faculty staff Rob Lutjeboer, Harry Jansen, Patrick van Holst and Jos van Driel for making the mechatronics lab a true engineering paradise, with all the equipment one could wish for. Gerard van Vliet, Rene van Ommen and Wim for their great advise on matters related to machining and manufacturing.

Also the great group of fellow students and researchers that form an amazing team that has solved challenges in a single coffee break that would have taken me days on my own. Thank you Bart, Bas, Gijs, Joost, Len, Martijn, Niranjan, Raoul and Stefan.

Finally I would like to thank my family, friends and girlfriend for supporting me both during this last year as well as the years preceding it and I hope to return all the love and patience they have had for me during the project.

T.H.E. Scheepers
Delft, February 2017

Abstract

This master thesis is a feasibility study of the use of linear induction machines as direct drive actuation method for planar positioning stages. The inherent benefits of a linear induction machine as being cogging free, having a position independent thrust and low moving mass, are extremely valuable for applications of planar positioning.

The lack of cogging and direct drive actuation allow for precise positioning. The position independent thrust allows to combine multiple machines for multi degree of freedom actuation, without the need to describe complex cross-coupling. And finally the low moving-mass allows for higher positioning speeds and bandwidths with respect to thrust.

Over the years many (planar) positioning stages have been built in our department of mechatronic system design at the Delft University of Technology. All the stages have been developed based on the linear Lorentz actuators. During discussions with my supervisor Jo Spronck an actuation method based on the use of eddy-currents was opted. The inherent dynamic physical principle by which thrust is generated, was something the department up to now had no experience with. The choice was made to investigate what could be achieved applying this actuation method to our inhouse knowledge of positioning stages.

Linear induction machines are a type of electromagnetic actuator that rely on induced eddy currents in the rotor to develop a resulting force between the stator and the rotor. A moving electrical field causes a moving magnetic field that in turn induces currents in the rotor of the machine. It is the Lorentz force that these currents undergo in the remaining magnetic field that produces thrust as in a rotational induction machine.

A thorough study is done on the current state of the art on linear induction machines. Based on this a description is given of the physical principles and particularities of linear induction machines. The theory of linear induction machines is developed into a set of three different models to describe such an actuator. All of which will serve a purpose in the development of the machine and its control.

First is a one dimension (1D) analytical model based on a field based approach, revealing the effects the design parameters have on the performance of the machine. The analytical model will also provide insight into the longitudinal end-effects, that are inherent non-linear effects, found in linear induction machines.

Second is a numerical finite element analysis (FEA) that reveals a more detailed analysis of the machine. It is used to verify the assumptions made in the derivation of the analytical model. Hereafter it is further developed to describe effects neglected in the analytical model. It is this model that will be used to design the induction machine used in the experimental set-ups.

Third is a lumped model based on equivalent circuit theory, this simplified model is used to develop the control strategy. The simple nature of the lumped model allows for it to be implemented on the real-time embedded microcontroller.

The main part of the thesis is focused on the design and implementation of all the components of a single degree of freedom (DOF) linear induction machine. To verify the predicted behavior of the machine a set of two complementing experimental setups have been built to verify the performance for both a static rotor and a dynamic rotor.

The geometric design of the linear induction machine will be developed using both insight gained from the analytical model and a sensitivity study based on the 2D FEA model. Finally a verification is done of the machine performance using a set of three linear amplifiers. The verification shows a good fit of the machine performance to the predicted behavior of the numerical model (up to 1.75 N of thrust). The predictive design approach can therefore be described as successful.

To allow implementation of a state of the art control scheme, the drive electronics will have to allow accurate control and sensing of the phase currents. The choice is made to develop this on a low-cost embedded microcontroller in combination with a switching three phase inverter, as to obtain a stand alone system. The use of stock power electronics will be described as well as the timing issues and conversions to the discrete

digital domain. A component level model is made of drive electronics that in combination with the lumped machine model can be used to simulate the electronics behavior.

The possible control schemes and their advantages are discussed separately. After which the implemented field oriented control (FOC) scheme will be discussed in depth. The implementation of the FOC scheme on the real-time electronics is described and its performance verified using measurements.

A three phase current controller with a bandwidth of 170 Hz is implemented for use in the linear machine. The thrust controller is developed around this fast current loop in a cascaded fashion. The final position controller is then developed around the thrust loop in cascaded fashion. The predicted thrust ripple and saturation of the inverter, limit the positioning performance of the implemented controller to a position bandwidth of 1.5 Hz with a precision and repeatability of 0.35° 3σ (or equivalent translation of 0.63 mm 3σ).

Once the results of the single DOF actuator have been verified, a design synthesis of a full planar stage (3 DOF) using the developed actuator will be discussed. A detailed analysis of the kinematics is discussed with the cross-coupling of the uncontrolled degrees of freedom. Finally the proposed control strategy in the decoupled global coordinates is introduced.

Concluding the results are discussed of using a linear induction machine for planar positioning. Verified as a feasible actuation method, the advantages and disadvantages over other actuation methods are covered. Followed by a description of the kind of applications in which the trade-offs favour the linear induction machine as an actuation method.

The developed work contains all the necessary tools needed for a mechatronic design engineer to evaluate and possibly implement linear induction machines for use in planar positioning applications. Hereby offering an additional actuation method that is less restrictive in the range precision trade-off. An application in for instance the field of microscopy would allow one to perform precise inspection of large samples.

Nomenclature

Symbols

α^{-1}	Attenuation constant
δ	Phase lag of magnetic field
ϵ	Disturbance amplitude
μ	Magnetic permeability
ω	Angular velocity
σ	Electrical conductivity
τ	Pole-pitch
θ	Electrical phase angle
$\vec{\psi}_m$	Magnetic flux
$\vec{B}$	Magnetic field
$\vec{E}$	Electrical field
$\vec{F}$	Force
$\vec{I}$	Moment of inertia
$\vec{i}$	Current
$\vec{J}$	Current density
$\vec{M}_o$	Out-of-plane transformation matrix
$\vec{M}_p$	In-plane transformation matrix
$\vec{T}$	Torque
$\vec{u}$	Voltage
$\vec{v}$	Velocity
ζ	Damping ratio
a	Transformation factor
C	Capacitance
D	Machine depth
d	Duty cycle
d_1	Thickness of rotor conductor
d_2	Thickness of rotor backing
d_3	Thickness of stator core
f	Frequency
g	Effective air gap
j	Imaginary unit
K	Motor constant
k	Discrete time index
K_i	Integral gain
K_p	Proportional gain
L	Inductance
L	Machine length
l	Wire length of coil
m	Mass
n	Number of windings per coil
p	Number of pole-pairs
R	Resistance
r_o	Effective motor arm
s	Slip
T_s	Sample time
v_e	Synchronous velocity
v_s	Slip velocity
w	Coil width

Subscripts

$_0$	Reference value
$_{1,2,3}$	LIM number (Chapter 4)
$_{1,2}$	Entry end effect, Exit end effect (Chapter 2)
$_{A,B,C}$	Three phase coordinates
$_{d,q}$	Direct, Quadrature
$_{e,m}$	Electrical, Mechanical
$_{s,r}$	Stator, Rotor
$_{x,y,z}$	Cartesian coordinates

Superscripts

*	Reference signal
$\hat{}$	Estimated signal

Abbreviations

AC	Alternating Current
AD	Analog to Digital
ADC	Analog to Digital Converter
CPU	Central Processing Unit
DC	Direct Current
DLIM	Double-sided Linear Induction Machine
DOF	Degree Of Freedom
EMF	Electromotive Force
FEA	Finite Element Analysis
FOC	Field Oriented Control
LIM	Linear Induction Machine
MMF	Magnetomotive Force
PI	Proportional Integral
PID	Proportional Integral Derivative
PSU	Power Supply Unit
PWM	Pulse Width Modulation
SLIM	Single-sided Linear Induction Machine
SVPWM	Space Vector Pulse Width Modulation
TBCTR	Time Based Counter
TBPRD	Time Based Period

Contents

1 Introduction

1.1. Context

As the world around us evolves, so do the production processes that are responsible for the materialistic half. As many have predicted the current trend of automation will continue to change the production and assembly lines. In most cases this requires transportation of the part between various production, inspection and assembly stations. At the respective station the part is often required to maintain a specified position and/or orientation.

One prominent example from the high-tech industry that relies heavily on automation is the lithography industry. Lithography is the process that is used to develop chips on thin silicon substrates called wafers. The manufacturing process requires various coating, exposing and developing steps of a single wafer. The current process uses robotic handlers (Figure 1.1) to move the substrate between the various processes and has separate precise positioning stages at the various production stations.

Imagine an actuation method that could make the range-precision trade-off less restrictive. One could use the same actuation method for both handling and positioning.

Figure 1.1: A conventional wafer handler by: Mechatronic systemtechnik gmbh.

1.2. Problem definition

In this thesis the focus will be put on the planar motions as they are found in production industry. This is a field that is highly dependent on the specific application at hand. In most cases however the desired performance raises similar problems. Below the most common performance criteria are listed and where necessary translated into engineering terms:

- Throughput → bandwidth $\propto \sqrt{\frac{\text{controlled stiffness}}{\text{moving mass}}}$
- Positioning → precision and/or accuracy
- Range
- Robustness/Cost → number of parts
- Breakage → stress concentration

Motion stages that work in-plane should have the ability to control all three of the degrees of freedom (DOF). This often makes the use of standard 1D linear/rotary actuation methods unpractical, as these would either have to be combined by a parallel mechanism or in cascaded fashion. A direct drive actuation method suitable for planar positioning is thus sought.

The actuation methods available to a mechatronic system designer to develop an application that needs position control of the in-plane DOF are limited. Depending on the application they are often constraint in either the precision or range. Applications that require both high precision and a large range are therefore often build using two complementing systems. The first allowing for coarse movement over a large range and a second stage to allow for a high precision around a specific location.

Within the Mechatronic System Design group a lot of research has been done on the development of state of the art microscopy stages. A microscopy stage for the inspection (high precision) of large areas (large range) requires the problematic combination of requirements stated above.

1.3. Existing solutions

There are various institutions that have investigated the challenges described above. The most high-tech examples of these arrive from research done in the lithography industry and universities around the world.

The use of magnetic levitation and actuation to actuate a mover filled with permanent magnets is one of the concepts often looked at. Figure 1.2a shows an example of such a design used in a US patent [2]. Other researches, at the Technical University of Eindhoven [19] and the Yonsei University in Korea [21] have investigated similar concepts.

Other concepts like the flowerbed (figure 1.2b) by the Technical university of Delft [43], work based on an air bearing that is modified as to provide a controlled thrust. This concept allows for direct actuation of thin substrates without the need of a mover.

A concept that can only control the planar translations is the Sawyer motor [35]. This is a type of switchable reluctance actuator that has been further investigated for use in for instance machining [39].

As of late concepts using linear induction machines have also gained renewed interest. Research has been done on specific applications [42] (marine hull inspection) and specific forms of actuator [9, 13, 23].

Little however has been written on the general consideration and trade-offs to be made using linear induction machines for planar positioning. The theory developed to describe the physical phenomena inside linear induction machines is plentiful, application to the design process is however sparse.

1.4. Proposal

The use of linear induction machines (LIM) as actuation method for planar positioning stages is proposed. The LIM has many inherent benefits for applications in planar positioning as being cogging free, a position independent thrust and low moving mass. The lack of moving parts and low-cost manufacturability have made its rotational equivalent the industries go-to standard in robust actuation.

The complexity of induction machines for positioning arises from the dynamic excitation that is necessary for the production of thrust. Recent developments in the control of induction machines however allow for a direct control of the thrust produced by the machine.

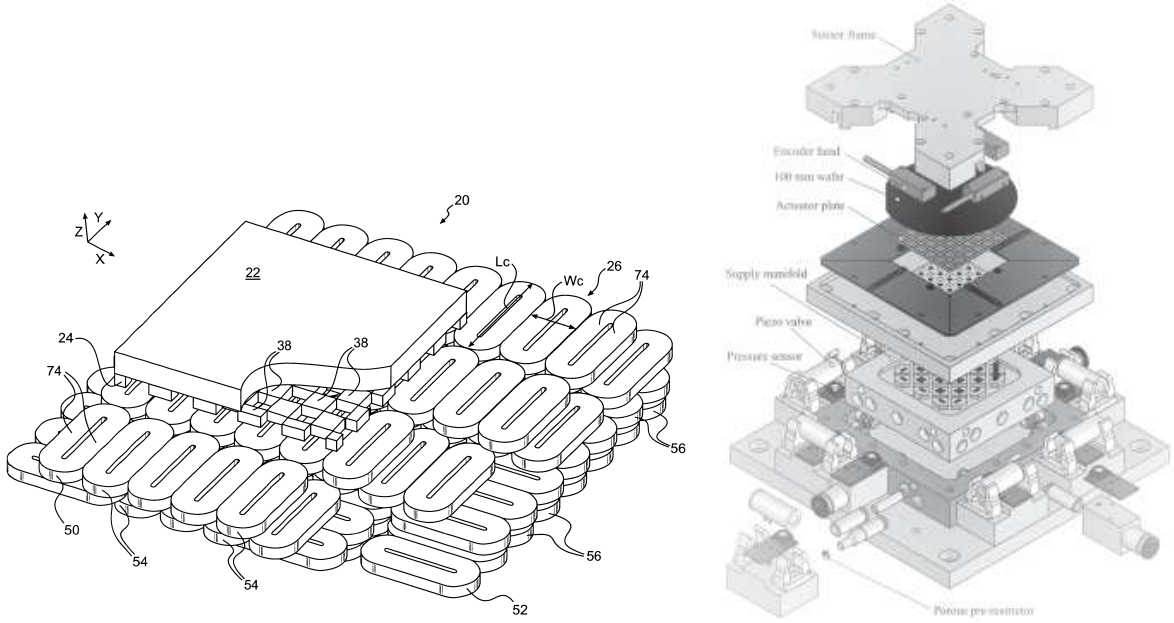

(a) Patent detailing the workings of a planar stage based on an array of coil to actuate the mover lined with permanent magnets [2]

(b) Flowerbed stage concept, actively controlled air-bearing that allows direct planar actuation of a wafer [43]

Figure 1.2: State of the art planar stages developed for use in lithography

The development of the theory necessary to design a linear induction machine capable of positioning will be given in this thesis. Based on which a design approach for linear induction machines, for use in planar positioning stages, will be given. Followed by the embodiment in a physical system and verification of its performance with regard to the predictive models. The stand alone actuator will finally be used to perform the synthesis of a planar 3 DOF positioning stage.

With this the thesis should result in a description of the necessary theory and design considerations to design and implement linear induction machine for planar positioning. The verified approach will form both the groundwork for further research into linear induction machines at the Mechatronic System Design group as well as the tools needed for a mechatronic engineer to consider and possibly implement a LIM for use in planar positioning.

1.5. Research objective

The objective of this thesis is to perform a feasibility study of the use of linear induction machines as direct drive actuation method for planar positioning stages. This can be subdivided in the following sub objectives:

- Development of linear induction machine theory
- Actuator design, implementation and verification
- Synthesis of full planar (3 DOF) stage

1.6. Thesis outline

The thesis is structured into five chapters. Following this introduction the second chapter will cover an introduction of the physical principles involved in induction actuation, the current state of research in the field and a set of models to describe linear induction machines. The third chapter will go into the detailed design of a linear induction machine and the experimental setups used for verification. The geometric, electronic and control design will be described, followed by the performance achieved. The forth chapter will cover the design synthesis of a planar microscopy stage using the previously described actuator. In the final chapter the results of the feasibility will be described and discussed together with possibilities for further research.

2

Introduction to linear induction machines

A linear induction machine is the linear equivalent of a rotary induction motor. This means it relies on the same physical principle to generate thrust. After covering the notation conventions, the physical principle will be introduced together with the end-effects specific to linear machines. Hereafter the current state of research will be covered followed by three different machine models that will be used to describe the linear induction machine.

2.1. Notation conventions

Below the notation conventions used throughout the thesis are given for the electrical and mechanical systems and an introduction will be given to the space vector description used throughout.

2.1.1. Electrical

The electrical systems will be described by their instantaneous voltage and current described by respectively u and i. The electrical power dissipated in the system, $p_e = u \cdot i$, is described by positive power ($p_e \geq 0$). Figure 2.1 depicts the electrical conventions that will be used for the ideal electrical components.

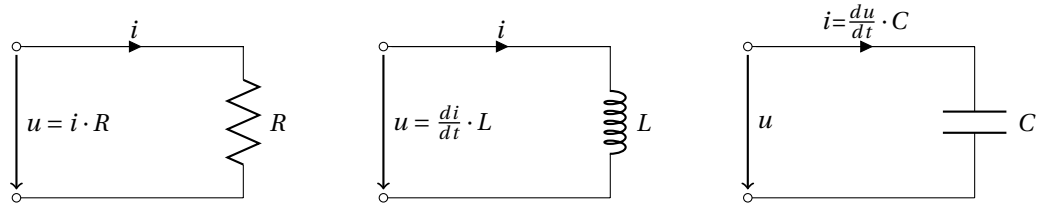

(a) Ideal transistor (b) Ideal inductance (c) Ideal capacitor

Figure 2.1: Electrical convention used for ideal electrical components

2.1.2. Mechanical

Similar conventions are used for the mechanical components of the system being described by either a moving or revolving mass with a mechanical load working on it. Here the power delivered to the external load ($p_l = F_l \cdot v$, $p_l = T_l \cdot \omega_m$) is considered positive (figure 2.2). Under the assumption that the winding and bearing losses can be neglected, one can now describe either the linear or rotational acceleration using (2.1) and (2.2).

$$\dot{v} = \frac{F_e - F_l}{m} \tag{2.1}$$

$$\dot{\omega}_m = \frac{T_e - T_l}{I} \tag{2.2}$$

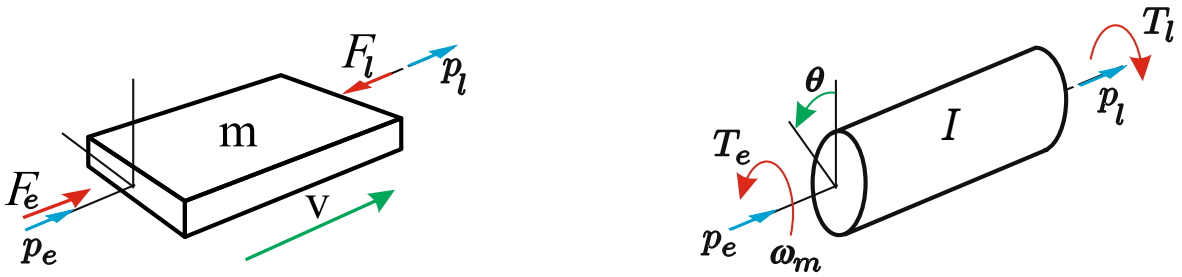

(a) Translating mass

(b) Rotating mass

Figure 2.2: Mechanical conventions used to describe a moving mass

2.1.3. Space vector

To describe various time-harmonic variables the use of space vectors is used. This is a phasor-like notation with an absolute description of the vectors phase. Unless stated otherwise the space vectors rotate in time in accordance with the electrical frequency (ω_e).

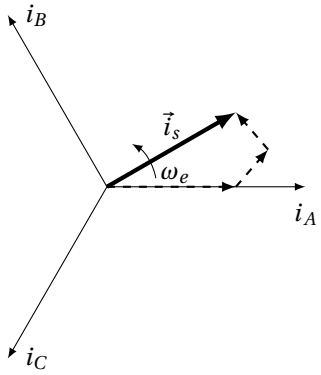

Figure 2.3: Example of space vector notation of the stator current vector ($\vec{i}_s$) with respect to the stationary phase vectors

Figure 2.3 gives an example of the time-harmonic stator current depicted as a space vector. In a rotational induction motor with a single pole-pair (figure 2.4a) one can simply overlay this description on the mechanical model. Throughout the thesis the same description will also be used for linear machines where one can translate between the electrical phase angle (θ) and the linear coordinate x using (2.3).

$$x(\theta) = x_0 + \frac{\theta \cdot \tau}{\pi} \tag{2.3}$$

Here x_0, τ respectively represent the x coordinate aligned with $\theta = 0$ and the machines pole-pitch. A variable represented by a space vector in a linear machine will thus represent a traveling wave along the machines length.

2.2. Physical principle

The thrust generating principle of an induction machine is based on Lorenz forces that work on the induced currents in the rotor. Similar to the rotational equivalent described below. Hereafter an introduction to the peculiarities of linear induction machines is given.

2.2.1. Rotational induction machines

Rotational induction machines are comprised of a stationary stator and a rotating part called the rotor. Stator coils are divided into several phases. Combined these can generate a current vector ($\vec{i}_s$) with a certain orientation and amplitude.

Rotation of the stator current vector results in a magnetic flux vector ($\vec{\psi}_m$) and an induced current vector in the rotor ($\vec{i}_r$). As can be seen in figure 2.4a the rotor current and the magnetic flux have a phase offset to

one another. It is this phase difference that results in torque proportional to the vector product (2.4) (figure 2.4b).

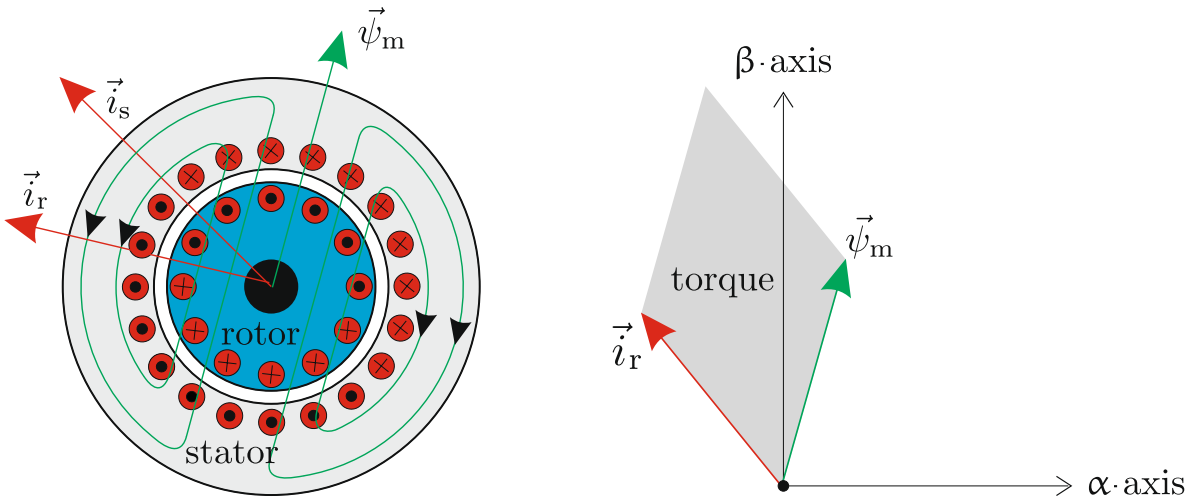

(a) Section of a single pole-pair rotational induction machine, one can see the induced rotor currents and magnetic flux due to the stator current

(b) Torque producing components in an induction machine, one can see maximal torque is obtained if the rotor current and magnetic flux are perpendicular

Figure 2.4: Rotational induction machine and torque producing principle [8]

$$\vec{T}_e = \vec{\psi}_m \times \vec{i}_r \tag{2.4}$$

A more detailed insight in the behavior will be covered in the various models described later this chapter.

2.2.2. Linear machine peculiarities

A linear machine is typically thought of as an unrolled version of its rotational equivalent. Figure 2.5 depicts a rotational machine with its linear counterpart. The biggest and most obvious difference being that the linear machine is no longer axisymmetric.

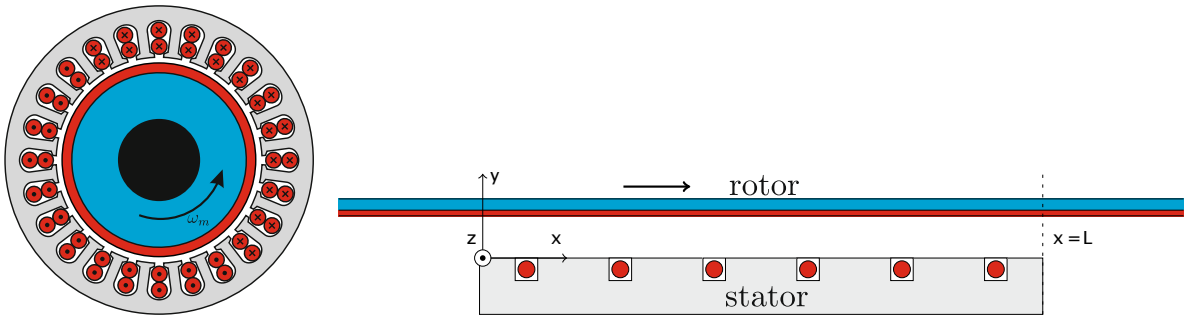

(a) Rotational induction machine [8] (b) Linear induction machine

Figure 2.5: Comparison of rotational versus linear induction machines. A linear induction machine can be described as the unrolled version of a rotational induction machine

Linear induction machines can due to their linear design be designed in two flavors. The so called double sided linear induction machine (DLIM) has two stators with a rotor in between. In this thesis the focus will be put on the single sided linear induction machines (SLIM), the principles and models can however easily be converted to represent the DLIM configuration. As can be seen in figure 2.5b a SLIM uses a magnetic backing on the rotor to reduce the magnetic reluctance and increase the magnetic field strength in the air gap.

The lack of axisymmetry of a LIM causes a noncontinuous electrical and in turn magnetic field. These effects can be divided into static and dynamic end-effects [37].

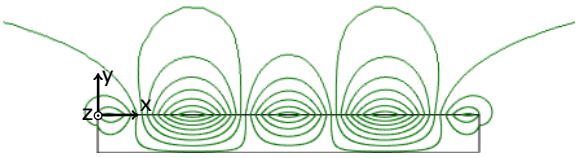

(a) Magnetic vector potential by the stator in free space

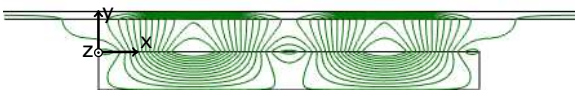

(b) Magnetic vector potential by the stator in the presence of an iron sheet

Figure 2.6: Magnetic out-of-plane vector potential. The addition of an iron sheet above the stator increases the magnetic field intensity within the air gap by reducing the reluctance path of the magnetic field

Static end-effects

The static effects are caused by the mere noncontinuous geometrical design of the linear machine. This causes a flux leakage to appear at the longitudinal ends that are not present in the rotational machine. These effects are present even for a static rotor and will therefore be called the static effects.

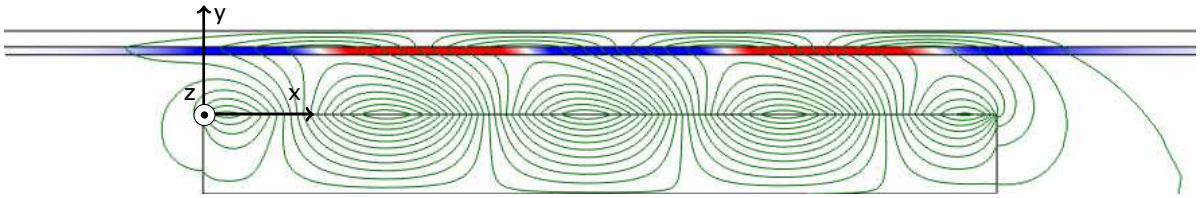

(a) Side view of a linear induction machine showing the induced current within the conducting sheet of the rotor with respect to the magnetic vector potential, $+J_z$ 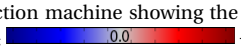 $-J_z$

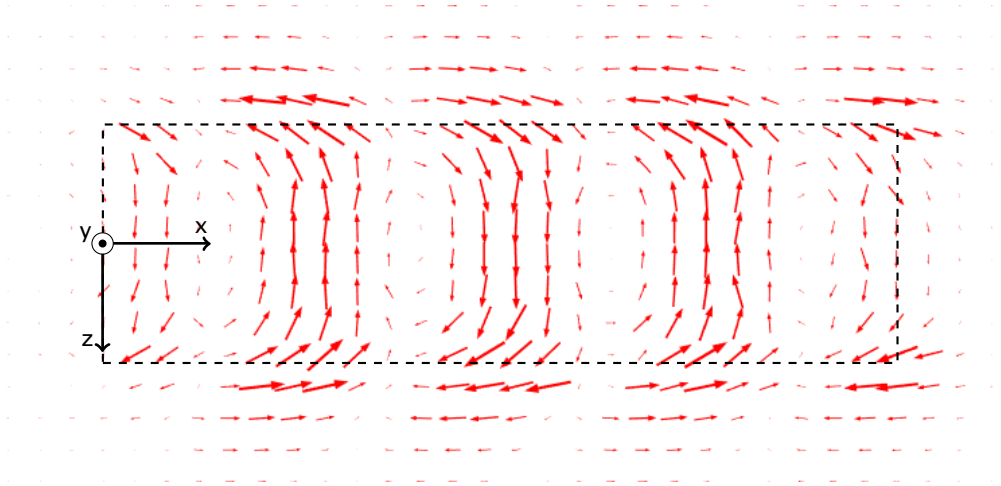

(b) Top view of the induced rotor currents, with a z-component above the stator and a return path along the x-direction in the overhang of the stator

Figure 2.7: Side and top view of the currents induced in the rotor due to the magnetic field of the stator

Further degradation of the linear fields is caused by the induced currents. As seen in figure 2.7a a rotor comprised of a conducting sheet will result in the generation of eddy-current within the conducting sheet. The induced currents in the rotor outside of the main magnetic field have a return path in the x-direction. This agrees with the principle of charge conservation (2.5), where ρ is the charge density and $\vec{J}$ the current density. Under the assumption the rotor charge remains unchanged, (2.5) simply states all current loops should be closed.

$$\frac{\partial \rho}{\partial t} + \nabla \vec{J} = 0 \tag{2.5}$$

The charge conservation however results in a degradation of the field that is different for the entering end effect ($x = 0$) and the exiting end effect ($x = L$). This is caused by the traveling magnetic field even if the rotor remains stationary. In figure 2.7a one can see more leakage of the magnetic field at the exiting-end than at the entering-end of the machine. Figure 2.7b depicts the path of the induced current within the rotor.

Dynamic end-effects

The dynamic end-effects are caused by the translation of the rotor with regard to the stator. The relative translation requires "new" material to be magnetized at the entry end of the linear induction motor. At the same time part of the induced rotor currents get moved out of the active area (figure 2.9). In figure 2.8 one can see the resulting degradation of the induced currents and thus thrust.

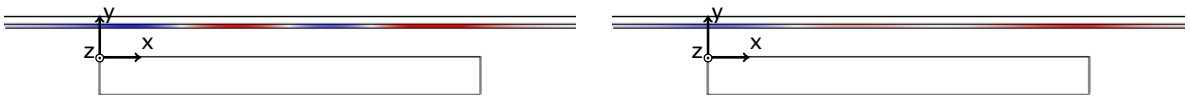

(a) Induced rotor currents for a static rotor

(b) Induced rotor currents for a moving rotor

Figure 2.8: Degradation of the induced rotor currents for a moving rotor versus a static rotor, $+J_z$  $-J_z$

These dynamic effects become more severe as the rotor velocity increases. This velocity dependent non-linearity further complicates the behavior of a linear machine with regard to a rotational machine. Figure 2.9 gives a graphical representation of the effects caused by the moving rotor. The "new" material entering the machine results in a degraded magnetic field at the entering-end while the induced currents moved out of the machine at the exiting-end results in increased flux leakage. The magnetic/current field is shifted with regard to the stator again the extend of which is dependent on the velocity of the rotor.

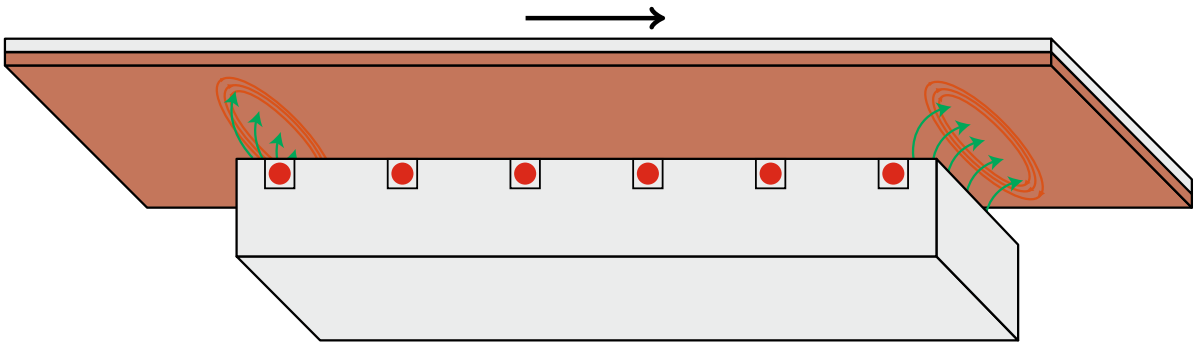

Figure 2.9: Dynamic end-effects due to movement of the rotor. One can see that at the entering-end the "new" material has traveled partially into the machine before it is fully magnetized. At the exiting-end the induced rotor currents are moved out of the stators reach

2.3. State of the art

Research on linear induction machines dates back as far as the 1840s, by Charles Wheatstone. It was however first made popular by Eric Laithwaite in the 1940s with his work on a maglev application that was later dubbed the magnetic river. Since, a lot of research has been done on the various aspects of the linear induction machines. One can divide the research into three categories: modeling, design and control. Below the various topics and stages of research will be covered.

2.3.1. Modeling

A lot of research has been focused on the development of models to describe the peculiarities of a linear induction machine and the verification using empirical data. A variety of different approaches have been

pursued to develop models both analytically and numerically.

The developed analytical models describe the magnetic field inside the motor using either space harmonics, Fourier series models or Fourier transform models. The initial description was first introduced in the work of S. Yamamura [44] and E.R. Laithwaite [25]. The models were further developed using Fourier domain descriptions as for instance in [12] and [30]. A comparative study of the various descriptions shows similar predictive performance of the models [6].

The description of the LIM's behavior as a lumped model in the form of an equivalent circuit has also received great attention in research. Here the model first described by Duncan [11] is still used by many in the field. Although in recent years the use of numerical models is often used to determine the lumped parameters [27].

Although the use of numerical models lacks the basic insight in how various elements of the system contribute to the motor performance, the high accuracy of the numerical simulations have caused them to dominate current day research.

2.3.2. Design

The design of linear induction motors has mainly been focused on the development for high speed transportation systems designed for a pure 1D translation. The development of which has even resulted in compensation techniques for the dominant entering end-effect at high speeds [15]. Development of general design rules for use in an application as a positioning stage are however sparse.

Laithwaite covers a couple general design perspectives [24] that highlight some of the exotic motor designs possible and first mentions other uses than transport systems. Other research focuses on the general optimization techniques that best fit the optimization of LIM parameters using numerical models [38]. In recent years a couple of projects have surfaced on the investigation of linear induction machines that could be used for planar positioning.

The work by N. Fujii [14] on the development of a two dimensional planar induction motor is especially interesting. The investigation of a circular stator that is excited using a set of variable frequency drives. As well as another 2D induction motor developed for ship hull surface inspection [41] that also uses a stator design that combines two linear induction machines into a single 2D actuator.

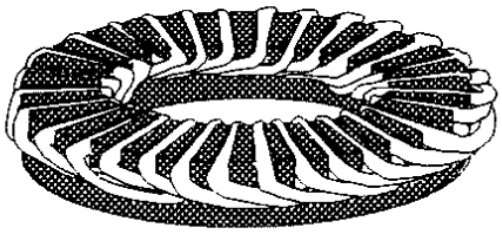

(a) 2DOF planar induction machine based on a circular stator [14], excitation by two variable frequency drives allows for either rotation or translation in a single direction

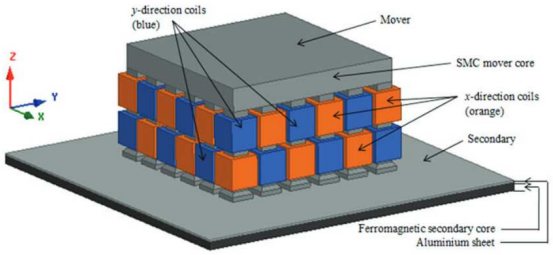

(b) 2DOF planar induction motor for surface inspection of ship hulls [41], a single stator is used for the windings of two linear induction machines

Figure 2.10: Planar induction machines assembled into single stator design

Finally there have been two groups that have investigated the use of multiple linear induction machines for planar actuation. P. Dittrich investigated the use of four two phase linear induction motors to obtain planar movement [9]. And finally the most recent development has been by M. Kumagai [23] in the development of a planar motor comprised of three linear induction machines as depicted in figure 2.11b.

2.3.3. Control

Finally the research covering the control strategies will be discussed. The general control schemes used for linear induction machines are extremely simple considering only a feed forward AC excitation scheme. Research on rotational induction machines has however resulted in field oriented control schemes that are considered far superior over the former forms of feed-forward scalar control.

Research on linear induction machines describes the use of these field oriented control (FOC) strategies to obtain increased dynamic behavior, an example of which is the previously described planar actuator shown

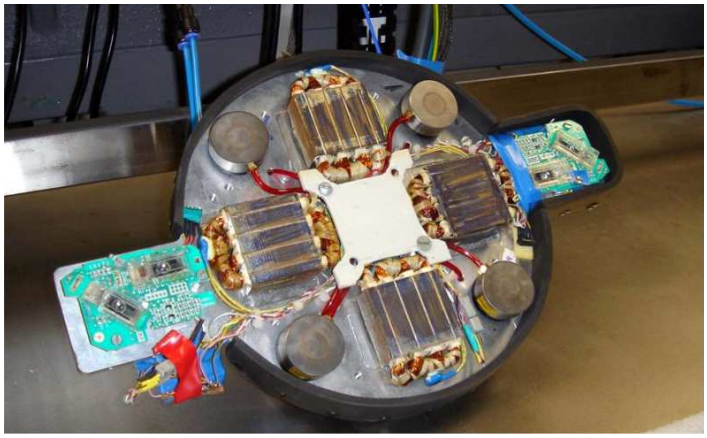

(a) Planar actuator comprised of four 2 phase linear induction motors [9]

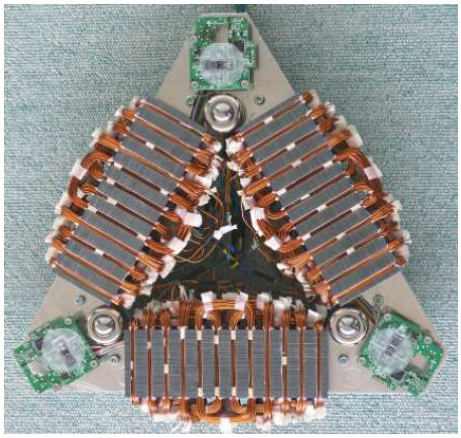

(b) Planar actuator using 3 linear induction motors [23]

Figure 2.11: Planar actuators composed of an array of linear induction machines to control the planar degrees of freedom

in figure 2.11b and research aimed at the development of a LIM based aircraft launch system [20]. In these cases the theory developed for rotational machines is directly applied to the linear machines although recent research has tried to incorporate the end-effects of the linear machine into the FOC scheme [33].

2.4. Machine models

To develop a thorough understanding of the behavior of a linear induction machine and how the various machine parameters influence the behavior, a set of models are developed in this section. Below first an introduction will be given to the surface current description used to model the stator windings in some of the models.

The analytical model will be developed using a 1D field based method first described by S. Yamamura [44]. The insight gathered here gives a detailed description of the physical principles involved. Following this a more accurate numerical finite element analysis is performed to describe the effects neglected in the analytical model. Finally a lumped parameter model in the form of an equivalent circuit will be given to describe the general behavior. It is this simplified model that will later be used in the real-time embedded control scheme.

2.4.1. Surface current description

A simplified representation of the current distributions is described for use during modeling. A surface current can be described as an infinitely thin conducting sheet, through which a continuous current density ($\vec{J}$) can be described in the plane.

As seen before (figure 2.4b) a linear induction motor in practice is built using a set of stator coils. Most often used in practice are stator coils that are divided into three 120° electrically spaced phases (here referred to as A, B and C). Using these three time-harmonic phase currents (3.27) one can represent the stator current vector $\vec{i}_s$.

$$i_A = i_s \cdot e^{j\cdot\omega_e\cdot t}, \qquad i_B = i_s \cdot e^{j\cdot(\omega_e\cdot t+\frac{2}{3}\pi)}, \qquad i_C = i_s \cdot e^{j\cdot(\omega\cdot t+\frac{4}{3}\pi)} \tag{2.6}$$

The stator current vector will rotate with the same electrical frequency as the separate stator phase currents. The spacial distribution of the stator phase angle is determined by the pole-pitch and can be used to compute the placement of the stator coils using (2.7).

$$x_A(n) = x_0 + (n-1)\cdot\tau, \qquad x_B(n) = x_0 + \left(n-\frac{2}{3}\right)\cdot\tau, \qquad x_C(n) = x_0 + \left(n-\frac{1}{3}\right)\cdot\tau \tag{2.7}$$

With n ranging from 1 to $2p$, p being the number of pole-pairs. The non-linear spatial distribution of

the stator current is often simplified using the surface current description. The stator current above will thus describe a continuous current density with an amplitude of $J_0 = \frac{3 \cdot i_s}{\tau}$.

$$\vec{J}_s = \frac{3 \cdot i_s}{\tau} \cdot e^{j \cdot (\omega_e \cdot t - \frac{\pi}{\tau} \cdot x)} \cdot \vec{e}_z \tag{2.8}$$

As seen the current density can be described as a traveling wave along the length of the machine (the offset x_0 is from hereon ignored for readability). Note only a z-component is present in the current density vector.

2.4.2. Field based analytical model

The analytical model is derived for one dimension, an approximation valid for machines with an effective air-gap (g) that is small with regard to the pole-pitch (τ). Below the model will first be solved for a continuous machine (infinitely long) followed by the description of the longitudinal end-effects in a LIM.

Continuous model

The continuous model of a LIM is depicted in figure 2.23. Here the iron backing and stator core are shown with a coarse hatch and the dense hatch is used to illustrate the conducting current sheets from the previous section.

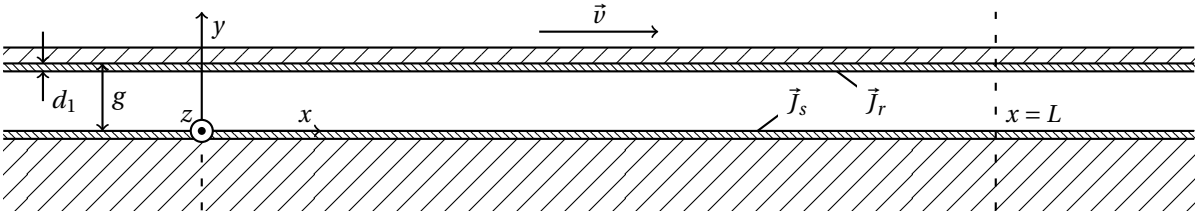

Figure 2.12: Side view of a model of a continuous (infinitely long) linear induction machine, conductors are represented by two respective current sheets

All the currents are assumed to be in the z-direction only and the magnetic field ($\vec{B}$) is assumed to have only a y-component in the air gap. These assumptions reduce the Maxwell-Faraday equation as shown in (2.9) and the Ampère's law as shown in (2.10).

$$\nabla \times \vec{E} = -\frac{\partial \vec{B}}{\partial t} \qquad \frac{dE_z}{dx} = \frac{dB_y}{dt} \tag{2.9}$$

$$\nabla \times \vec{B} = \mu \cdot \vec{J} \qquad \frac{g}{\mu} \cdot \frac{dB_y}{dx} = J_{\mathrm{sz}} + J_{\mathrm{rz}} \tag{2.10}$$

Here $\vec{E}$, μ are respective electrical field and the magnetic permeability of the air gap (often taken as $\mu_0 = 4\pi \times 10^{-7}\,\mathrm{N/A^2}$). The rotor velocity is given by v and describes the relative velocity with regard to the stator. The current flowing through the rotor ($\vec{J}_{rz}$) is induced by the magnetic field and derived using (2.9) in proportion to the surface conductivity (2.11) according to Ohm's law (2.12). σ and d_1 respectively describe the conductivity and thickness of the conducting sheet in the rotor.

$$\sigma_r = \sigma \cdot d_1 \tag{2.11}$$

$$J_{\mathrm{rz}} = \sigma_r \cdot E_z \tag{2.12}$$

$$\frac{dJ_{\mathrm{rz}}}{dx} = \frac{dB_y}{dt} \cdot \sigma_r = \left(\frac{\partial B_y}{\partial t} + v \cdot \frac{\partial B_y}{\partial x} \right) \cdot \sigma_r \tag{2.13}$$

One can see from (2.13) that the induced current is both dependent on the differential of $\vec{B}$ as well as the spacial gradient times the rotor velocity. Now by differentiating (2.10) and substituting the just derived spatial gradient of the rotor current (2.13), one obtains the following equation describing the continuous model.

$$\frac{g}{\mu}\cdot\frac{d^2B_y}{dx^2}-\sigma_r\cdot\frac{\partial B_y}{\partial t}-\sigma_r\cdot v\cdot\frac{dB_y}{dx}=\frac{dJ_{sz}}{dx} \tag{2.14}$$

Using the harmonic current sheet description of the stator current as given in (2.8) one can assume the solution for the magnetic field (2.15) to be of the same shape varying only in amplitude $\vec{B_0}$ and phase δ.

$$B_p = B_0\cdot e^{j\cdot(\omega_e\cdot t-\frac{\pi}{\tau}\cdot x+\delta)} \tag{2.15}$$

$$\frac{dB_p}{dx} = -j\cdot\frac{\pi}{\tau}\cdot B_0\cdot e^{j\cdot(\omega_e\cdot t-\frac{\pi}{\tau}\cdot x+\delta)} \tag{2.16}$$

$$\frac{d^2B_p}{dx^2} = -\left(\frac{\pi}{\tau}\right)^2\cdot B_0\cdot e^{j\cdot(\omega_e\cdot t-\frac{\pi}{\tau}\cdot x+\delta)} \tag{2.17}$$

$$\frac{\partial B_p}{\partial t} = j\cdot\omega_e\cdot B_0\cdot e^{j\cdot(\omega_e\cdot t-\frac{\pi}{\tau}\cdot x+\delta)} \tag{2.18}$$

Computing the various derivatives of our assumed magnetic field and substituting them into (2.14) results in both the space and time dependent variables to fall away. The resulting equation is given in (2.19). Where v_e is the synchronous speed given by: $v_e=\frac{\omega_e\cdot\tau}{\pi}$.

$$\frac{j\cdot\pi\cdot B_0\cdot g}{\tau\cdot\mu}\cdot e^{j\cdot\delta}-B_0\cdot\sigma_r\cdot(v_s-v)\cdot e^{j\cdot\delta}=J_0 \tag{2.19}$$

One can solve equation (2.19) by solving it for both the real (B_0) and complex (δ) part of the magnetic field. This results in the solutions shown below.

$$B_0 = \frac{J_0}{\sqrt{\left(\frac{\pi\cdot g}{\tau\cdot\mu}\right)^2+(\sigma_r\cdot(v_s-v))^2}} \tag{2.20}$$

$$\delta = \tan^{-1}\cdot\left(\frac{-\pi\cdot g}{\tau\cdot\mu\cdot\sigma_r\cdot(v_s-v)}\right) \tag{2.21}$$

One can now for a certain harmonic stator current excitation derive the state of the continuous linear induction machine. Computing the integral over the length of the machine of the thrust as described in (2.4). The instantaneous thrust has a harmonic component of twice the electrical frequency. The time average thrust produced by the machine is described using (2.22), where $\overline{B_p}$ is the complex conjugate of B_p [16, 29]. Note that the total thrust is distributed over an area proportional to the length and depth of the stator. The stress concentrations in the rotor are thus reduced significantly over other actuation methods.

$$F_x = -D\int_0^L 0.5\cdot\mathrm{Re}(J_{rz}\overline{B_p})dx \tag{2.22}$$

One can substitute the terms in (2.22) with the previously determined values to determine the average thrust working on the rotor. This results in (2.23) where D is the depth of the stator and L the length of the stator.

$$F_x = \frac{J_0\cdot B_0\cdot D\cdot L}{2}\cdot\cos(\delta) \tag{2.23}$$

Using the machine parameters (appendix A) of the actuator developed later in this thesis, one can depict the thrust with respect to slip ($s=\frac{v_e-v}{v_e}=\frac{\omega_e-\omega_m}{\omega_e}$). This matches the known behavior of a rotational induction machine.

A description that makes more sense for a linear machine is to plot the generated thrust with regard to the slip velocity ($v_s=v_e-v$). This is the velocity of the traveling magnetic field wave with respect to the rotor. As seen later in figure 2.13 this results in a measure that is independent of the rotor velocity.

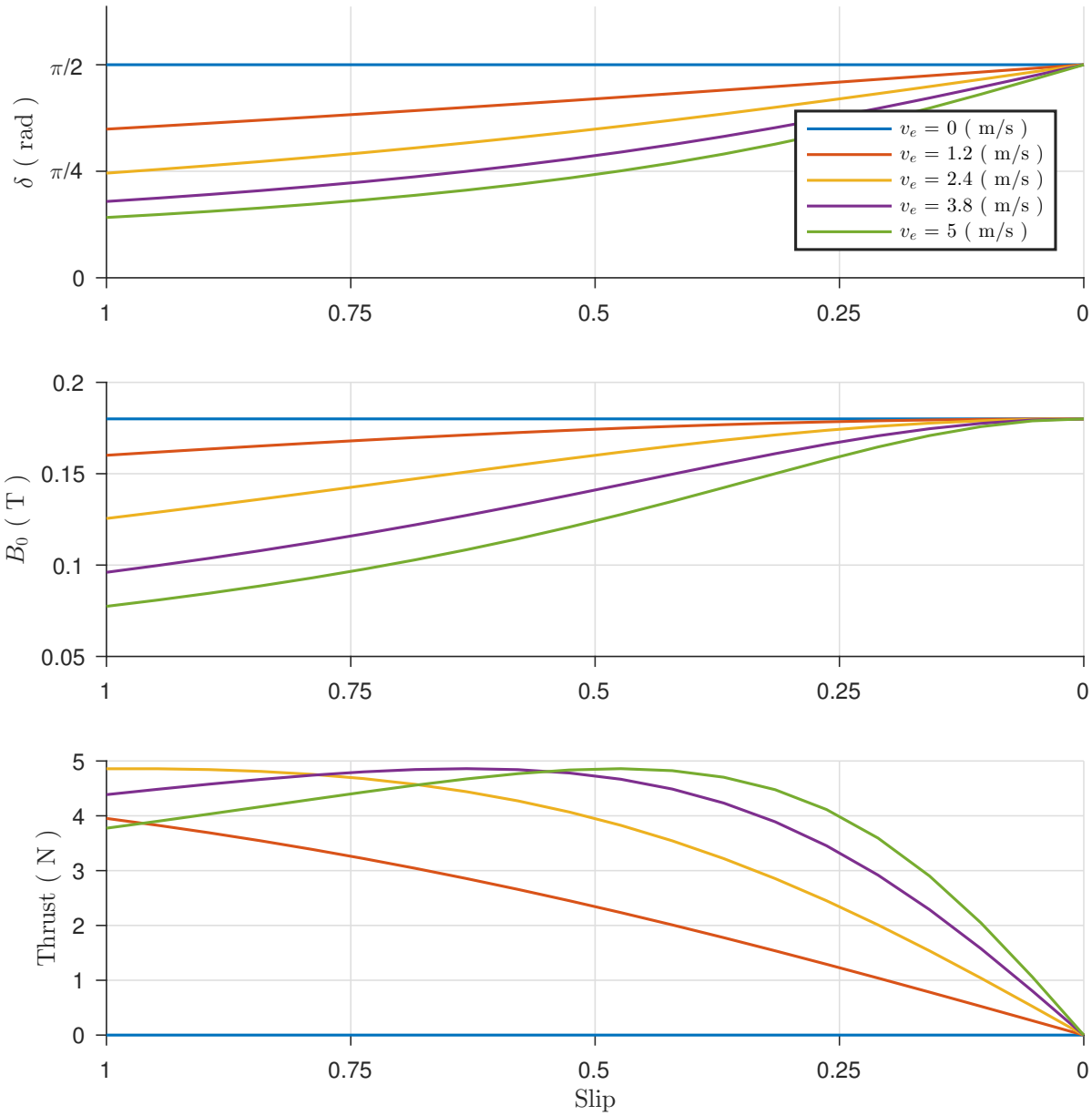

Figure 2.13: Continuous machine behavior with regard to slip for various synchronous speeds, δ gives the phase lag of the magnetic field with regard to the current excitation, B_0 gives the amplitude of the magnetic field in the air gap

Note that next to ignoring the significant end-effects present in the LIM the model is based on a couple of other assumptions: the magnetic field can be regarded to have only a y-component in the air gap. Furthermore the stator current distribution is assumed to be perfectly distributed in space. And finally the material properties are considered linear and ideal, meaning the rotor backing and iron core are considered to have an infinite magnetic permeability, are non-conducting and are non-saturating.

Finite length model

The model described in the previous section can be extended to incorporate the finite length of the machine and the hereby introduced longitudinal end-effects. This is done by first setting the right side to zero and solving the homogeneous equation.

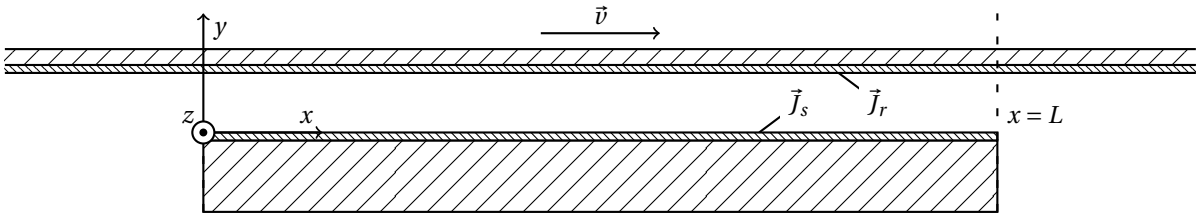

Figure 2.14: Side view of the model of a linear induction machine of finite length, conductors are described by two current sheets

$$\frac{g}{\mu}\cdot\frac{d^2B_y}{dx^2}-\sigma_r\cdot\frac{\partial B_y}{\partial t}-\sigma_r\cdot v\cdot\frac{dB_y}{dx}=0 \tag{2.24}$$

Because the homogeneous equation is a function of both space and time the theory of separation of variables will have to be applied. Therefore the homogeneous solution (B_h) will be defined as the product of the time dependent terms and the space dependent terms as depicted in (2.25).

$$B_h(x,t)=X(x)\cdot T(t) \tag{2.25}$$

One can then rewrite (2.24) and set both terms to be equal to a certain separation variable λ. Doing this allows one to solve both parts of the equation separately.

$$\left(\frac{g}{\mu\cdot\sigma_r}\cdot\frac{d^2X(x)}{dx^2}-v\cdot\frac{dX(x)}{dx}\right)\cdot\frac{1}{X(x)}=\frac{dT(t)}{dt}\cdot\frac{1}{T(t)} \tag{2.26}$$

$$\equiv\lambda \tag{2.27}$$

The more complex spacial equation will be solved first. Below one can see the separated equation and the solution for $X(x)$.

$$\frac{d^2X(x)}{dx^2}-\frac{\mu\cdot\sigma_r\cdot v}{g}\cdot\frac{dX(x)}{dx}-\frac{\mu\cdot\sigma_r\cdot\lambda}{g}\cdot X(x)=0 \tag{2.28}$$

$$r^2-\frac{\mu\cdot\sigma_r\cdot v}{g}\cdot r-\frac{\mu\cdot\sigma_r\cdot\lambda}{g}=0 \tag{2.29}$$

$$r_1,\ r_2=\frac{\mu\cdot\sigma_r\cdot v}{2\cdot g}\pm\sqrt{\left(\frac{\mu\cdot\sigma_r\cdot v}{2\cdot g}\right)^2-\frac{4\cdot\mu\cdot\sigma_r\cdot\lambda}{g}} \tag{2.30}$$

$$X(x)=C_1\cdot e^{r_1\cdot x}+C_2\cdot e^{r_2\cdot x} \tag{2.31}$$

The time dependent equation can also be solved in a similar manner. This derivation is depicted below.

$$\frac{dT(t)}{dt} - \lambda \cdot T(t) = 0 \tag{2.32}$$

$$T(t) = C_3 \cdot e^{\lambda \cdot t} \tag{2.33}$$

Combining the separated variables again using (2.25), the general homogeneous solution is given by the sum of all the solutions.

$$B_h = \sum_n \left\{ e^{\lambda_n \cdot t} \cdot \left(B_{n1} \cdot e^{r_{n1} \cdot x} + B_{n2} \cdot e^{r_{n2} \cdot x} \right) \right\} \tag{2.34}$$

Because the time dependent terms ($T(t)$) of the homogeneous solution are expected to be steady for steady operation of the motor, one can derive that λ_n should be pure imaginary. This in combination with the single harmonic excitation current allows for the following assumption of λ_n.

$$\lambda_n = \lambda = j \cdot \omega_e \tag{2.35}$$

Combining both the particular (2.15) and homogeneous equations and filling in (2.35) gives us the general solution of the magnetic field (2.36).

$$B_y = \underbrace{B_0 \cdot e^{j \cdot (\omega_e \cdot t - k \cdot x + \delta)}}_{B_p} + \underbrace{e^{j \cdot \omega_e \cdot t} \cdot \left(B_1 \cdot e^{r_1 \cdot x} + B_2 \cdot e^{r_2 \cdot x} \right)}_{B_h} \tag{2.36}$$

Here B_0 and δ are respectively given by (2.20) and (2.21). The r values of the particular solutions are given by (2.37). The remaining values of B_1 and B_2 are functions of time and have to be determined by the boundary conditions.

$$r_1,\ r_2 = \frac{\mu \cdot \sigma_r \cdot v}{2 \cdot g} \pm \sqrt{\left(\frac{\mu \cdot \sigma_r \cdot v}{2 \cdot g} \right)^2 - j \cdot \frac{4 \cdot \mu \cdot \sigma_r \cdot \omega_e}{g}} \tag{2.37}$$

Filling in (2.35) one can finally rewrite the solution into a simplified form using the substitution given in (2.38).

$$Y + jZ = \sqrt{\left(\frac{\mu \cdot \sigma_r \cdot v}{2 \cdot g} \right)^2 - j \cdot \frac{4 \cdot \mu \cdot \sigma_r \cdot \omega_e}{g}} \tag{2.38}$$

The final solution can then be written in the form shown below, with the rotor surface resistivity ($\rho_r = \sigma_r^{-1}$) [44]. S. Yamamura gives an analytical solution for B_1 and B_2, valid for certain assumed boundary conditions. The full derivation is not given here as the assumed boundary conditions hold poorly for low rotor velocities and thus not add to the understanding of the low velocity fields.

$$\alpha_1, \alpha_2 = \frac{2 \cdot \rho_r \cdot g}{\rho_r \cdot g \cdot Y \pm \mu \cdot v} \tag{2.39}$$

$$\tau_{1,2} = \frac{2\pi}{Z} \tag{2.40}$$

The description of the final magnetic field (2.41) reveals some valuable insight into the behavior of the longitudinal end-effects. As can be seen the field in the air-gap is composed out of three superimposed waves. The main wave is determined by the continuous motor model described earlier. The other two waves respectively represent the entrance and exit end-effect.

$$B_y = B_0 e^{j(\omega_e t - \frac{\pi}{\tau} x + \delta)} + B_1 e^{-\frac{x}{\alpha_1}} e^{j(\omega_e t - \frac{\pi}{\tau_{1,2}} x)} + B_2 e^{\frac{x}{\alpha_2}} e^{j(\omega_e t + \frac{\pi}{\tau_{1,2}} x)} \tag{2.41}$$

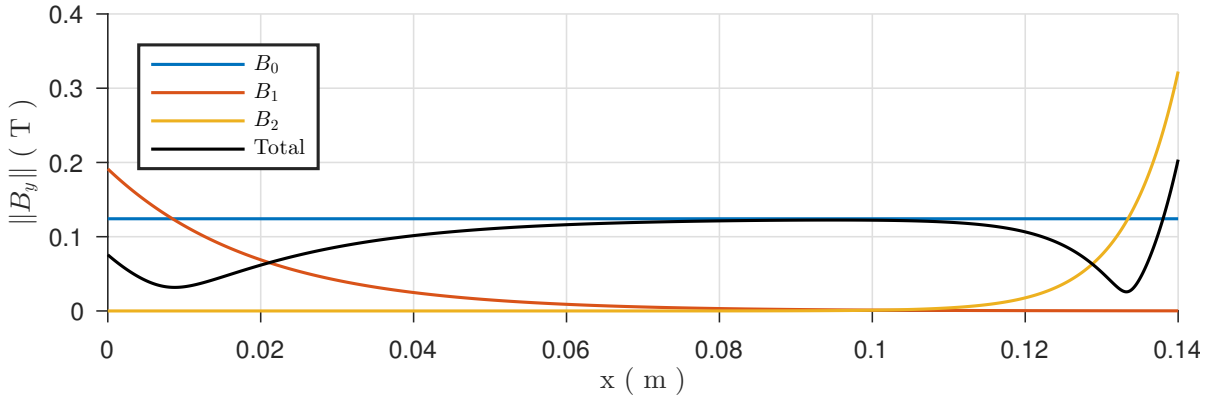

Figure 2.15: Magnitude of the three waves contributing to the magnetic field within the air gap, given for a rotor and slip velocity of both 2.5 m/s. One can see the constant magnetic field norm B_0 that was assumed in the continuous model and its degradation due to the end effects

The end-effect waves have a time dependent term that has the same frequency as the excitation frequency. The spacial velocities ($\frac{\omega_e \cdot \tau_{1,2}}{\pi}$) of the end-effects is however different for the continuous traveling wave (v_e). Found to be similar at high speeds the velocity of the end-effects are much higher than the rotor speed at low velocities [44].

Figure 2.15 shows the influence the end-effects have on the magnitude of the magnetic field in the air-gap. The effect of the entering end-effect can be seen to reduce, as it enters the motor, in accordance with the attenuation constant ($\frac{1}{\alpha_1}$). The exiting end-effect can too be interpreted as an attenuating wave entering from the other end of the machine.

The resultant field is overall smaller than for the model without end-effects and as such has degraded the thrust. Below (figure 2.16) one can see that the penetration of the entrance end-effect increases with the rotor velocity. One can also see that under rotor velocities, in the order of magnitude of a positioning stage, the end-effects are diminished after about twice the pole-pitch, independent of the total motor length.

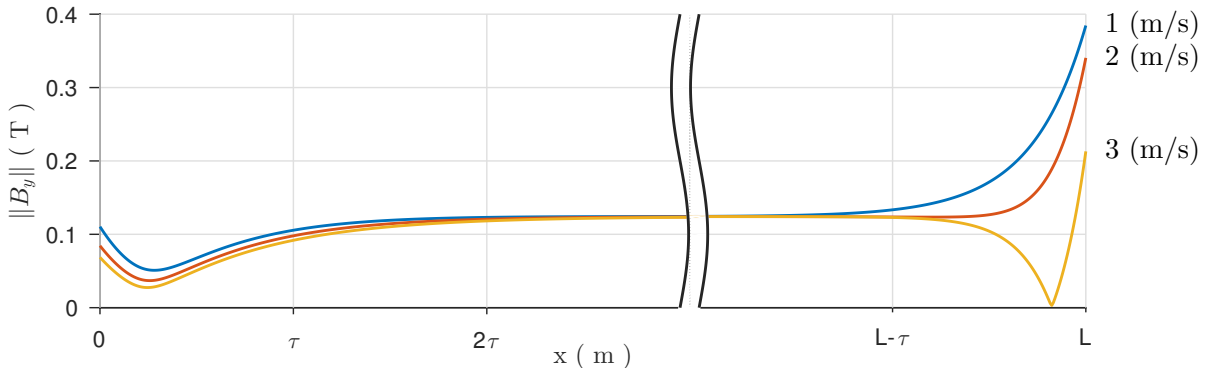

Figure 2.16: Spread of the end-effects visualized for various rotor velocities, given for a slip velocity of 2.5 m/s. One can see the end effects become more severe for higher rotor velocities. For velocities in the order of magnitude expected of a positioning stage the effects can be neglected after about twice the pole-pitch from either end

2.4.3. Finite element model

Next to the analytical model above the use of finite element analysis (FEA) to model the magnetic fields is used throughout this thesis. One can see that even for a 1D model an analytical description of the field quickly becomes cumbersome and heavily dependent on the assumptions made. The use of FEA allows for the incorporation of more of the physical phenomena present in a LIM. The trade-off being that the lack of an analytical solution removes the direct insight in the model sensitivity to various parameters.

Below the 2D FEA model of a single sided linear induction machine will be built following steps similar to that of the analytical model. This approach allows for verifying the models to one another. From there further development of the model is discussed. Modeling is done using the COMSOL Multiphysics simulation

software.

Continuous model

Similar to the analytical model one can initially develop a continuous model. The use of continuity boundary conditions result in a model that accurately describes the magnetic field of an infinitely long machine. Again initially the use of a current sheet description of the excitation current will be used.

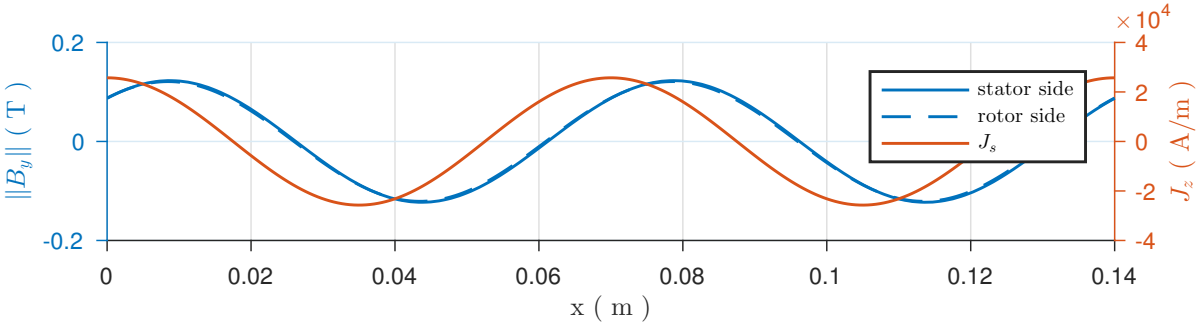

Figure 2.17: Magnetic field density (B_y) of continuous FEA model, for slip velocity of 2.5 m/s, both the field at the rotor and the stator side are depicted as well as the current sheet excitation

As can be seen in figure 2.17 the magnetic field in the air-gap indeed has a shape equal to that of the excitation current as was the assumption made in (2.15). Also visible is the fact that the vertical magnetic field component in the air gap shows little variation between the stator and rotor side. The 1D approximation of the magnetic field in the air gap can thus be considered a valid approximation (for small effective air gaps, $g \ll \tau$).

Further analysis of the magnetic field allows for comparison to the analytical model with respect to the slip velocity. Figure 2.18 shows there is a good match between both the 2D FEA model and its 1D analytical equivalent.

Finite length model

Removing the periodic boundary condition at either end of the model allows for a description of the boundary conditions assumed in the development of the analytical model. These state that there is no flux leakage outside of either end of the linear machine (2.42).

$$\int_0^L B_y dx = 0 \tag{2.42}$$

Figure 2.19 shows the magnitude of the magnetic flux within the air gap along the length of the machine. Both fields describe the same overall shape with high magnitudes at either end, induced by the boundary conditions applied.

The FEA model however allows for a correct description of these fields even for a stationary rotor. Using this the forces working on the rotor can be derived. Figure 2.20 shows how the motor thrust is reduced by the introduction of end-effects and rotor speed. Furthermore one can see that the slip velocity for which maximum thrust is achieved also increases with rotor velocity.

Longitudinal flux leakage

The assumption made for both the analytical models and the FEA model described above assume no flux leakage appears at either of the machine ends. A model that incorporates a more realistic description of the end-effects is depicted in figure 2.21.

The ends at $x = 0$ and $x = L$ are no longer considered the boundary for either the magnetic flux or the induced currents. The resulting magnetic field will therefore naturally flow outside of these boundaries, a phenomenon from now on called flux leakage.

Figure 2.22 shows the effect flux leakage has on the magnetic field strength along the length of the LIM. The flux leakage results in a stretching of the end-effects to outside of the LIM. Also note that the artificially high peaks in the magnetic flux described by the previous model are diminished.

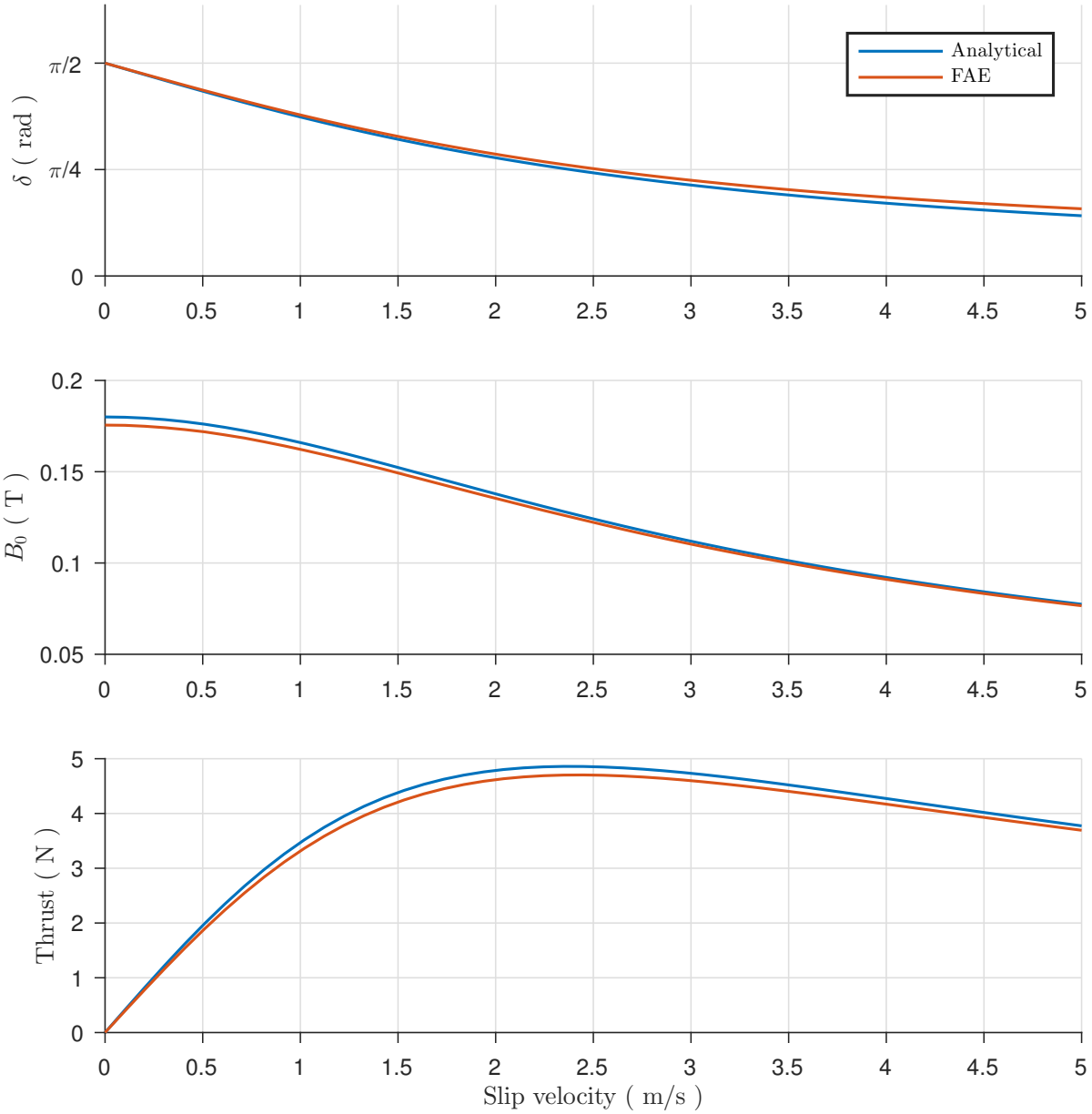

Figure 2.18: Continuous machine behavior with regard to velocity predicted by both the analytical model and FEA, δ gives the phase lag of the magnetic field with regard to the current excitation, B_0 gives the amplitude of the magnetic field in the air gap

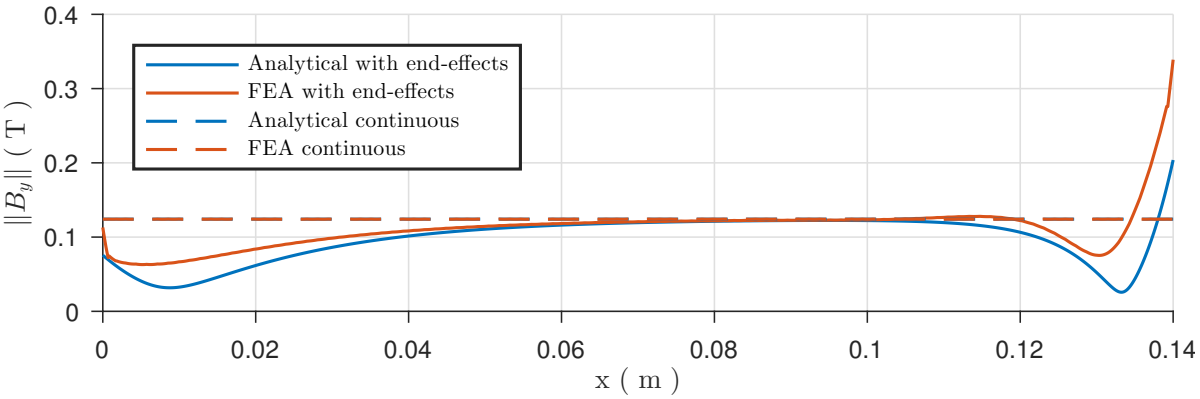

Figure 2.19: Magnetic field magnitudes for both the analytical and FEA model, given for a rotor and slip velocity of both 2.5 m/s

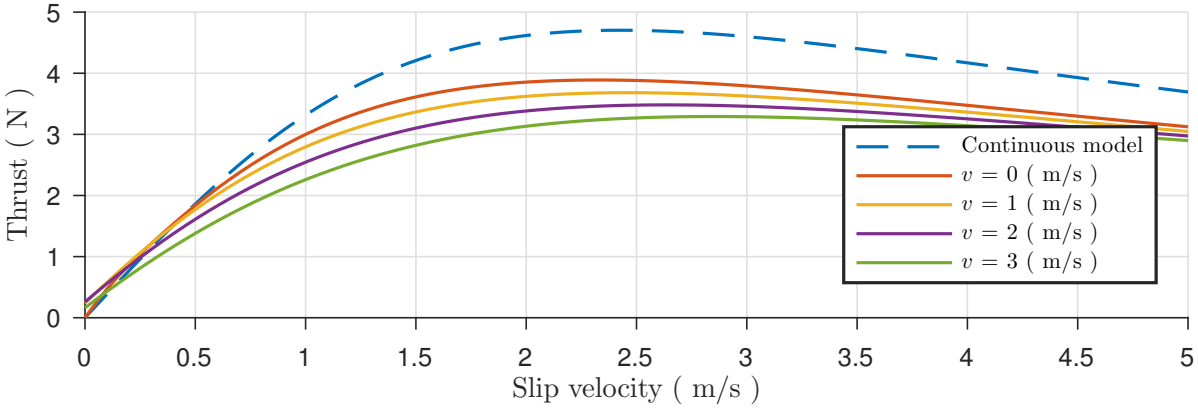

Figure 2.20: Thrust with respect to slip velocity for various rotor velocities. One can see a degradation of the thrust curve for higher rotor velocities due to the end effects. The continuous model does not take these effects into account and can therefore be considered ideal

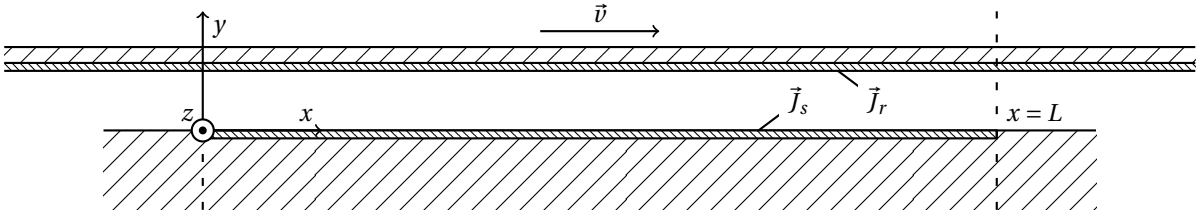

Figure 2.21: Side view of model of a linear induction machine including the possibility of the magnetic field to leak out of either end. The leakage of flux was constraint in the former models assuming (2.42)

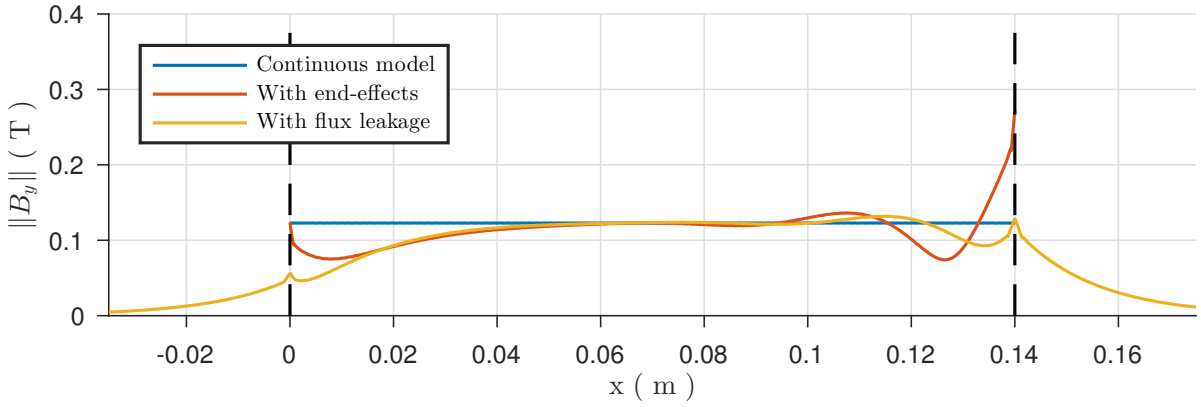

Figure 2.22: Magnetic field magnitude along the air gap described by different models, for a static rotor and slip velocity of 2.5 m/s. One can see a smoothing of the end effects due to the flux leakage that was introduced

Spacial current distribution

In reality the excitation current in an induction machine is most often applied through the use of copper windings. Although many winding schemes are possible, nearly all will result in a spacial current distribution that differs from the ideal current sheet description. The variation from the earlier assumed sine will cause higher harmonics in the gradient and thus also in the developed magnetic field and induced rotor currents.

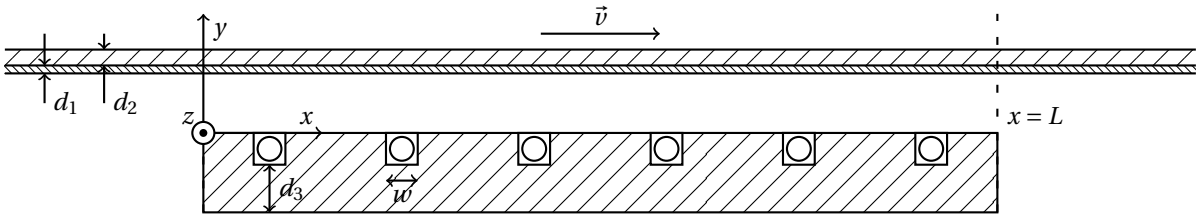

Figure 2.23: Side view of model of a linear induction machine with a current excitation in the form of stator windings

Figure 2.23 depicts such a model where the windings are placed into slots of the rotor. The current distribution is now no longer distributed evenly along the length of the machine. Figure 2.24 shows the difference in the magnetic field distribution in the air gap, between a coil excited LIM and one excited using the current sheet description.

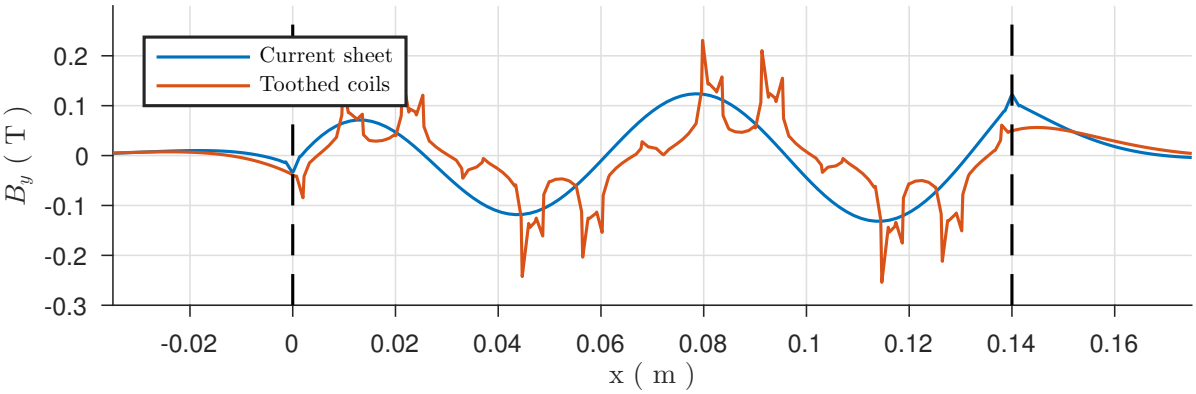

Figure 2.24: Spacial magnetic field distribution for a certain point in time of a 4 pole LIM, comparison is made between excitation by a current sheet and stator windings

Note the strong gradients caused in the field due to the spacial higher harmonics. These gradients will also induce eddy-currents that in some cases counteract the first harmonic. Devision from a pure sinusoidal current distribute will therefore reduce the produced thrust.

Iron losses

Finally the model is completed by introducing the iron losses present in both the stator core and iron backing of the rotor. Iron losses are classically split into hysteresis losses, excess losses and eddy-current losses [3]. The former is introduced by the energy dissipated in the Weiss domains under the presence of a varying magnetic field.

The hysteresis of the iron parts is visualized in figure 2.25a. As can be seen, the HB-curve is not a pure line but encloses an area. Every full magnetizing cycle an amount of energy proportional to the area will therefore be lost as hysteresis losses. One can describe these losses as the energy needed for the Weiss domains to change the orientation of their magnetization.

Excess losses are the losses caused by a higher dynamic effect caused in the Weiss domains. For the magnetization does not happen gradually but in so called Barkhausen jumps. These fast jumps cause small eddy-currents that get dissipated in the iron.

Finally figure 2.25b depicts the macro eddy-current that arise from the changing magnetic field through the iron. The eddy-currents will in turn result in Joule losses.

Using the FEA model the hysteresis and eddy-current losses together with the magnetic saturation of the iron can be taken into account.

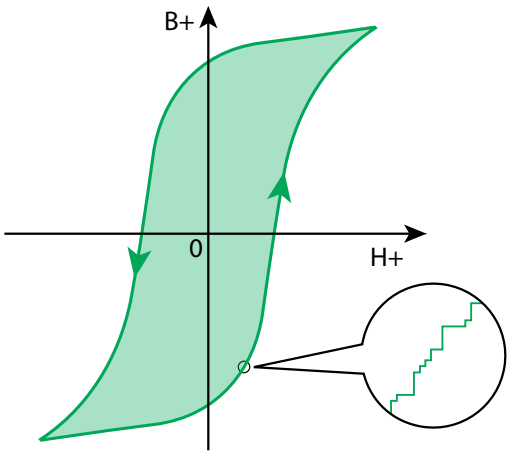

(a) Magnetization curve of iron including the Barkhausen jumps, visualizing the magnetic hysteresis in a magnetic cycle

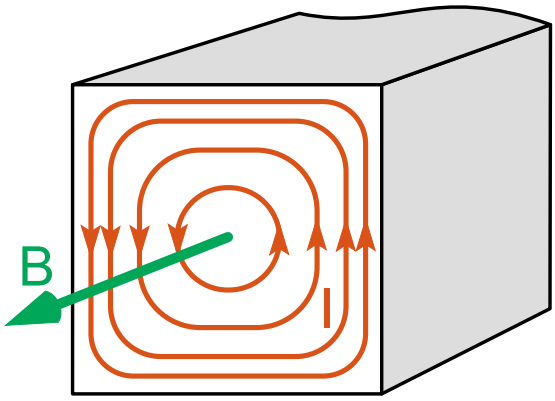

(b) Visualization of eddy-currents in an iron bar due to a varying magnetic field

Figure 2.25: Causes of iron losses in the form hysteresis losses and eddy-current losses

Model comparison

The various steps taken above describe the various sources of losses that are taken into account modeling the linear induction machine. Below the resulting static motor thrust is shown after cumulative addition of the various losses.

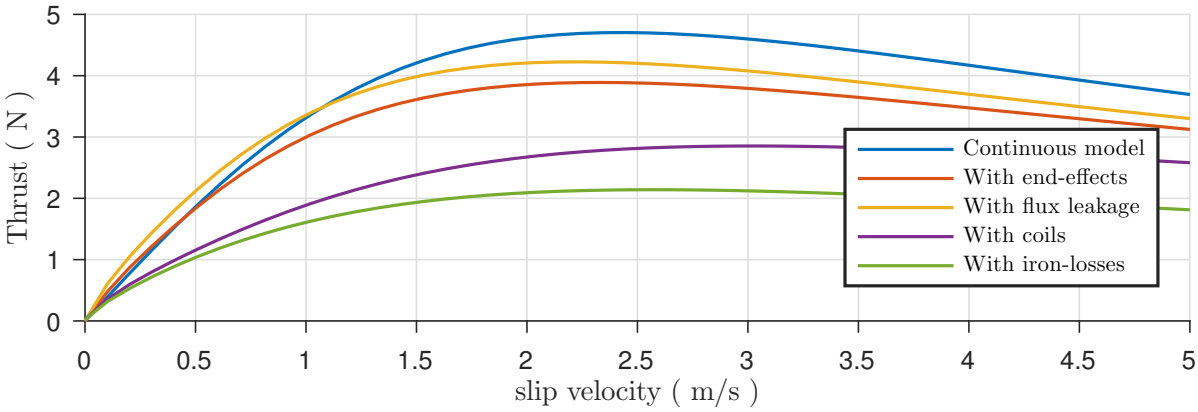

Figure 2.26: Static thrust with respect to slip velocity for cumulative addition of various losses. One can see that the initial force curve described by the ideal continuous model is degraded by the various model refinements introduced

As seen from figure 2.26 the largest degradation of thrust for a static rotor is caused by the non-linear spacial current distribution. For higher velocities the end-effects become the dominant source of loss as they protrude further along the length of the machine.

One can also look at the effect various of the modeling refinements have on the normal force working on the rotor in y-direction. This force is dominated by the negative reluctance force working on the iron backing of the rotor. This effect can be seen to be fairly constant although it grows significantly under the introduction of the flux leakage for low slip velocities. This is due to the fact that the reluctance path of the machine is hereby significantly reduced as the area over which the flux can cross the air-gap is increased.

As the excitation frequency increases the reluctance force is counteracted by the electro-magnetic levitating force caused by the induced eddy-current in the rotor. The most prominent effect on the levitating force is caused by the introduction of the non-linear spatial current distribution. As described before this causes the introduction of higher spacial harmonics in the induced currents and although they diminish the thrust they increase the levitating forces.

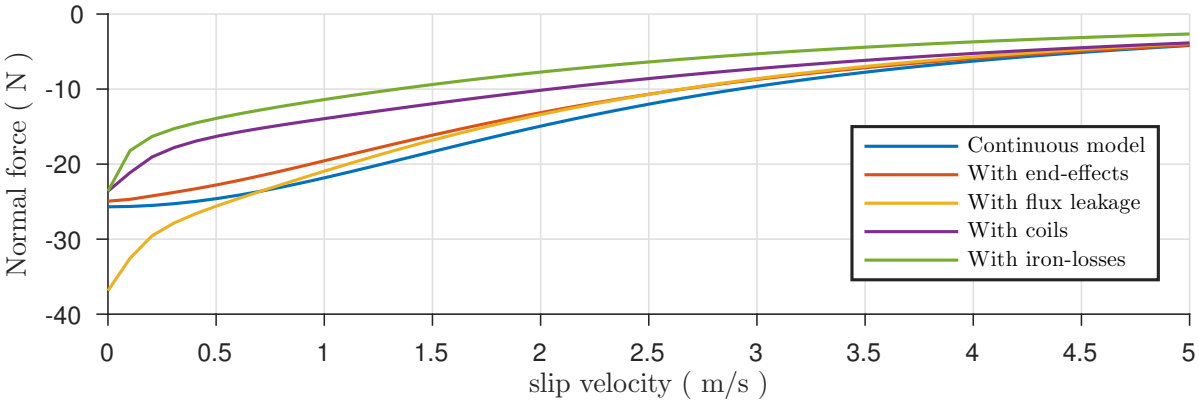

Figure 2.27: Static normal force with respect to slip velocity for cumulative addition of various losses. One can see that the normal force is dominated by the attractive reluctance forces, as the electrical frequency increases these are slowly compensated by the levitating forces due to eddy-currents

2.4.4. Equivalent circuit model

For use on the real-time embedded control a simplified lumped model will be developed. The parameters of which will be empirically determined at a later stage in this thesis (appendix B). The lumped model used, is defined using an equivalent circuit description.

5 parameter phase model

The single phase 5 parameter model is often used to describe the steady state of rotational induction machines. As proposed by J. Duncan [11] the same model can be used to describe the steady state behavior of a linear induction machine by the introduction of velocity dependent terms. A description later improved upon by the use of FEA data to determine the parameters [27]. Here a linearized model will be given for a quasi-static rotor state.

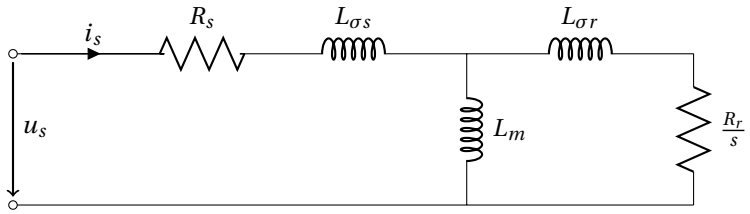

Figure 2.28: 5 parameter single phase equivalent circuit model

As depicted above the 5 parameter model is described by 5 parmeneters. The effective rotor resistance is given by $\frac{R_r}{s}$ where s is the slip of the machine, the stator resistance in turn is given by R_s. L_m is the magnetizing inductance of the induction machine and the respective stator and rotor leakage inductances are given by $L_{\sigma s}$ and $L_{\sigma r}$.

$$\lim_{s\to 0} \frac{R_r}{s} = \infty, \qquad \lim_{s\to 1} \frac{R_r}{s} = R_r \tag{2.43}$$

At synchronous speed ($s = 0$) the effective rotor resistance will approach infinity as in this state close to no rotor currents will be induced. As the slip increases the efective rotor resistence will approach R_r as seen in (2.43).

4 parameter phase model

As the devision between the stator and rotor leakage inductance is often difficult do distinguish they are often assumed to be equal ($L_{\sigma s} = L_{\sigma r}$). Under this approximation one can converter the 5 parameter model to the 4 parameter description shown in figure 2.29.

The resulting parameters can be transformed using the transformation factor [8] described by (α).

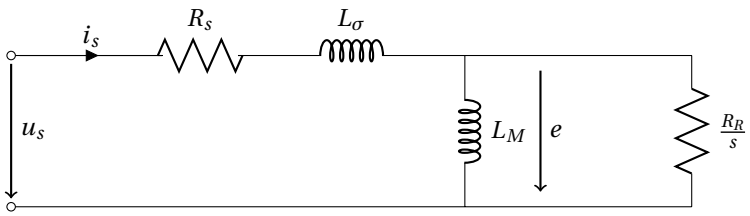

Figure 2.29: 4 parameter single phase equivalent circuit model

$$a = \frac{L_m}{L_r} = \frac{L_m}{L_m + L_{\sigma r}} \tag{2.44}$$

$$L_\sigma = \left(\frac{L_s}{L_m} - a\right) \cdot L_m = \left(\frac{L_m + L_{\sigma s}}{L_m} - a\right) \cdot L_m \tag{2.45}$$

$$L_M = a \cdot L_m \tag{2.46}$$

$$R_R = a^2 \cdot R_r \tag{2.47}$$

The back EMF with amplitude $\hat{e}$ is also shown. Here the amplitude is considered proportional to the electrical frequency and the magnetic flux in the machine. The equivalent circuit describes the machine flux using (2.48) where i_d is the direct current. As later described the direct current is the current component of the stator flux that is in phase with the magnetic flux axis.

$$\psi = L_M \cdot i_d \tag{2.48}$$

$$\hat{e} = p \cdot \omega_e \cdot \psi \tag{2.49}$$

3 phase description

Figure 2.30 shows a typical linear 3 phase machine model often used to represent a star-wired stator of induction machines. Note this lumped description describes the steady state of a machine under harmonic excitation. Non-linear effects as velocity dependent end-effects, spacial current distributions and iron saturation cannot be described using this simplified model.

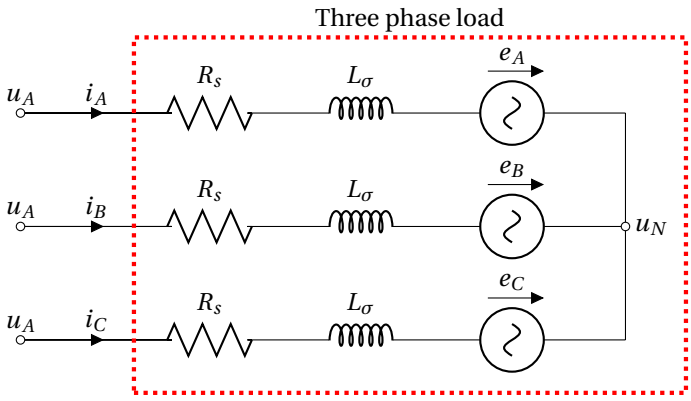

Figure 2.30: Typical 3 phase machine model

The parameters are equal to that of the 4 parameter machine depicting only the stator side of the machine. It is the model in this form upon which the control described in later chapters will be developed.

Appendix B discusses the steps taken to fit the equivalent circuit models to the empirical data. In the remainder of the thesis these fitted parameters will be used in the control design as given in table B.1.

3

Design of a linear induction machine

As described in the introduction of this thesis a linear induction machine will be developed to perform a feasibility study of its use in planar positioning. Such a system is usually comprised of three here separately described systems, the linear induction machine, the drive electronics and the controller.

First the geometric design of the induction machine will be described based on a sensitivity study performed using the previously developed models. Followed by a description of the requirements of the stock drive electronics and their use. Finally the control strategy will be covered and implemented. The achieved performance under the various actuation methods is also covered accordingly.

3.1. Geometric design

The design of a linear induction machine is described in this section. The various decisions that have to be made will here be documented in a collinear fashion although the reality is prone to heavy iteration between the various steps taken. The effect design parameters have with respect to the pure actuator performance, system performance (of a planar stage) and in relation to other components as the electronics and controller will be discussed.

The initial section will focus on a sensitivity study performed using the models described in the previous section. The knowledge gained from this will be combined to develop a design approach and its implementation into a detailed design. Also the set of experimental set-ups built around the linear induction machine will be covered with the initial verification of the physically built machine.

3.1.1. Sensitivity analysis

The sensitivity study performed here is to describe the effect change of a design variable has on the LIM performance in terms of thrust. The model used is the most thorough FEA model developed in the previous section described by in figure 2.23.

All simulation will be done for the parameters of the final machine described in appendix A, unless otherwise stated and of course the parameter for which the sensitivity is described. The current amplitude used is $i_s = 1\,\mathrm{A}$. Where necessary the cross coupling between these single parameter sensitivity analysis will be described.

Pole pitch sensitivity

As seen in the modeling section, the pole-pitch (τ) is the main variable describing the first harmonic of the spacial fields. Below the three main consideration in choosing the pole-pitch are discussed.

The most obvious influence the pole-pitch has is the relation between the electrical frequency and the velocity of the traveling excitation wave (2.8). As seen before the synchronous speed (equal to the slip velocity for a stationary rotor) is equal to $v_e = \frac{\omega_e \cdot \tau}{\pi}$. Furthermore it was shown that the thrust of a LIM can be described with regard to the slip velocity (figure 2.18). This shows that for a decrease in the pole-pitch of the LIM the excitation frequency at which the maximal thrust is produced is increased according to (3.1).

$$f_{e,max} \propto \frac{1}{\tau} \tag{3.1}$$

An increase of the excitation frequency is however constraint by the sampling time of the controller and the saturation of the inverter used to produce this excitation.

The second aspect variation of the pole-pitch influences is the spread of the end-effects. As seen before in figure 2.16 the influence of the end-effects can be neglected after about twice the pole-pitch from either end of the machine. To obtain motor characteristics that approach that of the continuous model (upon which the control theory is based) a smaller pole-pitch is thus desired. Note one should always keep the number of poles per phase equal to avoid unnecessary phase unbalance.

Finally the side of the pole-pitch also has an influence on the leakage flux inside the machine. During the modeling phase the effective air gap was assumed small with respect to the pole-pitch of the machine ($1 \ll \frac{g}{\tau}$). If this is no longer the case the assumption of a pure magnetic flux in the y-direction of the air gap will no longer be valid. A greater ratio of the magnetic field lines will no longer pass through the rotor but will return withing the air gap itself.

Current density sensitivity

The amplitude of the current density of the excitation is described as J_0 and is proportional both to the phase current and the number of windings per coil (n). (2.22) shows that the average thrust of the continuous model is proportional to both the amplitude of the current and magnetic field density, respectively J_0 and B_0. Furthermore (2.20) shows that the latter is also proportional to the current density, resulting in a final sensitivity of the thrust as described in (3.2).

$$F_x \propto J_0^2 \tag{3.2}$$

The results of a numerical sensitivity analysis of the number of coil windings is shown in figure 3.1. Confirming the cubic relation derived from the analytical model.

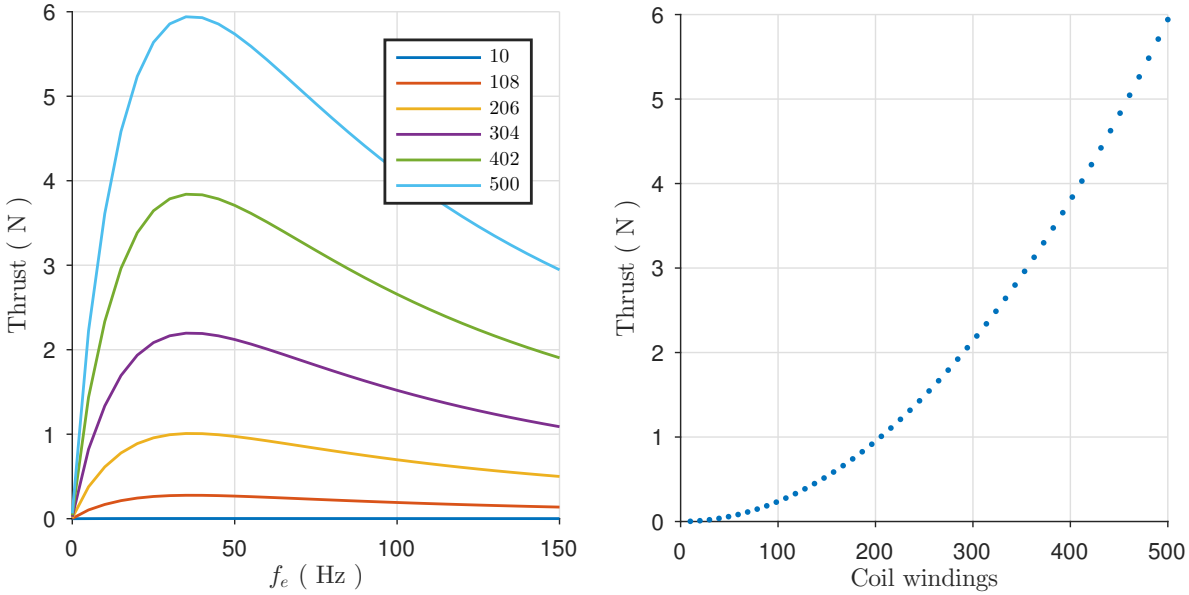

(a) Selection of thrust curves with regard to the slip frequency

(b) Sensitivity of maximum thrust

Figure 3.1: Sensitivity analysis of the number of coil winding, n

Effective air gap sensitivity

As one would expect a larger air gap will result in a decreased thrust. The continuous model suggests that the thrust will asymptotically decrease to zero for an increase of the effective air gap according to (3.3).

$$\delta \propto \tan^{-1}(g), \qquad F_x \propto \cos(\delta) \tag{3.3}$$

Again the numerical analysis verifies the asymptotic decrease of the thrust as the effective air gap is increased (figure 3.2). Notice that as the numerical analysis now describes a geometric variation of the model, re-meshing causes some numerical noise in the results.

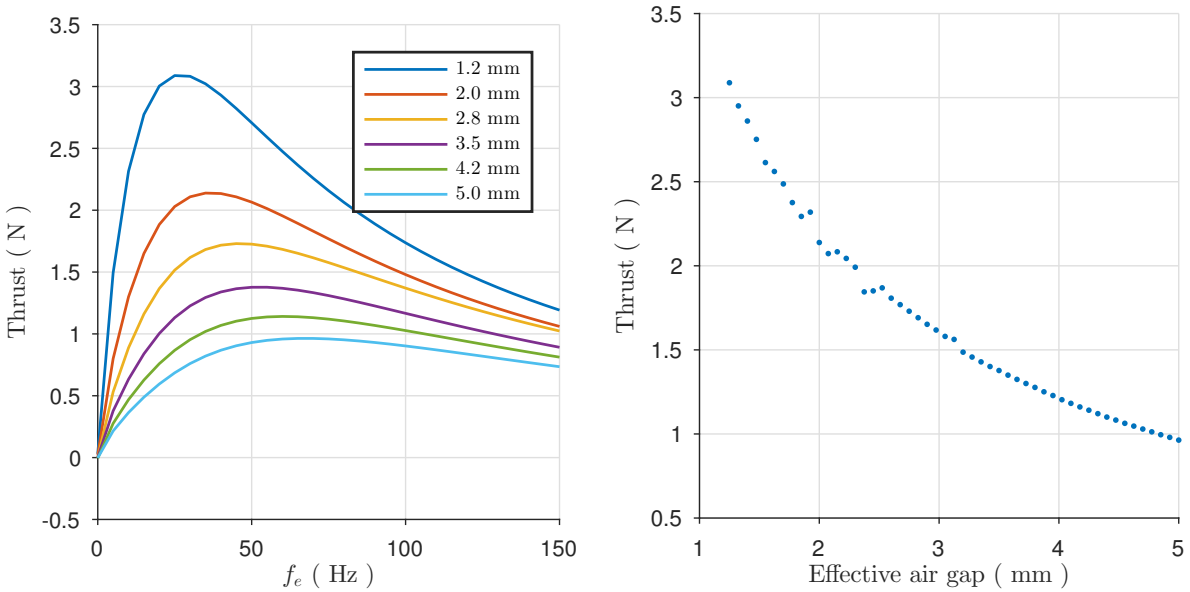

(a) Selection of thrust curves with regard to the slip frequency

(b) Sensitivity of maximum thrust

Figure 3.2: Sensitivity analysis of the effective air gap, g

Rotor conductor thickness sensitivity

Notice the effective air gap in the model contains the thickness of the rotor conductor as well as the physical air-gap. This assumption is based on the fact that magnetic permeability of the conductor can in most cases be considered equal to that of air. The conductor thickness (d_1) is also present in the description of the surface current (2.11). Under the assumption that $g \approx d_1$ one can describe the sensitivity of the thrust as being inverse proportional to the conductor thickness 3.4.

$$F_x \propto -d_1 \tag{3.4}$$

The numerical model (figure 3.3b) shows the inverse proportionality described above for thick conductors. It however also describes the drop in thrust for very thin conductor sheets. As described in (2.21) for this case the limit of the phase lag of the magnetic field to the current sheet becomes (3.5).

$$\lim_{d_1 \to 0} \delta = \frac{\pi}{2} \tag{3.5}$$

The physical interpretation for this is that the rotor surface resistance becomes so large that hardly any currents are induced. All the excitation magnetomotive force is contained within the magnetic field that cannot produce any thrust without rotor currents.

Although defining performance in terms of thrust is a valid approach, measurement of the force to mass ratio might be a more insightful performance criteria on a system level. In the case of a small load the moving mass and thus dynamic behavior of the system will be dominated by the rotor mass.

Figure 3.3c gives the sensitivity of the normalized maximum thrust with regard to the conductor thickness. As the conductor mass is proportional to the thickness with its density, the force is normalized as $\frac{F_x}{d_1}$. As seen in this case the choice for a thin conductor can be justified within the mechanical constraints on the rotor design.

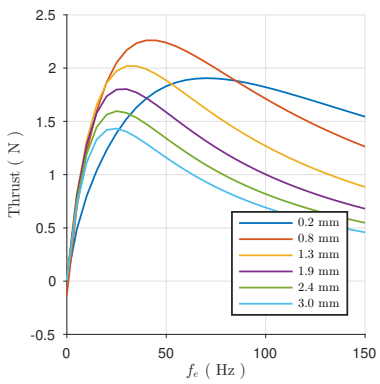

(a) Selection of thrust curves with regard to the slip frequency

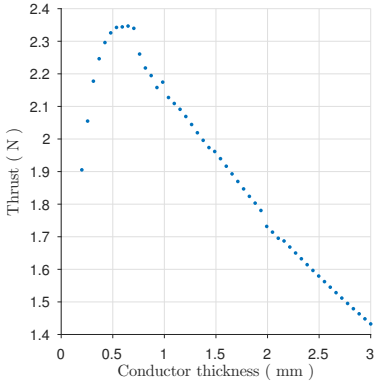

(b) Sensitivity of maximum thrust

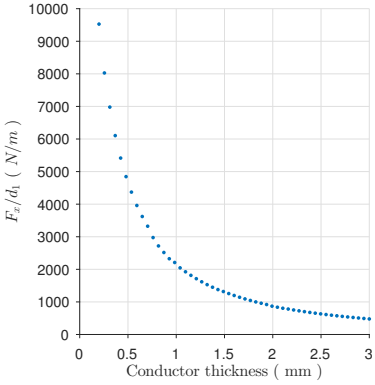

(c) Normalized sensitivity of maximum thrust

Figure 3.3: Sensitivity analysis of rotor conductor thickness, d_1

Rotor back iron thickness sensitivity

The sensitivity of thrust with regard to thickness of the rotor back iron is not available from the analytical model as it is considered ideal ($\mu = \infty$). In reality this approximation is only valid while the iron is unsaturated. Figure 3.4b describes this behavior as one can see a decrease of the thrust for thin (saturated) iron backings. Once saturation is avoided further increase of the backing thickness does not add to additional thrust.

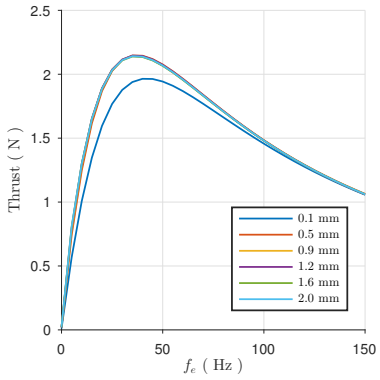

(a) Selection of thrust curves with regard to the slip frequency

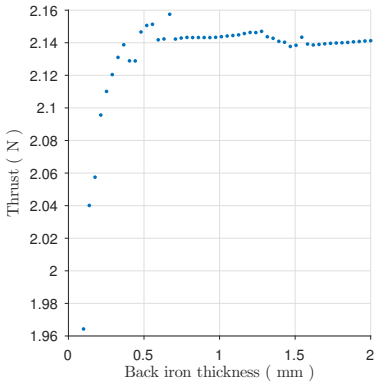

(b) Sensitivity of maximum thrust

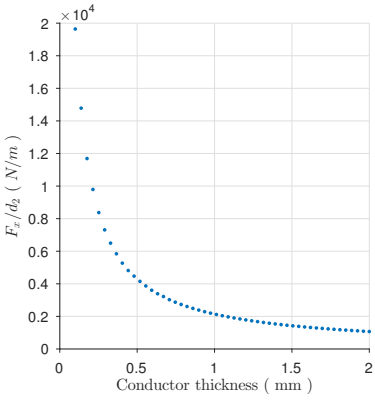

(c) Normalized sensitivity of maximum thrust

Figure 3.4: Sensitivity analysis of rotor iron backing thickness, d_2

The iron backing too adds to the moving mass of the final mechatronic system. For this reason the sensitivity of the normalized thrust is given as shown in figure 3.4c. Once again one can see that if the mass of the load can be neglected the choice of a configuration with degraded thrust due to saturation might still be preferable.

Stator core thickness sensitivity

As long as saturation of the stator is avoided the thrust is fairly insensitive to the stator thickness (d_3). As in this thesis the stator side of the machine is considered to be stationary the mass due to thickness is of no concern here. For large and/or mass-critical systems the use of excessive material can however be undesirable. A good description of the trade-offs involved are covered in the thesis on the design of a LIM actuated aircraft launch system [20].

Winding width sensitivity

Finally the sensitivity to the width of the coil windings (w) is covered. In literature the use of toothless stator designs are proposed to minimize the spacial higher harmonics [24]. As seen before in figure 2.26 the higher

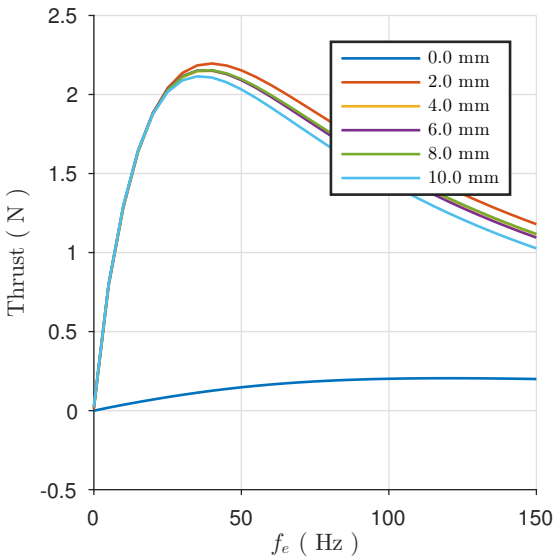

(a) Selection of thrust curves with regard to the slip frequency

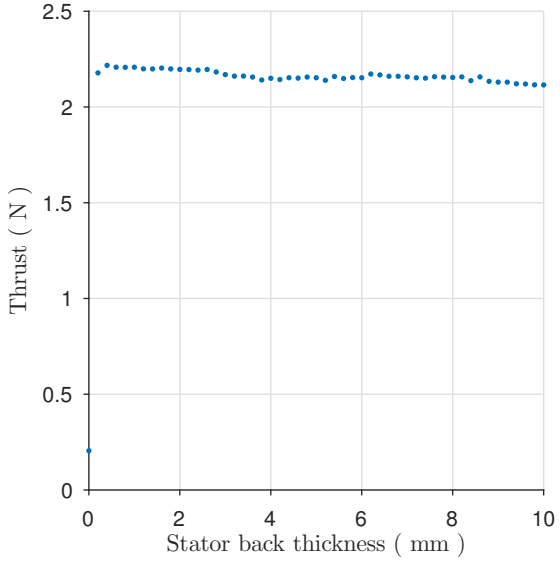

(b) Sensitivity of maximum thrust

Figure 3.5: Sensitivity analysis of stator core thickness, d_3

harmonics of the current distribution are indeed responsible for a large part of the machine losses. Thinning the stator teeth beyond the point of saturation will however increase the magnetic reluctance path of the machine, effectively increasing the air-gap. One can thus describe the winding width as a trade-off between a high magnetic field and the spacial distribution of it.

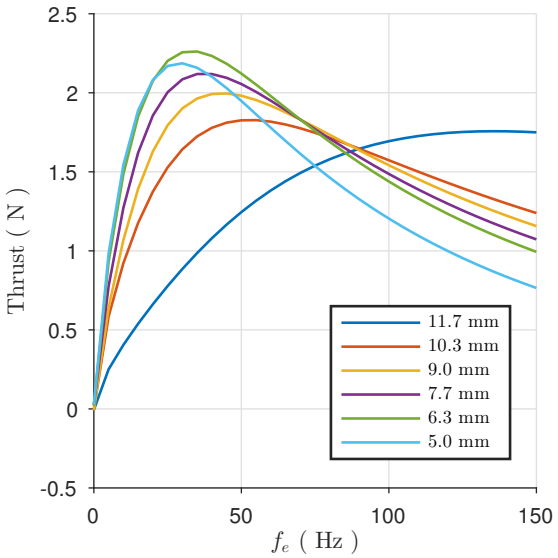

(a) Selection of thrust curves with regard to the slip frequency

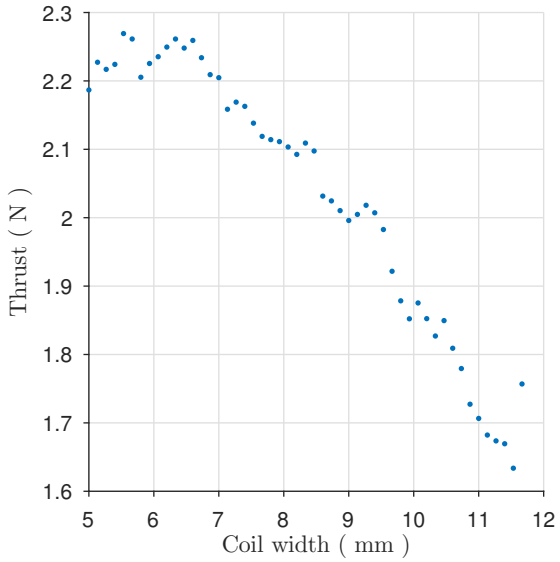

(b) Sensitivity of maximum thrust

Figure 3.6: Sensitivity analysis winding width for a constant winding area, w

For a machine as considered in this thesis, with a relative low excitation current and air gap, figure 3.6b shows a preference for a toothed stator. As the coil width increases the generated thrust deteriorates, one can however see that for the limit case ($w = \frac{\tau}{3}$) there is a slight increase of the thrust, here the coils cover the entire motor length reducing the spacial harmonics of the current distribution.

3.1.2. Design synthesis

The approach to the design of a linear induction motor for use in planar actuation is covered in this section. Initially a description is given of some aspects of the design for planar positioning, as the transverse effects in the z-direction of the machine that have up to now not been covered. Followed by a proposed collinear design approach to develop a suitable machine. Finally the additional choices made in the detailed design are covered.

Considerations transverse direction

The transverse direction of a linear induction machine is in the modeling section referred to as the z-direction. In the modeling section these transverse effects were not discussed as they are not contained in the 1D and 2D models. In reality the induced currents are however not purely in z-direction causing variation in the magnetic field along the motor in the transverse direction (figure 3.7).

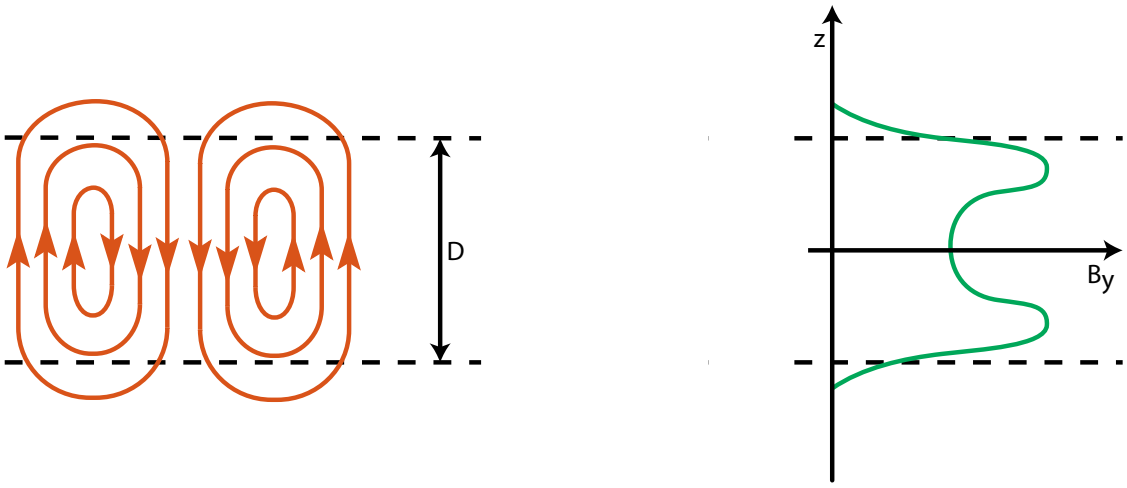

(a) Top view of current flow in part of the rotor conductor, the current flow can be seen to have a x-component both above the stator and in the rotor overhang

(b) Transverse section of the magnetic field norm in y-direction along the depth of the LIM, field can be seen to be non-uniform above the stator and to "leak" into the overhang

Figure 3.7: Magnetic field distribution in transverse direction under consideration of the x-component of the rotor currents

The transverse effect can simply be added to the analytical and numerical model using a method developed in [4, 44]. Thrust degradation due to the transverse effect is accounted for using a modified surface conductivity.

In case of transverse movement of the rotor the magnetic gradient shown in figure 3.7 will cause eddy-current damping. To minimize this effect the choice is made to focus on the straightforward toothed stator design over more exotic winding schemes that would increase the magnetic flux gradients in transverse direction.

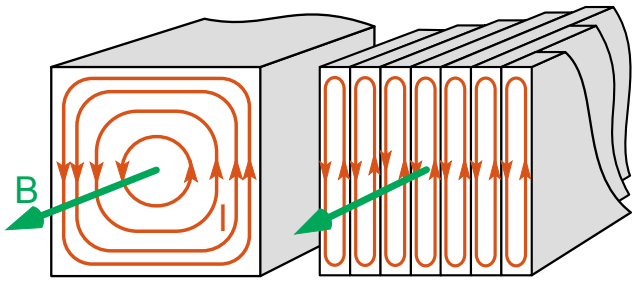

Figure 3.8: Reduction of eddy-current losses, by using a core composed of insulated laminates

The other transverse consideration that has to be made is in regard to eddy-currents that are generated in the stator core. The resulting Joule losses are often counteracted by the use of a non-continuous stator core

in the form of laminates. As can be seen in figure 3.8 the use of a laminated core that has insulating layers in between the laminates, avoids concentration of the induced currents. As the Joule losses are proportional to the squared current this reduces the losses significantly.

Design approach

Design of the linear induction machine as an actuator for planar positioning is done using the design approach described below. The resulting actuator is made to be optimal in terms of thrust production under limitations of the current source.

Length over depth The first design rule is to determine the length of the motor with respect to its depth in the transverse direction. According to the continuous analytical model (2.23) the thrust is proportional to both the length and depth of the machine (3.6).

$$F_x \propto D \cdot L \tag{3.6}$$

As seen before the sensitivity to the longitudinal end-effects is however proportional to the length of the machine as they have a spread of about twice the pole-pitch. It is for this reason the design approach defines the length of the machine only limited by the physical design constraints.

Pole-pitch In accordance with the sensitivity analysis (section 3.1.1) the pole-pitch is defined as small as possible to minimize the effect of the end-effects. Two considerations have to be taken into account, first is the minimal pole-pitch as limited by the electrical bandwidth of the current source, second being change of the pole-pitch should be chosen such that a full number of pole-pitches fit in the length of the machine.

Stator core thickness The thickness of the stator core should be sufficient to allow for a low reluctance return path of the magnetic flux. As seen in the sensitivity analysis an increase of the thickness beyond the saturation limit will however not improve the thrust significantly. The stator core thickness will therefore be designed to just avoid magnetic saturation.

Note that the stator thickness for which saturation occurs is dependent on the later determined current density. The sensitivity to this is however small with regard to the sensitivity to the earlier determined pole-pitch. The actual stator core thickness could thus be determined using an interactive approach although in practice a collinear approach will result in approximately the same result due to the low sensitivity.

Machine depth Using the limitations of the current source one can determine the phase resistance one can design for. In turn the winding current will determine the wire gauge necessary and thus the length of available wire for winding (l). The rule of thumb here is to use a current density of between 2.5 A/mm^2 and 6 A/mm^2 depending on the heat dissipation available.

The trade-off that is hidden in determination of the machine depth is in the number of windings that fit around the core and the length of the active wire. As seen in (3.2) the number of windings are squared proportional to the thrust, the thrust is however linear proportional to the depth (3.6). As shown in (3.7) the length of a single winding is proportional to twice the depth and a certain constant length (l_0) used to represent wire length in the ends.

$$l_n = 2(D + l_0) \tag{3.7}$$

$$n = \text{round}\left(\frac{l}{l_n}\right) \tag{3.8}$$

$$F_x \propto n^2 \cdot D \tag{3.9}$$

Using (3.8) one can now describe the number of windings with respect to the machine depth. Figure 3.9 shows the variation the depth has on the normalized parameters described above.

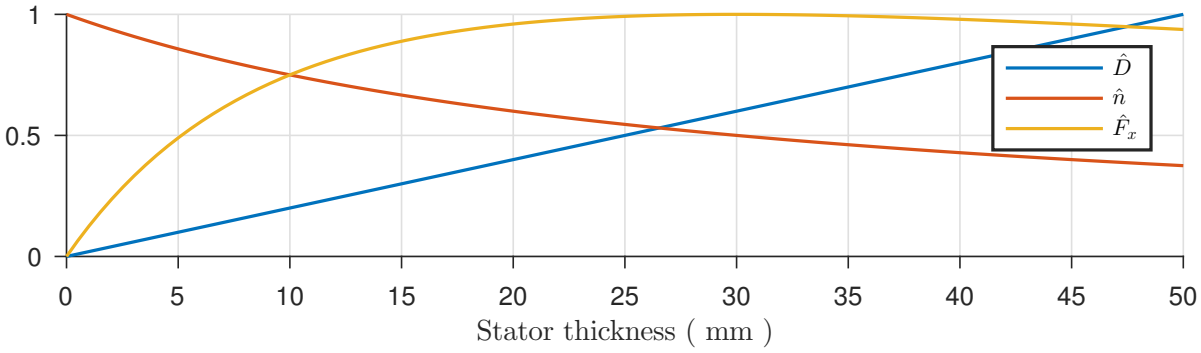

Figure 3.9: Visualization of the trade-off between the number of windings and machine depth, $l_0 = 30\,\text{mm}$

Rotor design The design of the rotor is mostly covered in the sensitivity analysis and depends heavily on the mass of the load. If the load can be neglected with regard to the rotor mass one should minimize both the conductor and back iron thickness as far as possible. The limits here are constraint by the manufacturability and the description using continuum mechanics.

For applications in which the mass of the rotor can be neglected with regard to that of the load the sensitivity analysis will describe the conductor thickness for which maximum thrust is generated. The back iron should again be taken as thin as possible while avoiding saturation.

Summary Below the collinear steps involved in the synthesis of a machine design are summed. Following the various steps described result in an adequately designed LIM optimized for maximum thrust within the constraints of the current amplifier and size constraints (maximum length).

1. Maximize length as allowed by mechanical constraints
2. Maximize the number of poles-pitches that fit in the length, constraint by the amplifier bandwidth following (3.1)
3. Minimize the stator core thickness until saturation occurs
4. Determine wire gauge and length according the excitation current
5. Optimization of machine depth according to (3.9)
6. Chose optimal rotor conductor thickness according to sensitivity analysis
7. Minimize rotor backing thickness until saturation occurs

Detailed design

Below the detailed design of the physical linear induction machine build is covered. The steps described in the previous section will be touched upon only briefly focusing on some of the more detailed level design choices made during the machine build and design.

Mechanical constraint The design of an amplifier produced keeping a planar application of a wafer handler in mind. As a typical wafer has a mean diameter of 300 mm the choice is made to limit the actuator length to 140 mm to allow a configuration similar to that shown in figure 2.11b.

Amplifier constraint As the current source initially used in the development of the actuator (detailed description in appendix C) is for a source voltage of 48 V limited to an amplitude of about 2 A for a respectable bandwidth of ≈ 80 Hz. Furthermore the linear amplifiers are power limited to 30 W.

Machine stator sizing As stated by the design approach, the machine length is chosen maximal, in this case the full 140 mm allowed by the constraints. One can thus define the pole-pitch of the machine as the maximum number of pole-pairs that fit in the machine without saturating the current supply. One can see that for 2 pole-pairs ($p = 2$, $\tau = 35\,\text{mm}$) and a slip velocity of 2.5 m/s, electrical frequency stays under the amplifier saturation limit up to a rotor velocity $\approx 2.5\,\text{m/s}$.

$$f_e = \frac{v_s + v}{2\tau} \tag{3.10}$$

Finally the stator core thickness is set to 15 mm, this is far above the minimum needed to avoid saturation. In the design the stator core will however also be used as the basis for mechanical mounting.

Machine windings The machine windings chosen are so called Gramme-ring windings. They were found in simulation to have the best thrust characteristics to other winding layouts under the manufacturing constraint of a 2.5D coil design. As seen in figure 3.10 the winding configuration allows for a compact current distribution and a simple coil design.

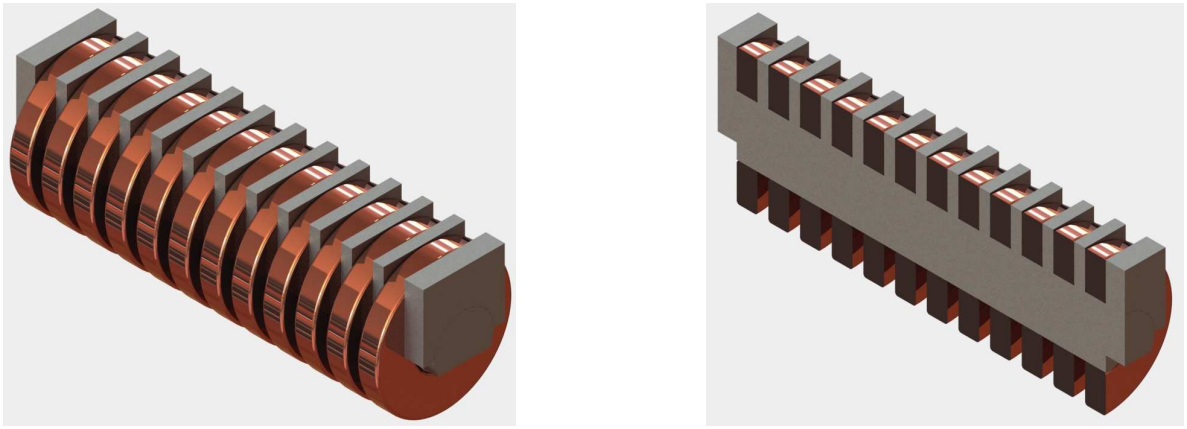

(a) Isometric view

(b) Longitudinal section of stator core

Figure 3.10: Render of toothed stator core with Gramme ring-windings

The coils designed are made using copper wire with a diameter of 0.5 mm, limiting the coil current to about 1 A for a current density of $5\,\text{A/mm}^2$. To match the current amplifier used, the phase coils will be wired in two parallel sets (figure 3.11).

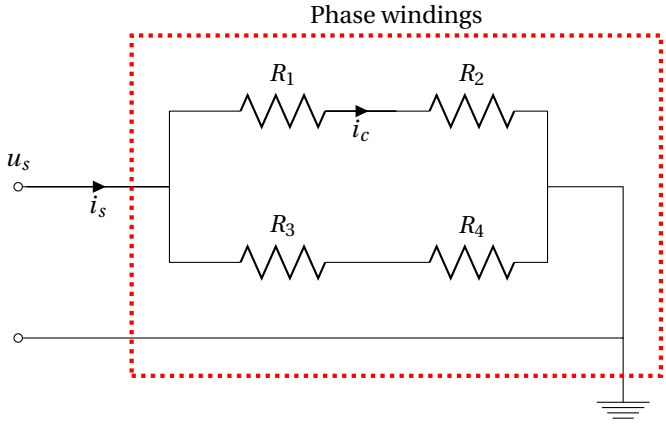

Figure 3.11: Winding scheme of phase coils belonging to a single phase

The phase resistance in terms of the separate coil resistances is given in (3.11). As one can see for this specific configuration the resistive value is equal for both.

$$R_s = \left(\frac{1}{R_1 + R_2} + \frac{1}{R_3 + R_4} \right)^{-1} = R_c \tag{3.11}$$

From here one can compute the wire length available per stator coil using the resistivity of the copper wire. Finally the number of windings per coil and machine depth are obtained from figure 3.9.

Rotor design Design of the rotor is done using the sensitivity analysis shown in figure 3.3b. To account for the strong non-linearity in sensitivity in the maximum thrust region the choice is made to use a conductor thickness of 1 mm. After accounting for the effective rotor conductivity this is found to give the maximal performance.

Design of the iron backing is 1.5 mm in thickness resulting in an unsaturated iron backing. The increased thickness is chosen to avoid saturation even under variance in electromagnetic properties of the material.

Mechanical fabrication The full machine parameters are described in appendix A. The physical realization of the design will here be covered as it was used to develop the final version. Note the process has been a long and interesting road as the building of electromechanical assemblies has proven far from trivial.

The initial design was composed of a laminated stator core. The fabrication of which after a lot of experimentation proved to be no simple feat either by traditional machining techniques or laser cutting of the stator laminates. Pushing the project forward the alternative of a solid steel core was adopted. The fabrication of which is covered below.

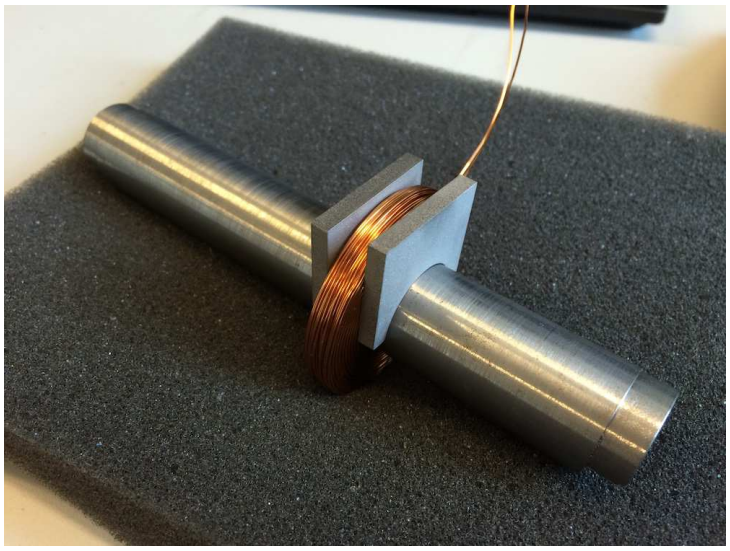

(a) Assembly of the stator core with a single coil and two stator teeth

(b) Coil being wound around the jig within the coil winder

Figure 3.12: Production images of the stator assembly and the winding of the stator coils

As can be seen in figure 3.12a the alternative design is comprised of a round stator core upon which stator teeth and coils are assembled. The fabrication of the coils are discussed in more detail in appendix E, figure 3.12b shows the winding-jig mounted in the coil winder.

Once the stator core is fully assembled it is placed in a machined aluminium base used both to accurately mount the LIM with regard to other parts of the set-up and as a heat-sink for the stator coils. To provide a low thermal barrier between the stator windings and the base, it is filled with resin that has a high thermal conductivity. The final assembly is shown below in figure 3.13.

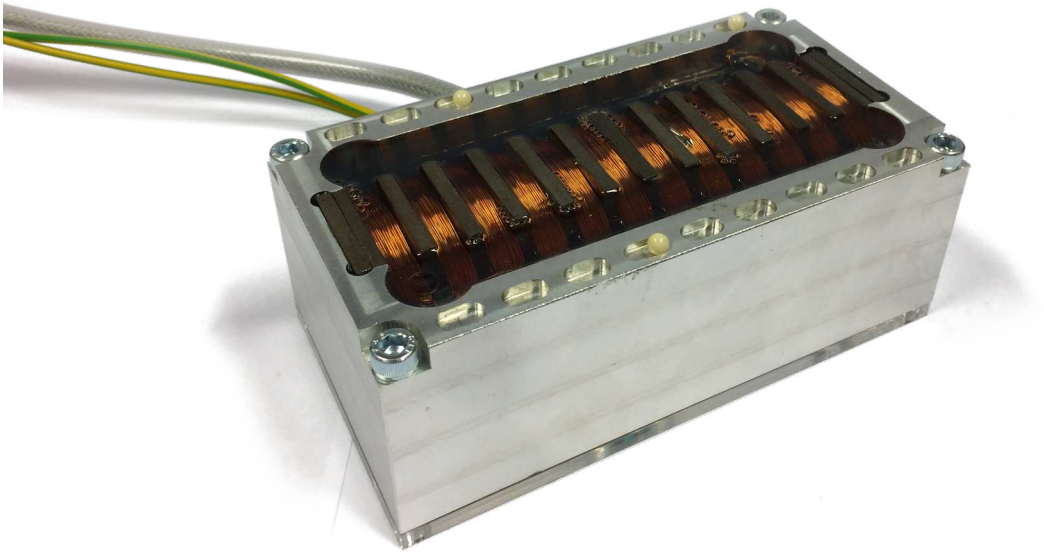

Figure 3.13: Stator side of linear induction machine assembly, placed in machined base and filled with thermal resin. Ceramic ball bearings used in the static setup visible

3.1.3. Experimental setups

Using the LIM designed in the previous section a set of two experimental setups were designed. The stationary set-up is built to measure the static thrust characteristics of the machine. The dynamic set-up allows for infinite rotation of the circular rotor and thus allows for verification of the positioning capabilities of the machine.

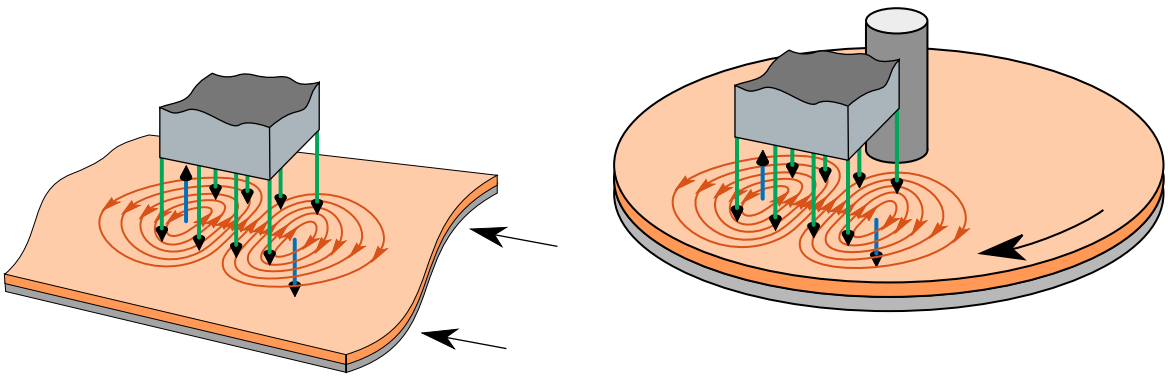

(a) Static set-up

(b) Dynamic set-up

Figure 3.14: Visualization of the difference in the DOF between the experimental set-ups developed

Static setup

The static setup is composed of the previously described LIM. To precisely constraint the height of the rotor with respect to the stator a set of three ceramic ball bearings are used. These simple Hertzian contacts between the rotor and machined base form a stiff constraint in the normal direction of the machine while

allowing movement in the planar degrees of freedom. As visible in figure 3.13 the ceramic ball bearings are placed in precisely milled slots of the aluminium base. Using three different slot depths and 2 bearing sizes in total 6 fly heights can be tested, ranging from 0.5 mm to 3.0 mm.

Figure 3.15: Static setup used to measure and verify the generated thrust for different heights

Furthermore as can be seen in figure 3.15, to avoid any deformations of the rotor during testing, the rotor is reinforced by an aluminium backing.

Finally the static setup is comprised of a mount to which a Futek load-cell is attached. In this configuration a positive thrust of the rotor can be measured by compression of the load-cell, that is connected to a data-acquisition unit via a Scaime signal amplifier. Further description and verification of the load-cell is described in appendix D.

Dynamic setup

The dynamic setup uses a rotating rotor with a diameter of 400 mm. It is supported at its center of rotation using a specially designed bearing mount (appendix F). For further support two ball bearings are located at the rotors edge constraining the vertical deflection of the rotor.

To measure the rotation of the rotor a 10 bit optical encoder is connected to the center of rotation of the rotor. The quadrature signal returned by the encoder is used to determine the position, speed and direction of the rotor. The angular resolution (R_θ) is described using (3.12).

$$R_\theta = \frac{2\pi}{2^{10}} \approx 6.136 \times 10^{-3}\,\text{rad} = 0.3516° \tag{3.12}$$

The thrust produced by the rotor can, for this setup, also be described using an equivalent toque (3.54) based on the effective arm (r_0) of the force vector. As the translation in the direction of the developed thrust is constraint only an angular acceleration will be obtained.

$$\hat{T} = F_x \cdot r_0 \tag{3.13}$$

3.1.4. Machine validation

Now the machine built a first measurement was done to validate the performance of the machine. For the measurement the static setup will be used in combination with three analog amplifiers (figure 3.17) built for this setup. The negative feedback amplifiers are built of a design by P. Ouwehand [31] for the specifics of which one is referred to appendix C.

The measurements were done under feed-forward current excitation. As seen below in figure 3.18 the thrust curves depicted look like the predicted behavior. The shift with regard to the frequency can be accounted for using the transverse effects described in section 3.1.2. After taking these effects into account

Figure 3.16: Dynamic setup, the rotor made transparent as to show placement of underlying components. The rotor can be see to be supported in the middle by the bearing mount that also contains the rotary encoder

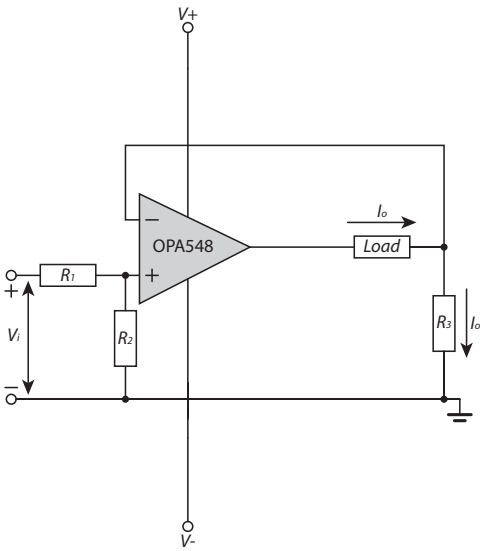

(a) Linear amplifier simplified circuit

(b) Triple amplifier assembly

Figure 3.17: Linear amplifier schematics and assembly used for the initial machine validation

using the proposed decreased effective rotor conductivity [44] and accounting for the new material properties the FEA model matches the measured results closely.

Also depicted in the thrust measurements is the standard devision of the measured thrust. One can see that for the measurements around 30 and 60 Hz the measurements become significantly more spreadout. As explained further in appendix D this is due to an excitation of the eigenfrequency by the thrust harmonic.

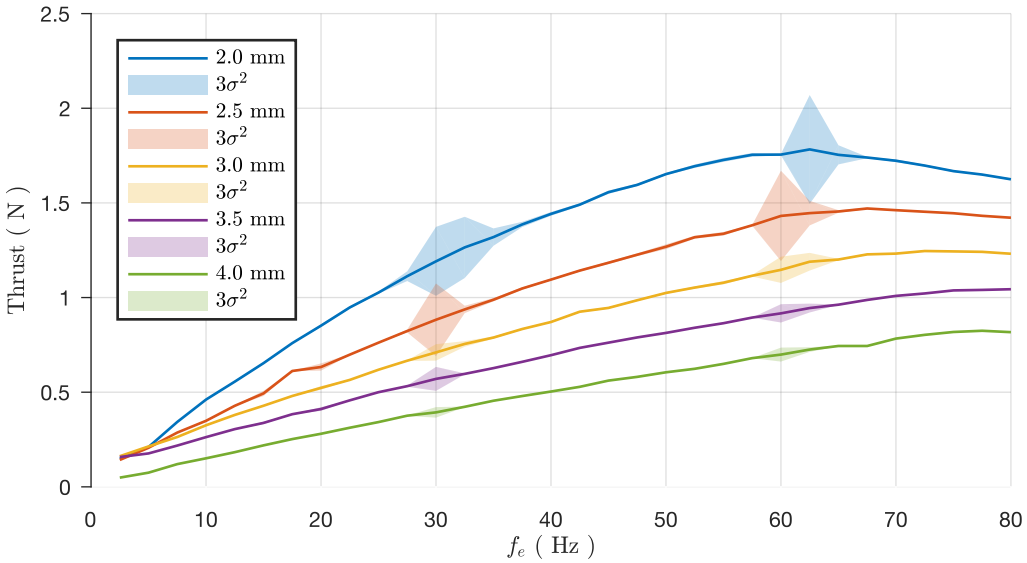

Figure 3.18: Time average thrust measurements with respect to the excitation frequency with an amplitude of 2 A, different curves represent different effective air-gaps. Visible is the increased measurement variance due to excitation of the eigenfrequency of the setup (appendix D)

Comparing the measured response with the predicted values of the machine model one can see that the maximum thrust deteriorates for larger air-gaps as expected (figure 3.19a). The thrust however deteriorates more rapid than expected from the FEA model. The behavior can be explained by the transverse flux leakage that also increases with an increased air-gap. The compensation method described above is however considered constant.

The exponential behavior predicted with respect to the excitation current is also verified. As seen in figure 3.19b the measurements closely match the model although for higher currents the effect of the amplifier saturation (appendix C) is visible.

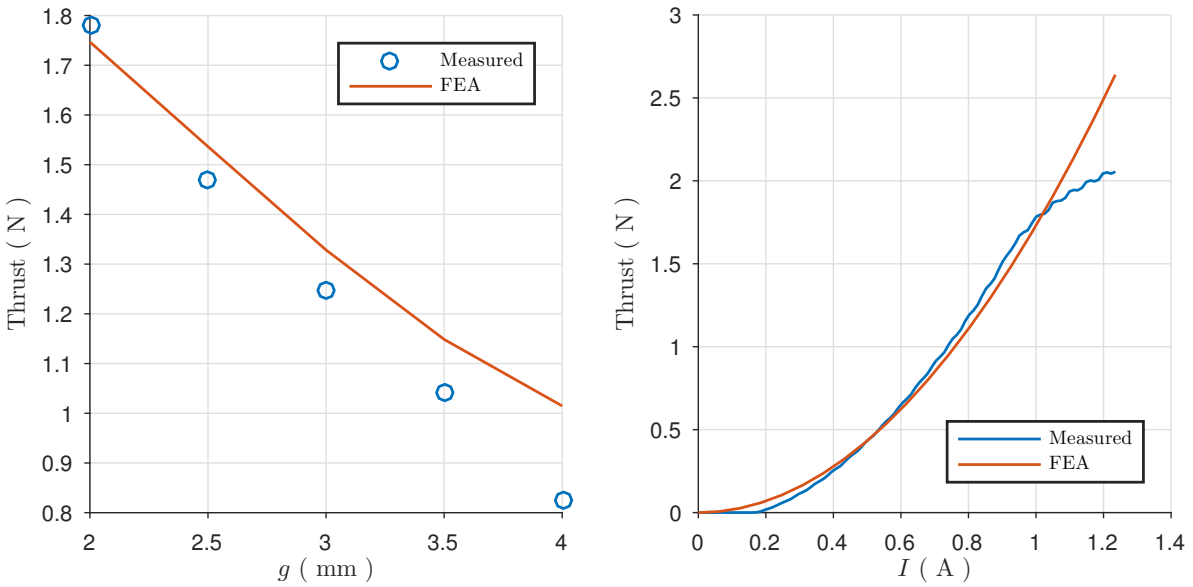

(a) Maximal time average thrust with respect to the effective air-gap, $i_s = 2\,\mathrm{A}$

(b) Time average thrust with respect to winding current, $f_e = 62.5\,\mathrm{Hz}$ and $g = 2\,\mathrm{mm}$. Note the visible saturation of the amplifiers in the high thrust region

Figure 3.19: Thrust comparison between FEA model and empirical data for varying air-gap and current

3.2. Electronics design

To allow for actuation of a LIM, using advanced control strategies discussed in the next section, one should be able to compute and execute the required control effort many thousand times a second. In this section the stock electronics used for this feat will be discussed as well as the theory and techniques used to implement the real-time control.

The initial focus will be put on the real-time micro controller used to perform the time critical elements of the control scheme. Following this the power electronics in the form of a three phase switching inverter will be described with the modulation strategy used. Figure 3.20 depicts the various electronic components and how they are combined into a typical scheme used in actuation of an electrical machine.

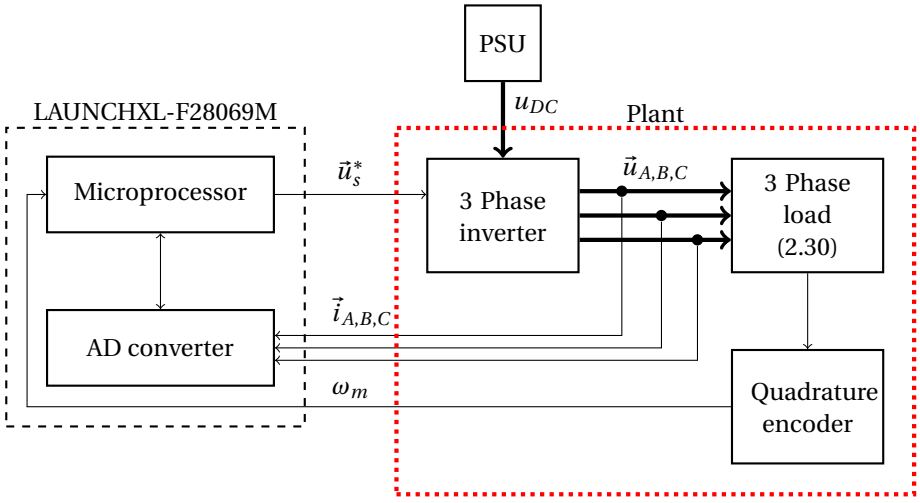

Figure 3.20: Overview of electronic components in a typical real-time controlled electrical machine, high power signals are represented by bold arrows

3.2.1. Real-time hardware

The real-time hardware used is the stock LAUNCHXL-F28069M development board by Texas Instruments. The board has many on-board features that accelerate the development speed possible as the JTAG-emulator for direct access to the live variables and memory. Furthermore the many motor control minded libraries made available for the F2806x micro controllers allow for highly optimized code and avoid reimplementation of standard protocols and algorithms.

The controller has to achieve three main tasks. The first is measurement of the sensor signals needed for control of the LIM. Once the current measurement samples are obtained the control effort must be computed. Finally the modulation signals must be sent to the power inverter for correct delivery of the computed control effort. Additionally the correct logging of various signals is necessary for both development and research.

Timing

The three tasks of the real-time hardware described above have to be accurately executed thousands of times a second. At this time scale even operations as a simple AD-conversion can no longer be neglected.

Figure 3.21 shows the main timing strategy as proposed in by Texas Instruments in their InstaSPIN documentation [18]. The timing is based on a triangle signal build using the CPU clock (here 90 MHz) to trigger an up/down time based counter (TBCTR).

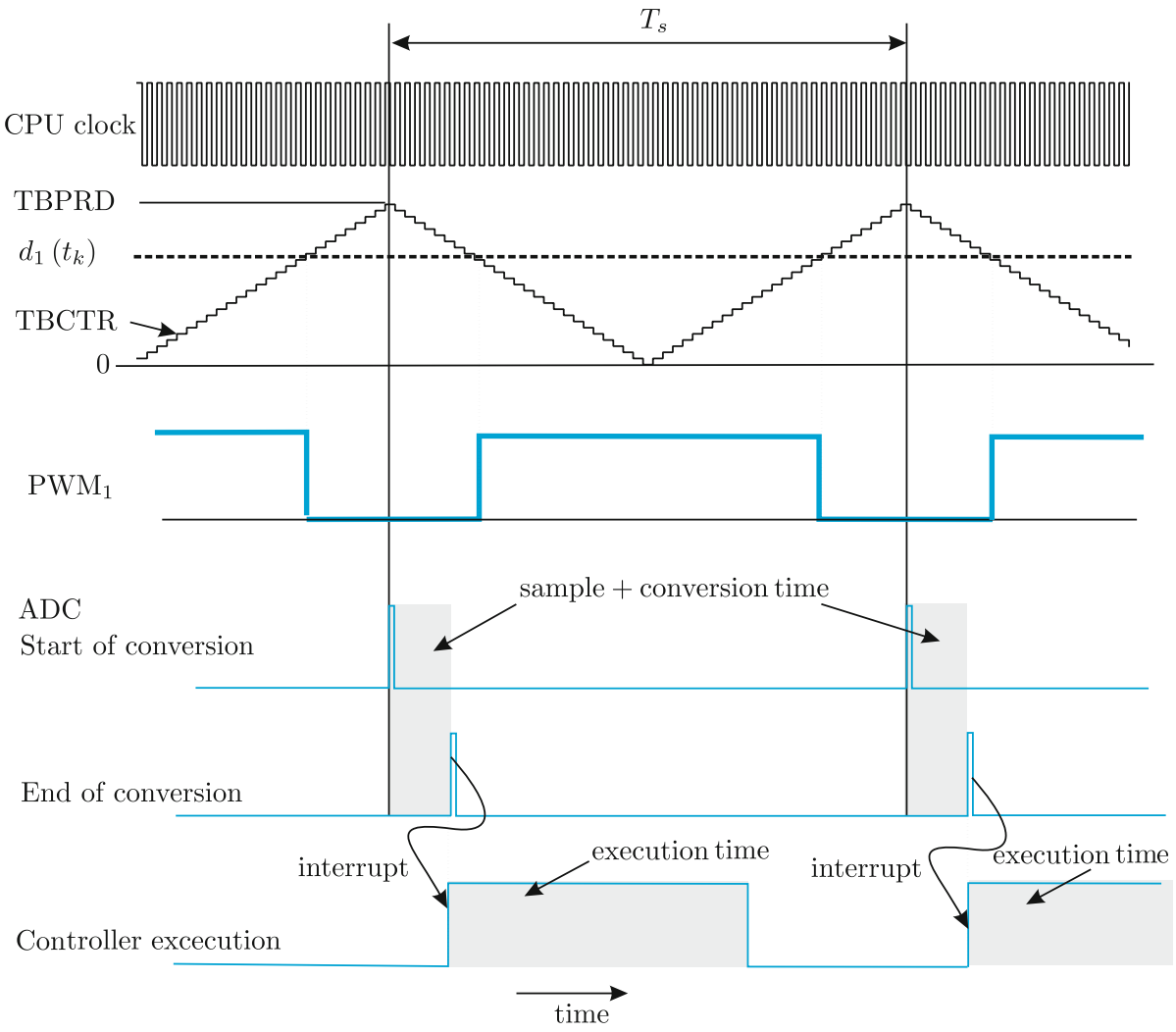

Figure 3.21: Timing scheme used to trigger real-time execution of tasks on the embedded platform [34]

The up/down counter is set to a specific time-based period (TBPRD) that is defined using the required sample-period (T_s). Once the counter reaches the value of the TBPRD, a software interrupt is triggered that both reverses the counter direction and triggers the integration of the AD-converters. Once the last of the AD-

conversions has completed it triggers another interrupt that in turn starts the execution of the implemented controller.

$$TBPRD = \frac{T_s \cdot f_{CPU}}{2} \tag{3.14}$$

Note that the implemented strategy forces the AD-conversions to take place while the modulator signals are switched low, this will be seen to be essential for a correct current measurement. The same TBCTR is used to define the PWM signals as the desired discrete duty cycle for that period ($d(k)$) is directly compared to the TBCTR. Here u_0 is the reference voltage and u_{DC} the DC supply voltage.

$$d(k) = \frac{u^*(k) + u_0}{u_{DC}} \cdot TBPRD \tag{3.15}$$

AD conversions

As shown above the sample period is started with the sampling of the various analog signals for use by the discrete controller. There are two analog to digital converters (ADC) present that can be simultaneously used to sample two separate analog signals. Every sample period the three phase currents, phase voltages, DC current and voltage are all measured two at a time. Of these the current measurements are most time critical and will therefore be sampled first. Below the Simulink/SimMechanics model made of the signal conditioning circuit used for measurement of the phase voltage and current using the 3.3 V ADC of the hardware (figure 3.22).

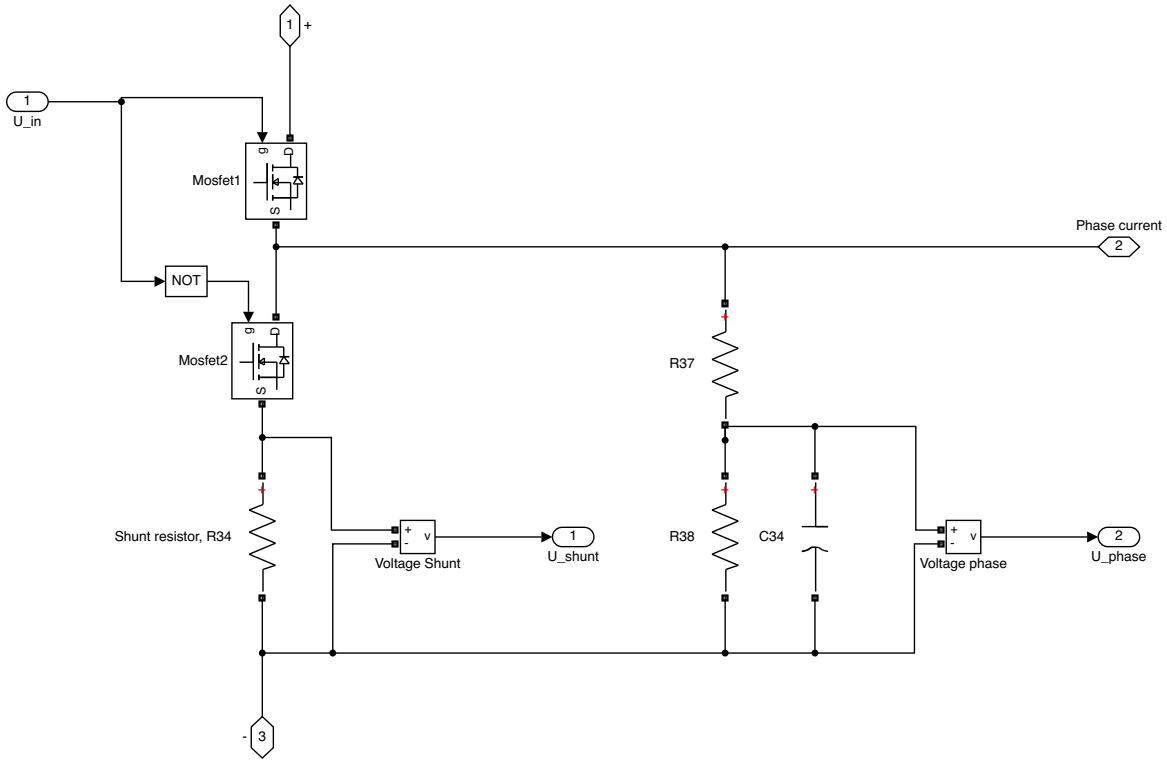

Figure 3.22: Simulink/SimMechanics model of the embedded signal conditioning of the respective phase voltage and current for the ADC. Visible is the low-side shunt resistor for measurement of the phase current and the voltage divider and low-pass filter used for measurement of the phase voltage

As seen, the phase current is measured over a shunt resistor by the ADC. The current measurement is performed on the low-side switch. And although the current is sufficiently filtered by the phase inductance

itself it can only be measured as the low-side switch is active. As the voltage signal is modulated it is first conditioned using a voltage divider and low-pass filter in the form of an RC-circuit shown in figure 3.22. For the hardware used the low-pass filter has a cut-off frequency of 365 Hz. The shunt resistor and voltage divider are designed such that the 12 bit ADC's have a measuring range of 26.314 V and ±16.5 A.

IQ math

To allow for high speed computation on the limited resources provided by the microprocessor while maintaining a high numerical resolution, the use of Texas Instruments IQ math library is used. Below an initial introduction will be given on the often used floating point description of decimal values.

$$\overbrace{S\ \underbrace{eeeeeeee}_{\text{8 bit exponent}}\ \underbrace{fffffffffffffffffffffff}_{\text{23 bit fraction}}}^{\text{32 bit float}} \tag{3.16}$$

A 32 bit floating point description of a decimal value has been widely adopted as the standard due to its large versatility. It can respectively represent very large numbers ($\pm 3.4028 \cdot 10^{38}$) and also very small numbers around zero ($\pm 1.1755 \cdot 10^{-38}$) due to its relative resolution along its range. Furthermore the description is made in such a way it can perform a lossless description of signed integers in the range of $\pm 2^{24}$. The 32 bit representation is depicted in (3.16) where one can see that the first bit is used to determine the sign of the represented decimal value. The following 8 bits describe an integer value called the exponent. The remaining 23 bits describe a decimal value called the fraction.

$$\text{value} = (-1)^S + \underbrace{2^{e-127}}_{\in [2^{-126};2^{127}]} \cdot \underbrace{1.f}_{\subset [1;2-2^{-23}]} \tag{3.17}$$

The decimal value represented by a 32 bit floating point can be computed using (3.17). Here e represents the unsigned integer value given by the exponent bits and $1.f$ is a decimal value of which the decimals are given by the fraction bits.

For the fast arithmetic on a microprocessor, without the need for a dedicated floating-point unit, a so called fixed point representation is used. Using the same 32 bit to describe a decimal value within a certain range, using an absolute resolution. This is done by implicitly describing the location of the decimal point in the unit type.

$$\overbrace{\underbrace{SI}_{\text{2 bit int}}.\underbrace{ffffffffffffffffffffffffffffff}_{\text{30 bit fraction}}}^{\text{32 bit IQ30}} \tag{3.18}$$

Equation (3.18) and (3.19) respectively show the way in which the IQ30 and IQ24 types are defined. As seen, the position of the radix point is defined by the definition of the type itself and thus implicitly divides the significant bits into range and precision.

$$\overbrace{\underbrace{SIIIIIII}_{\text{8 bit int}}.\underbrace{ffffffffffffffffffffffff}_{\text{24 bit fraction}}}^{\text{32 bit IQ24}} \tag{3.19}$$

The integer bits represent the signed integer that describes the pre-radix point value of the decimal value. The fraction bits represent the decimals with a certain precision defined by the IQ type used. Comparing the range and precision of the different types is done in table 3.1.

To allow for efficient computation, variables will be converted to a fixed point representation using a certain gain called the full-scale value (x_{fs}). One can thus map a variable with a certain value x to a per-unit value (x_n) that covers the entire range of its fixed point type.

Table 3.1: Comparison of floating point and fixed point representations

Type	Maximal value	Minimal value	Significant bits	Resolution
float	$2^{128} \cdot (1-2^{-23}) \approx 3.4028 \cdot 10^{38}$	$\approx -3.4028 \cdot 10^{38}$	24	$2^{-24} \cdot 2^{e-127}$
IQ30	$2-2^{-30} \approx 2$	-2	32	$2^{-30} \approx 9.3132 \cdot 10^{-10}$
IQ24	$128-2^{-24} \approx 128$	-128	32	$2^{-24} \approx 5.9605 \cdot 10^{-8}$

$$x_n = \frac{x}{x_{fs}} \tag{3.20}$$

$$y_n = \underbrace{K \cdot \frac{x_{fs}}{y_{fs}}}_{K_n} \cdot x_n \tag{3.21}$$

Simple arithmetic can now simply be done using the fast IQ math operations on the per-unit values. Where for multiplication and devisions one should account for the appropriate full-scale values of the in and output variables. Multiplying a value with a certain gain K is shown in (3.21) where the gain in the per-unit domain needs to be scaled accordingly using the full-scale values.

3.2.2. Power electronics

The power electronics execute the computed control effort using high power signals, above the tolerances that can be handled by the microprocessor directly. The implementation is done using a stock three phase inverter by Texas Instruments, the BOOSTXL-DRV8301. It is based on a DRV8301 gate driver in combination with six NexFET Power MOSFETs in a triple half-bridge configuration. Below a description is given of the workings of a triple half-bridge inverter followed by the switching strategy that will be used.

Triple half-bridge inverter

A three phase inverter is comprised of a set of 6 unipolar switches that, when correctly switched, can be used to drive a three phase load. Figure 3.23 shows a schematic representation of such an arrangement of switches, where the phase terminals u_A, u_B and u_C are respectively connected to the three-phase load.

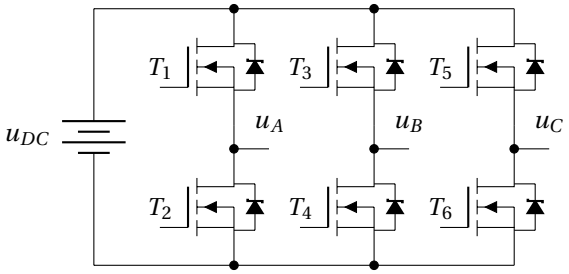

Figure 3.23: Triple half-bridge inverter comprised of six unipolar switches

The pair of switches connected to a single phase are always switched in pairs. Meaning that if the T_1 is switched low, T_2 will be switched high. A small intermediate period called the dead-time exists for which both switches will be switched low to avoid a short of the source lines. Defining the neutral as half of the source voltage (u_{DC}) one can connect the respective phases to either $+\frac{u_{DC}}{2}$ or $-\frac{u_{DC}}{2}$ by switching the respective pair of switches. Using a pulse width modulated (PWM) representation of the phase reference voltage one can approximate any phase voltage within the source limits. As can be seen in (3.22) only the average of the PWM controlled voltage over a sample period can be controlled, if the sample frequency is chosen fast enough this approximation is however sufficient.

$$u(k) = \frac{1}{T_s} \int_{t=t_k}^{t=t_k+T_s} u(t)\,dt \tag{3.22}$$

In figure 3.24 one can see an example of such a PWM represented voltage signal. After conditioning of the signal (figure 3.22) the applied reference sine of 10 Hz is recovered.

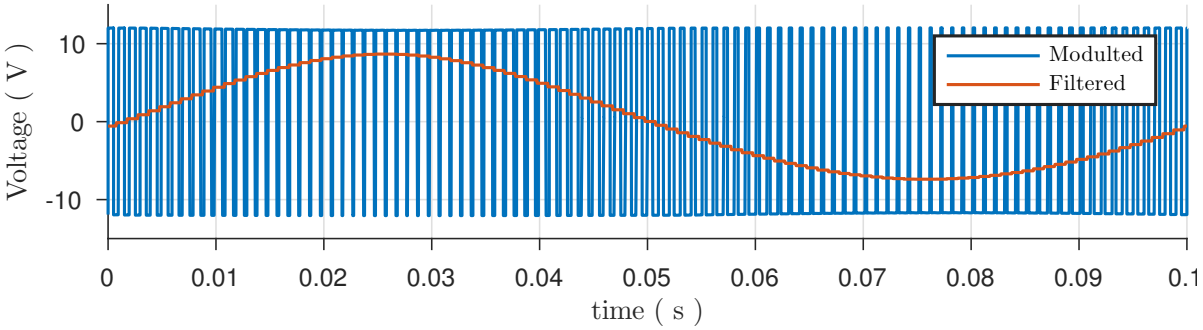

Figure 3.24: Pulse width modulated voltage description, and the measured signal after filtering

Space vector pulse width modulation

Using (3.22) to define the three inverter outputs (u_A, u_B and u_C) one could describe the resulting phase voltages as a (u_{AN}, u_{BN} and u_{CN}) using (3.24). Here u_{NO} is the voltage between the neutral line of the star connected load to the ground defined as (3.23).

$$u_0 = \frac{1}{2} u_{\mathrm{DC}} \tag{3.23}$$

$$\begin{bmatrix} u_{AN} \\ u_{BN} \\ u_{CN} \end{bmatrix} = \begin{bmatrix} u_A \\ u_B \\ u_C \end{bmatrix} + u_{N0} \tag{3.24}$$

The most straightforward approach to develop a rotating voltage vector using PWM would be to use a static neutral at $u_{N0} = \frac{1}{2} u_{DC}$. Applying a set of three sinusoidal voltages to the inverter outputs would in turn cause three sinusoidal phase voltages. This approach allows one to describe a voltage vector with a radius of $u_s = \frac{1}{2} u_{DC}$. Space vector modulation improves this range by changing the neutral voltage as the winding voltages are described by (3.24).

Space vector modulation of the inverter directly converts a given reference space vector into the modulation indexes used to switch the bridges. For this the possible inverter states are described in the space vector reference frame. A set of eight possible inverter states exist, each linked to a respective state of the six switches as depicted in table 3.2.

Table 3.2: Space voltage vectors expressed in the state of the respective inverter switches

Vector	T1	T2	T3	T4	T5	T6
(000)	OFF	ON	OFF	ON	OFF	ON
(100)	ON	OFF	OFF	ON	OFF	ON
(110)	ON	OFF	ON	OFF	OFF	ON
(010)	OFF	ON	ON	OFF	OFF	ON
(011)	OFF	ON	ON	OFF	ON	OFF
(001)	OFF	ON	OFF	ON	ON	OFF
(101)	ON	OFF	OFF	ON	ON	OFF
(111)	ON	OFF	ON	OFF	ON	OFF

If one represents these possible vectors as space vectors, with (000) and (111) being the non-active/zero-vectors, one obtains the representation in figure 3.25a. As seen any reference voltage vector can be described using a combination of 2 of the inverter vectors with the possible addition of the zero-vectors.

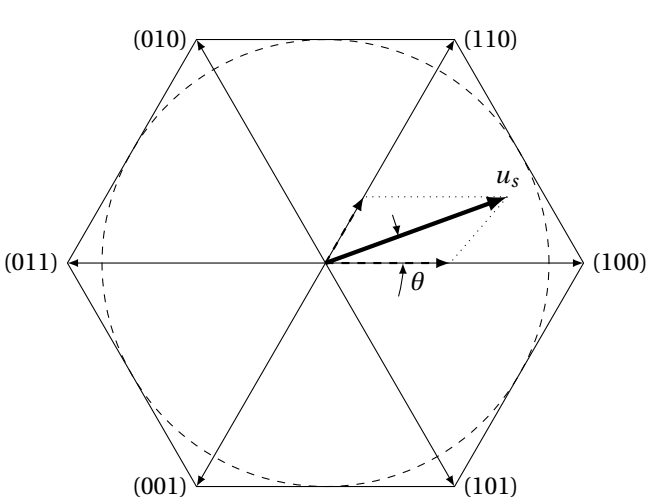

(a) Space vector description of the voltage vectors and a stator voltage in the first section, consisting of a (100) and (110) component

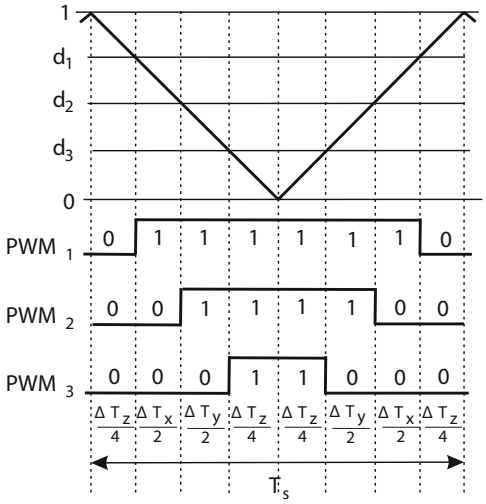

(b) Centered PWM derivation from TBCTR

Figure 3.25: Space vector modulation visualized both as space vectors and in time domain

Figure 3.25b depicts the response of the PWM signals in time domain. As one can see the PWM signal describes a set of four inverter vectors. Initially all bridges are turned low (000), followed by a period (T_x) with a single high bridge (100), a period (T_y) where two bridges are in the high position (110) and finally the second zero vector (111). Also visible is the fact that the modulation pulses are centered around the TBCTR.

Table 3.3 gives the line-to-line voltages defined by the inverter terminals. Considering a star connected load with equal phase resistance one can compute from this the phase voltages. The thing to note being that the neutral voltage is no longer constant and equal to ground ($u_{N0} \neq 0$).

Since u_{N0} can be none-zero when using SVPWM one can describe a voltage vector with an amplitude that is larger than $\frac{u_{DC}}{2}$ as was to be expected from (3.24). The floating neutral has an offset of $u_{N0} = \pm\frac{1}{6}u_{DC}$. The centering of the PWM modulation visible in figure 3.25b in practice centers the required line-to-line voltage in the center of the source voltage. Resulting in the full source voltage to be available to describe a line-to-line voltage.

Table 3.3: Space vector voltages in u_{DC} V

Vector	u_{AB}	u_{BC}	u_{CA}	u_{AN}	u_{BN}	u_{CN}	u_{N0}
(000)	0	0	0	0	0	0	0
(100)	1	0	-1	2/3	-1/3	-1/3	-1/6
(110)	0	1	-1	1/3	1/3	-2/3	1/6
(010)	-1	1	0	-1/3	2/3	-1/3	-1/6
(011)	-1	0	1	-2/3	1/3	1/3	1/6
(001)	0	-1	1	-1/3	-1/3	2/3	-1/6
(101)	1	-1	0	1/3	-2/3	1/3	1/6
(111)	0	0	0	0	0	0	0

The dashed inscribed circle (figure 3.25a) describes the maximal radius (3.25) that can be obtained without over-modulation. Using the full range of the supply voltage, one can further extend the amplitude to within the hexagon depicted in figure 3.25a. Note that even without over-modulation the maximum voltage amplitude is increased from $\frac{u_{DC}}{2}$ to $\frac{U_{DC}}{\sqrt{3}}$ ($\approx 15\,\%$) by using space vector modulations.

$$u_{s,\max} = u_{DC}\frac{2}{3}\cdot\cos\left(\frac{\pi}{6}\right) = u_{DC}\frac{1}{\sqrt{3}} \tag{3.25}$$

3.3. Control design

To allow for a precise tracking of certain machine states (in this case the stator current and rotor position) to the desired reference state, a variety of controllers are used in the actuation scheme. The control of AC machines has made great advancements since the 1980s, when the use of solid-state electronics popularized. It allowed for the implementation of cost-effective power electronics and microcontrollers [26].

In this section an introduction will be given on both scalar control and field oriented control of induction machines. After which the various steps of implementing the chosen, indirect field oriented, control method is covered more thoroughly. The implemented controller is based on the theory and material from [34]. Note the control strategies covered here are all so-called "sensored" control schemes, meaning that the mechanical rotor position is measured and used in control. Heavy research is being done on the implementation of both scalar control and field oriented control schemes in "sensorless" form.

3.3.1. Scalar control

The scalar control, often cold Volt-Hertz control, is the most simple control used for induction machines. The concept is based on the idea of keeping the motor flux constant within the machine for any steady-state of the machine.

This is done based on the linear per phase model described earlier (figure 2.29). Within the linear regime of the model and assuming low slip ($s \approx 0$) one can describe flux producing current (current component linear related to the magnetic flux, i_d) using (3.26) [17].

$$i_d = \frac{u_s}{R_s + \omega_e \cdot L_s} \approx \frac{u_s}{\omega_e \cdot L_s} \tag{3.26}$$

Here L_s is the total self inductance of the motor ($L_\sigma + L_M$). As can be seen under the assumption that R_s can be neglected one can see that flux producing current will stay constant for a constant ratio of u_s to ω_e. It is this constant relation that the Volt-Hertz controller borrows its name from.

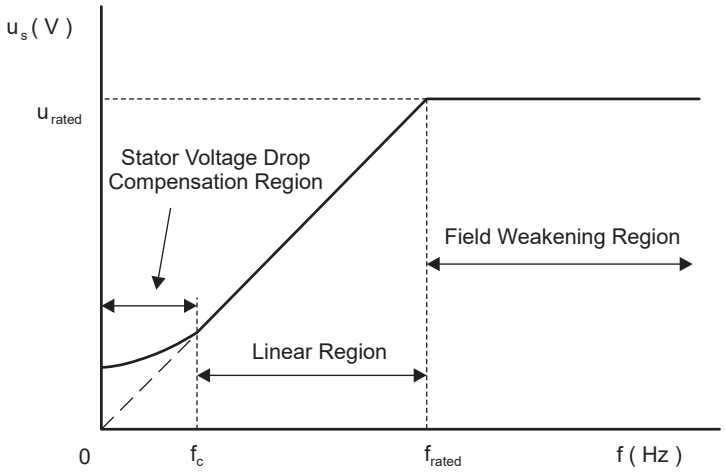

Figure 3.26: Stator voltage with respect to frequency under Volt-Hetz control [17]

Figure 3.26 shows the relationship between the stator voltage and the electrical frequency, in which three regions are distinguishable. First is the non-linear domain ($f_e < f_c = \frac{R_s}{2\pi \cdot L_s}$) in which the stator resistance (R_s) can not be neglected. Second is the linear region for which the main control scheme is developed, recognized by the constant slope. Third and final is the region for which field weakening has to be applied as not to damage the stator coils.

The diagram depicted in figure 3.27 shows an implementation of scalar control in a velocity controller. The difference between the velocity reference (ω_m^*) and the measured velocity (ω_m) is fed to a PI-controller to obtain the desired slip frequency. The derived electrical frequency (ω_e) is then simply fed back to the Volt-Hertz regulator to obtain the desired voltage vector. Although extremely simple to implement, scalar control is regarded most suitable for steady-state operation only [20].

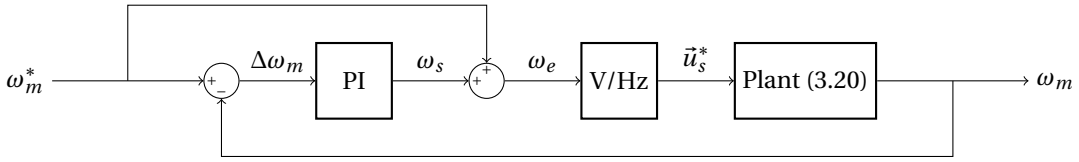

Figure 3.27: Closed loop scalar velocity controller

3.3.2. Field oriented control

Field oriented control uses the same linearity between flux and rotor current (2.4) as scalar control does. However instead of performing control on the three phase signals directly, the signals are first converted to a more convenient reference frame. In this rotating reference frame the two orthogonal current components respectively describe the magnetic flux and the induced rotor currents. This allows for direct control of an induction motors torque/thrust and thus similar behavior as that of a DC motor.

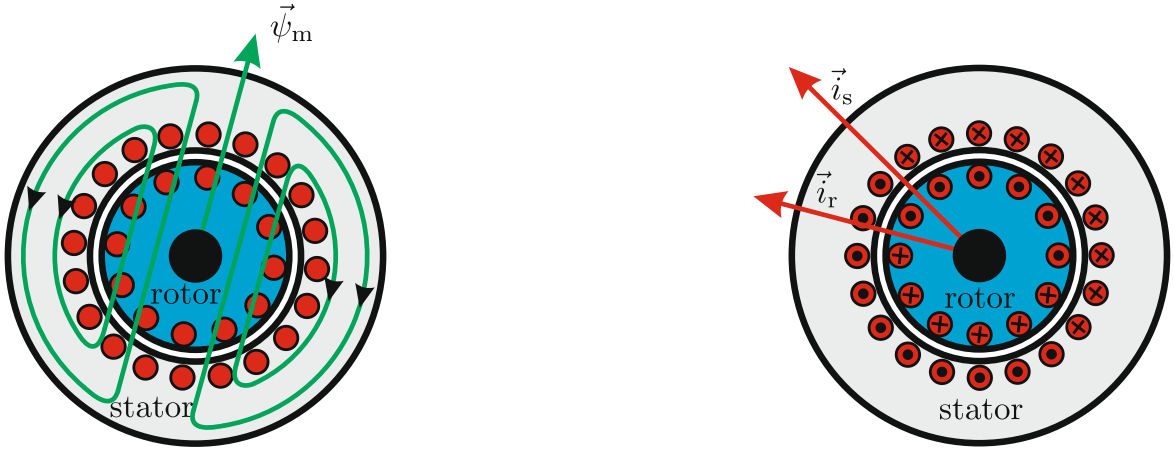

(a) Motor flux distribution

(b) Motor current distribution

Figure 3.28: Motor flux and current distribution in a single pole pair IM under excitation of a stator current $\vec{i}_s$ [8]

In figure 3.28 the section of a single pole pair induction machine is again depicted in line with a space vector frame. One can see that the stator current vector ($\vec{i}_s$) depicted in figure 3.28b produces a rotor current vector ($\vec{i}_r$) that is perpendicular to the flux vector ($\vec{\psi}_m$) shown in figure 3.28a.

Note that in reality the rotor current distribution is reversed to the notation convention. As the permeability of the motor approaches infinity and the air-gap approaches zero, this will result in the stator magneto-motive forces (MMF) to be equal to the rotor MMF [8].

Figure 3.29 shows the three reference frames used in field oriented control. As one can see, initially the space vector is described in the abc-frame that matches the three phases of an induction machine. This time and speed dependent three coordinate signal is transformed to a two coordinate signal in the $\alpha\beta$-frame, using the Clarke transform. This signal is then transformed to a time and speed invariant signal using the Park transform. The dq-frame is a rotating frame that is field oriented, meaning that the d-axis of the frame is aligned with the magnetic flux axis.

Clarke transform

The Clarke transform allows for the description of the stator current in a static reference frame with only two orthogonal components (i_α and i_β) [10]. Initially the stator current will be described by the three phase components as in (3.27).

$$\vec{i}_s = \begin{bmatrix} i_A & i_B & i_C \end{bmatrix}^T \tag{3.27}$$

As can be seen in figure 3.29b the i_α is in line with the i_a component of the three phase frame. The $\alpha\beta$-frame can thus be described as follows:

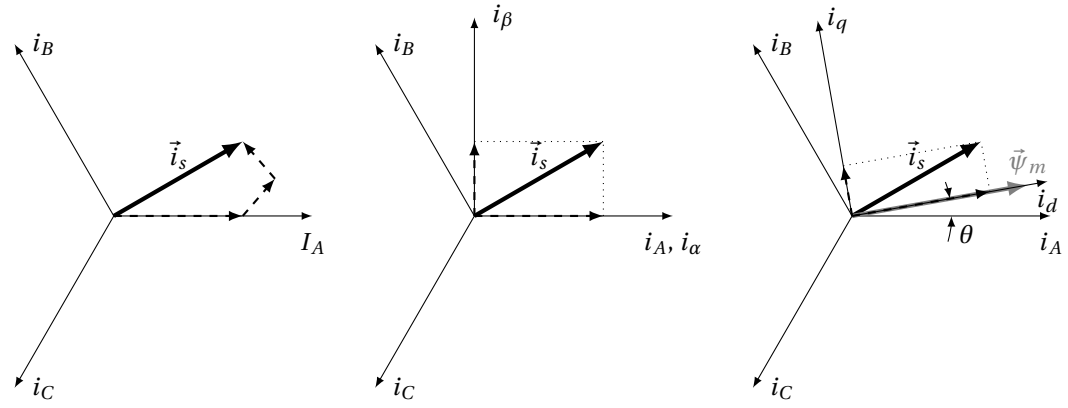

(a) abc reference frame (b) $\alpha\beta$ reference frame (c) dq reference frame

Figure 3.29: Current vector depicted in the three reference frames used in FOC

$$\begin{bmatrix} \vec{i}_\alpha \\ \vec{i}_\beta \end{bmatrix} = \begin{bmatrix} 1 & 0 & 0 \\ \frac{1}{\sqrt{3}} & \frac{2}{\sqrt{3}} & 0 \end{bmatrix} \cdot \begin{bmatrix} \vec{i}_A \\ \vec{i}_B \\ \vec{i}_B \end{bmatrix} \tag{3.28}$$

The Clark transform can now be used to convert the stator current between these two reference frames. Note that in the $\alpha\beta$-frame the stator current is still time and speed variant. Below both the forward (3.29) and inverse (3.30) Clarke transform are given in their simplified form as described in [40].

$$\begin{bmatrix} i_\alpha \\ i_\beta \end{bmatrix} = \frac{2}{3} \begin{bmatrix} 1 & -\frac{1}{2} & -\frac{1}{2} \\ 0 & \frac{\sqrt{3}}{2} & -\frac{\sqrt{3}}{2} \end{bmatrix} \cdot \begin{bmatrix} i_A \\ i_B \\ i_C \end{bmatrix} \tag{3.29}$$

$$\begin{bmatrix} i_A \\ i_B \\ i_C \end{bmatrix} = \frac{3}{2} \begin{bmatrix} \frac{2}{3} & 0 \\ -\frac{1}{3} & \frac{\sqrt{3}}{3} \\ -\frac{1}{3} & -\frac{\sqrt{3}}{3} \end{bmatrix} \cdot \begin{bmatrix} i_\alpha \\ i_\beta \end{bmatrix} \tag{3.30}$$

Although the current amplitude is invariant over this computation, the (reactive) power is not. For power computations in the Clarke reference frame it is therefore advised to use the power invariant variation as proposed in [7]. Throughout this thesis the amplitude invariant transformations will be used.

Parke transform

The Parke transform as proposed by R.H. Parke [32] transforms the stator current from the $\alpha\beta$-frame to a rotating reference frame. The Parke reference frame comprised of two orthogonal components (i_d and i_q) of which the former is aligned with the motors magnetic flux axis ($\vec{\psi}_m$) as depicted in figure 3.29c. In this representation the signal is both time and speed independent during steady state operation.

$$\begin{bmatrix} i_d \\ i_q \end{bmatrix} = \begin{bmatrix} \cos(\theta) & \sin(\theta) \\ -\sin(\theta) & \cos(\theta) \end{bmatrix} \cdot \begin{bmatrix} i_\alpha \\ i_\beta \end{bmatrix} \tag{3.31}$$

(3.31) describes the Parke transformation and (3.32) describes the inverse. In the Parke reference frame the direct current is responsible for the magnetic flux and the quadrature component is directly proportional to the thrust.

$$\begin{bmatrix} i_\alpha \\ i_\beta \end{bmatrix} = \begin{bmatrix} \cos(\theta) & -\sin(\theta) \\ \sin(\theta) & \cos(\theta) \end{bmatrix} \cdot \begin{bmatrix} i_d \\ i_q \end{bmatrix} \tag{3.32}$$

Note that both the Parke and the inverse Parke transformation need the phase of motor flux axis (θ). In an induction motor, this is not equal to the rotor position but the slip frequency will have to be taken into account.

Although mentioned for completeness above, the inverse Parke transform will not be used in the final implementation. The $\alpha\beta$ signal description will be directly used as input for space vector modulation described earlier.

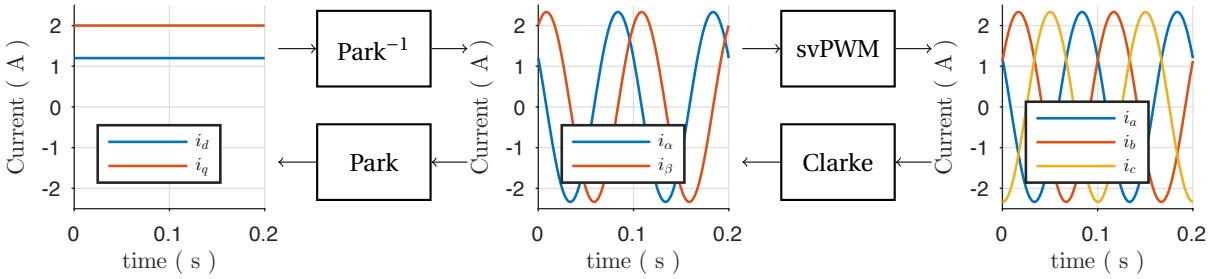

Figure 3.30: Overview of the phase signal as they are transformed between the different reference frames

Figure 3.30 gives an overview of the various signals and transformations involved in FOC. The physical system is linked to the signals on the right-hand side of the figure, while control is performed on the signals in the left-hand side.

Note that the limiting factor in FOC as a control method is that for the (inverse) Park transform one needs the rotor flux angle (θ). This is a physical quantity that can either be directly measured from the machine flux or estimated from other motor parameters.

Direct FOC

Direct field oriented control uses either sensing coils or hall-effect sensors to get a direct measurement of the magnetic flux density in the machine [28]. Although this method for estimating the magnetic flux axis often gives the most accurate results, it is often omitted for more practical reasons. The increased complexity and cost of the sensor system and control electronics in combination with the often poor flux measurements at low speeds, are some of the disadvantages of a direct FOC method [5].

Indirect FOC

Indirect field oriented control uses a motor model to make an estimate of the motor flux axis ($\hat{\theta}$). Using the per phase equivalent motor model, one can describe the motor slip estimate using the functions below [8].

$$\psi_r^* = i_d^* \cdot L_M \tag{3.33}$$

$$\hat{\omega}_s = \frac{i_q^* \cdot R_R}{\psi_r^*} \tag{3.34}$$

$$\omega_e^* = p \cdot \omega_m + \hat{\omega}_s \tag{3.35}$$

One can thus describe the flux axis estimator using the scheme depicted below in figure 3.31. One can see indirect FOC only needs a measurement of the mechanical rotor velocity to make an estimate of the machine flux axis.

3.3.3. Current controller

Using the three phase inverter one can develop a PWM approximated voltage vector. For accurate control of the motor thrust one however requires an accurate current vector. It is for this reason the final position controller has an internal current loop. In this section the dynamics and tuning of the internal current loop will be described.

Generic RL-load controller

To accurately follow the reference current (i^*) a model based controller is used [34]. In simplified form it has the form of a standard PI controller with a discrete sampling time (T_s) that is tuned based on the L-R per phase load model taking the discrete sampling time into account (figure 3.32).

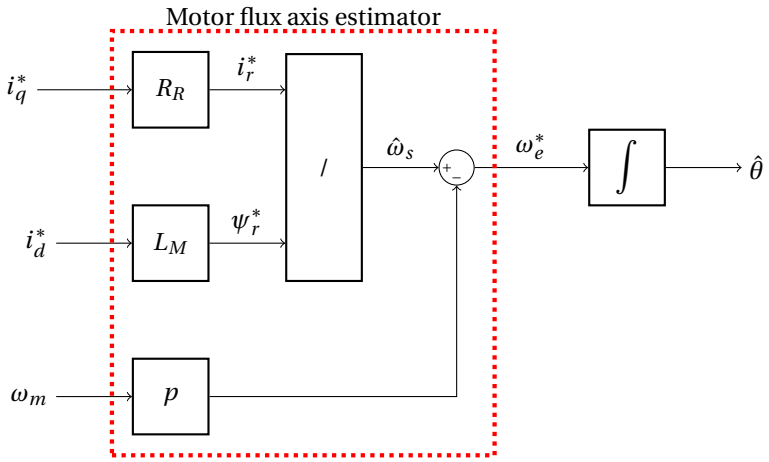

Figure 3.31: Block diagram of machines flux axis estimator

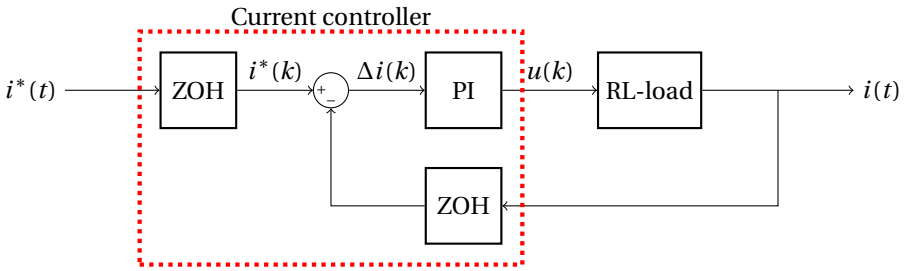

Figure 3.32: Current controller in discrete time

The idea is based on the current behavior of a L-R load. In its continuous deferential form this is defined as (3.36). In reality both the input and the output of the controller are discrete signals. One can however approximate the output of the switching inverter by its time average over a sample period (3.22).

$$u(t) = R \cdot i(t) + L \cdot \frac{di}{dt} \tag{3.36}$$

Figure 3.33 depicts the current behavior of the desired controlled current. For a certain time sample (k = 1, 2, 3, etc.) the controller defines the current error as the difference between the current reference and the measured current at the sample time: $\Delta i(k) = i^*(t_k) - i(t_k)$.

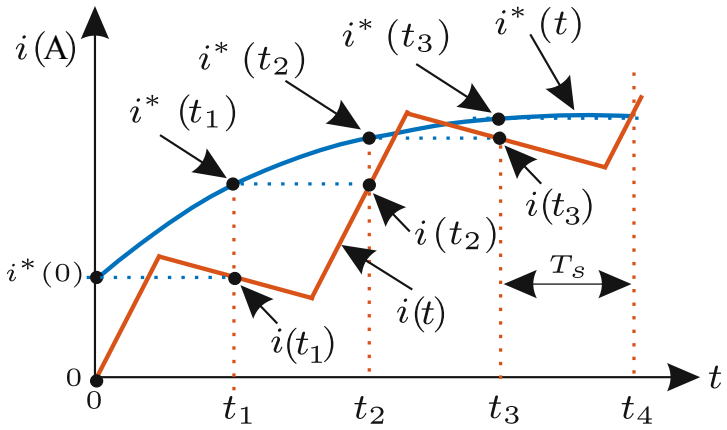

Figure 3.33: Current behavior under current controller (— continuous signal, - - sampled signal) [34]

The objective of the current controller is to determine the required stator voltage to reduce the current error at the start of the sample period ($\Delta i(k)$) to zero at the end of the sample period (3.37).

$$i(t_k + T_s) = i^*(t_k) \tag{3.37}$$

The required average voltage that is necessary to achieve the control objective described above can be defined as (3.38).

$$u(k) = \frac{R}{T_s}\int_{t_k}^{t_{k+1}} i(t)\,dt + \frac{L}{T_s}\int_{i(t_k)}^{i(t_{k+1})} di \tag{3.38}$$

Using the equation above one can thus with a detailed knowledge of the load derive the exact average current necessary. In the absence of any disturbance and a small enough sampling period, a near perfect current reference tracking can be obtained.

In reality the (3.37) is often discretized for implementation. Under the assumption T_s is chosen sufficiently small the first order approximation (3.39) gives good results.

$$u(k) \approx R \cdot i(t_k) + \frac{R}{2}\Delta i(k) + \frac{L}{T_s}\Delta i(k) \tag{3.39}$$

One can see from figure 3.33 that if the current objective is achieved, and the error is reduced to zero at the end of every sample period, one can describe the measured current at the start of the sample time by the sum of the all previous errors.

$$i(t_k) \approx \sum_{n=0}^{n=k-1} \left(i^*(t_n) - i(t_n)\right) \tag{3.40}$$

Assuming $t_0 = 0$ and $i(t_0) = 0$ the equation above can finally be used to rewrite (3.39) in the form of a standard PI controller (3.41). With $K_p = \frac{L}{T_s} + \frac{R}{2}$ and $K_i = \frac{R}{T_s}$.

$$u^*(k) = R\sum_{n=0}^{n=k-1} (\Delta i(t_n)) + \left(\frac{L}{T_s} + \frac{R}{2}\right) \cdot \Delta i(t_k) \tag{3.41}$$

Because in practice $\frac{R}{2} < \frac{L}{T_s}$ the term $\frac{R}{2}$ is considered negligible, resulting in the following description of the current controller and discrete control gains.

$$u^*(k) = K_p \cdot \Delta i(k) \cdot (1 + \omega_i T_s) + R \cdot i(t_k) \tag{3.42}$$

$$K_p = \frac{L}{T_s} \tag{3.43}$$

$$\omega_i = \frac{R}{L} \tag{3.44}$$

Figure 3.34 shows the behavior of the controlled current for a reference step. As one can see, the simulated current tracks the reference extremely well even for this exaggerated large sample time. A small modeling error is introduced in the form of switching dead-time, the integrating nature of the controller however still reduces the error to zero. If no a priori knowledge of the machine is available, one could resort to other control strategies for instance hysteresis control.

Three phase load controller

For a general star connected three phase load as described in the modeling section (figure 2.30) one can perform a similar derivation to the one in the previous section. The control is now developed for the control of a space vector of which the objective function is described as (3.45). Note the back EMF is here neglected and will thus be compensated for as if it where a disturbance.

$$\vec{i}(t_k + T_s) = \vec{i}^*(t_k) \tag{3.45}$$

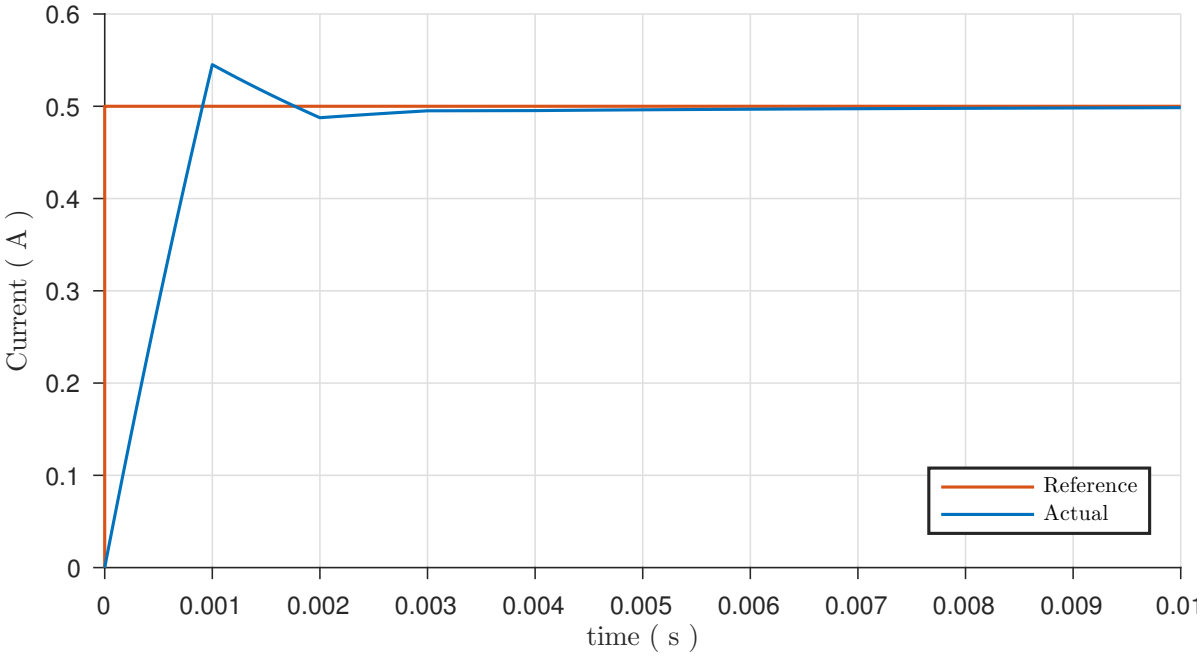

Figure 3.34: Step response of current controlled load, $R = 2.8\,\Omega$, $L = 13.6\,\text{mH}$ and $\frac{1}{T_s} = 1\,\text{kHz}$

The controllers will be applied in the rotating dq-frame, (3.36) for this space vector representation the load can be defined as (3.46). Furthermore under the assumption that $\frac{1}{T_s} >> \omega_e$ the approximation of the sample period average (3.47) of the inverter voltage vector holds.

$$\vec{u}_{dq}(t) = R \cdot \vec{i}_{dq} + L\frac{d\vec{i}_{dq}}{dt} + j\omega_e L \cdot \vec{i}_{dq} \tag{3.46}$$

$$\vec{u}_{dq}(k) = \int_{t_k}^{t_{k+1}} u_{dq}(t)\,dt \tag{3.47}$$

One can derive the two orthogonal voltage components necessary to achieve (3.45) and see that apart from the cross-coupling (caused by $j\omega_e L\vec{i}_{dq}$) the two current components are equal to that of the earlier described generic RL load.

$$u_d(k) = \frac{R}{T_s}\int_{t_k}^{t_{k+1}} i_d(t)\,dt + \frac{L}{T_s}\int_{i_d(t_k)}^{i_d(t_{k+1})} di_d - \frac{1}{T_s}\int_{t_k}^{t_{k+1}} \omega_e L \cdot i_q(t)\,dt \tag{3.48}$$

$$u_q(k) = \frac{R}{T_s}\int_{t_k}^{t_{k+1}} i_q(t)\,dt + \frac{L}{T_s}\int_{i_q(t_k)}^{i_q(t_{k+1})} di_q + \frac{1}{T_s}\int_{t_k}^{t_{k+1}} \omega_e L \cdot i_d(t)\,dt \tag{3.49}$$

Furthermore also the discretization used before can be directly applied on the equations above resulting in the two discrete controllers shown below. As one can see, apart from the cross-coupling term the exact same controller gains can be used as for a single generalized load described before.

$$u_d^*(k) = K_p \cdot \Delta i_d(k) \cdot (1 + \omega_i T_s) + R \cdot i_d(t_k) - \omega_e L \cdot \vec{i}_q(t_k) \tag{3.50}$$

$$u_q^*(k) = K_p \cdot \Delta i_q(k) \cdot (1 + \omega_i T_s) + R \cdot i_q(t_k) + \omega_e L \cdot \vec{i}_d(t_k) \tag{3.51}$$

Depicting the control strategy above results in the block diagram shown in figure 3.35. The space vector transformations covered in the introduction are here depicted in a single forward and inverse block.

Three phase current control verification

To verify the behavior of the designed current controller, it was implemented on the embedded hardware described before, using the solidThinking embed development environment. The controller gains are used

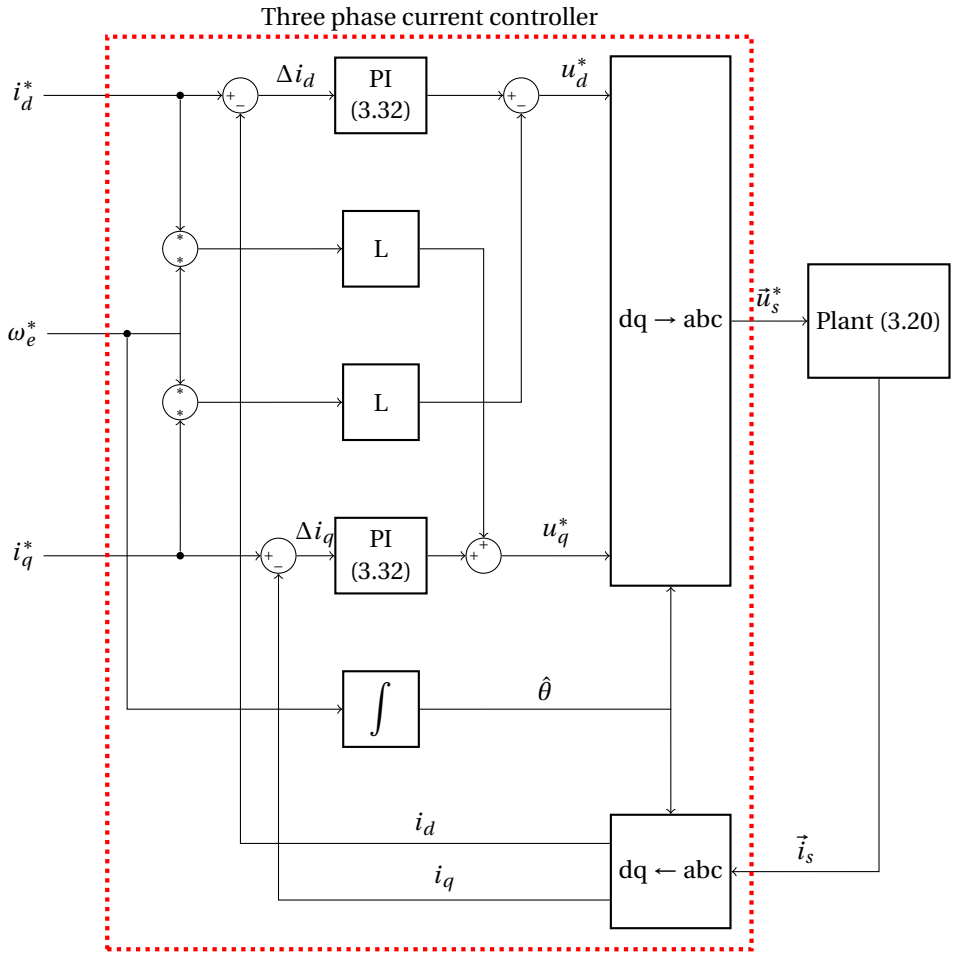

Figure 3.35: Three phase current controller in the dq reference frame

as an upper limit and slightly downscaled to move more of the control effort from the feed-forward gain to the integrating part of the component. The resulting controller is thus chosen to be more robust against model inaccuracies, in the trade-off with speed.

Table 3.4: Controller parameters of the implemented current controller

Parameter	Value	Units
K_p	25.00	V/A
ω_i	206.60	rad/s

Using the control parameters used in table 3.4 a reference signal can be tracked accurately. Figure 3.36a shows the tracking of such a reference signal described by: $i_s^* = 2\,\text{A}$, $\omega_e^* = 10\,\text{Hz}$.

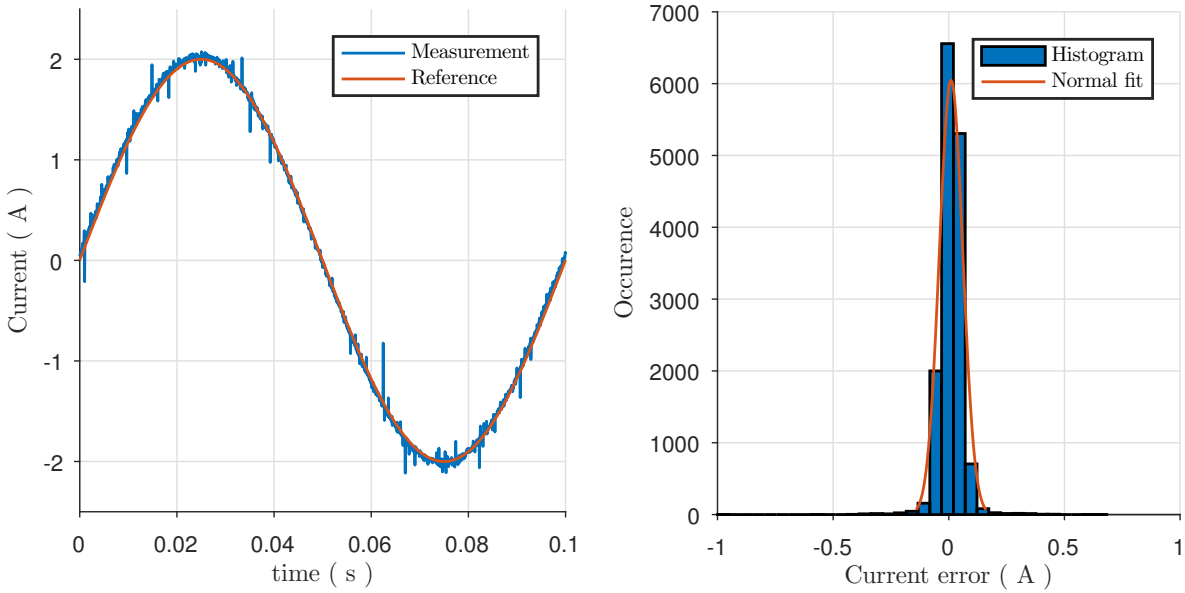

(a) Response depicted using i_α component

(b) Tracking error distribution

Figure 3.36: Tracking response of an example current vector, $i_s^* = 2\,\text{A}$, $\omega_e^* = 10\,\text{Hz}$

As seen in figure 3.36b the noise for this signal with a large amplitude can still be tracked with a precision of 0.15 A (3σ).

One can also perform a more thorough analysis of the current response in the frequency domain. Note that here the varying frequency is the electrical reference frequency (ω_e^*) and the amplitude of the reference signal is kept constant throughout. Below the frequency response of such an analysis is given for both the physical system and a component level model of the plant using MathWorks Simulink.

As can be seen for an amplitude of 0.5 A the cut-off frequency of the model accurately describes the physical system. This bandwidth however decreases for larger amplitudes as the inverter is saturates. In practice saturation of the inverter resulted in undefined behavior and was avoided during further measurement.

Figure 3.38 shows the required source voltage of the inverter to follow a certain reference trajectory. Also indicated is the iso-line indicating the actual supply voltage of 24 V. Signals that would be represented above the iso-line represented in red would therefore cause saturation of the inverter.

Within the saturation limit the machine thrust is measured for various current signals, the result of which is depicted in figure 3.39. As expected, the thrust increases both with the amplitude and frequency of the excitation signal. At higher frequencies, that cannot be reached here without saturation of the inverter, one would start to see a drop as described earlier in the machine model.

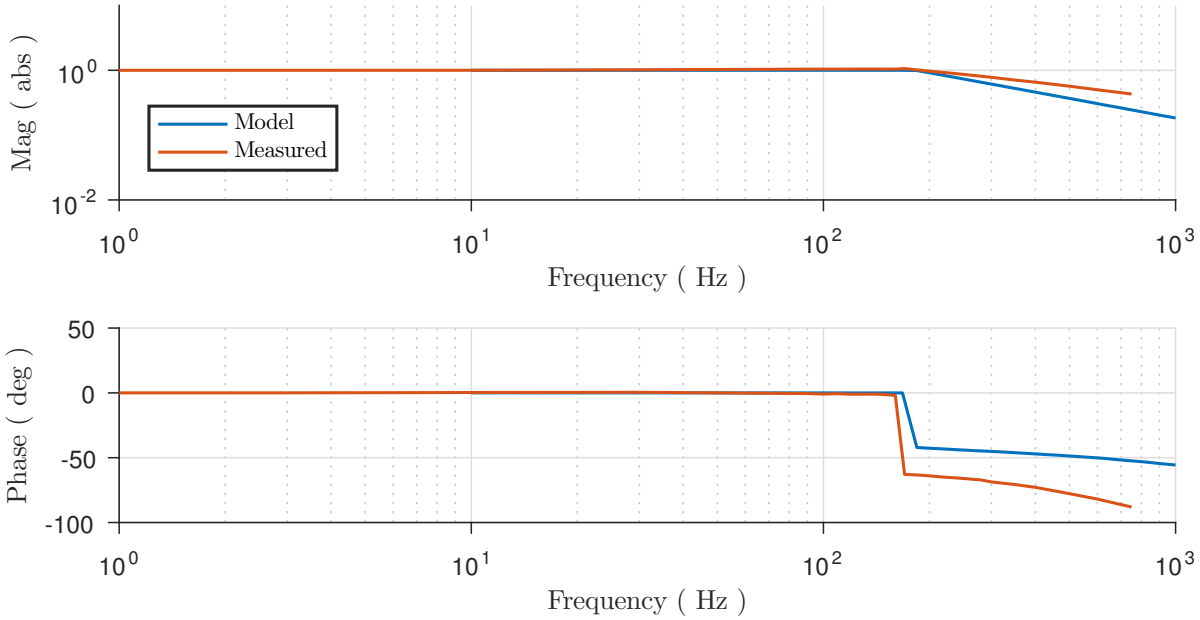

Figure 3.37: Frequency response for a three phase current vector, $i_s^* = 0.5\,\text{A}$. The magnitude given is the actual stator current versus the reference stator current, $\frac{i_s}{i_s^*}$

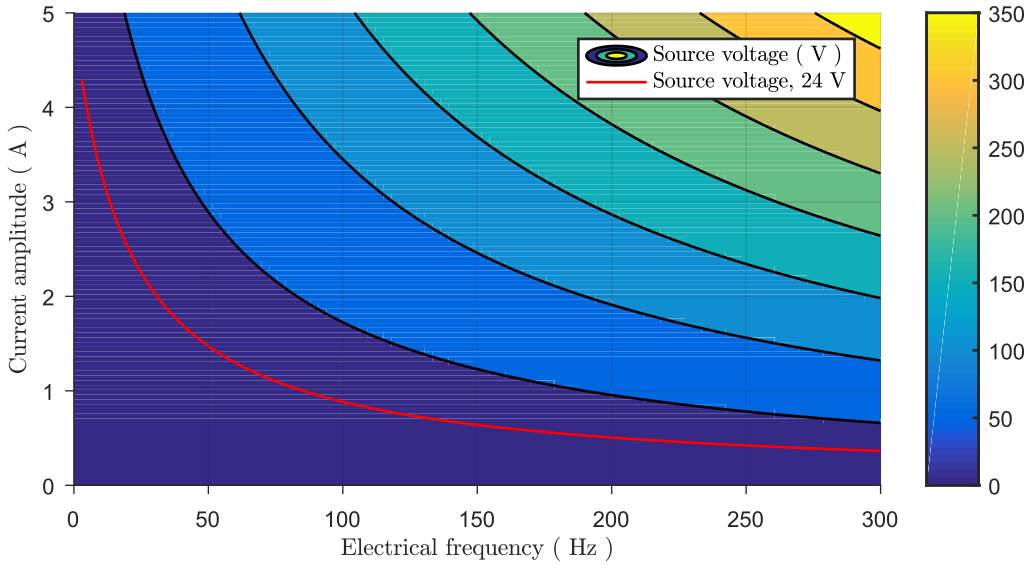

Figure 3.38: Necessary inverter source voltage with respect input signal. Visible is the current vector that can be produced by the inverter without saturating. The physical system is indicated by the red iso-line and can thus describe all reference signals South West of the line

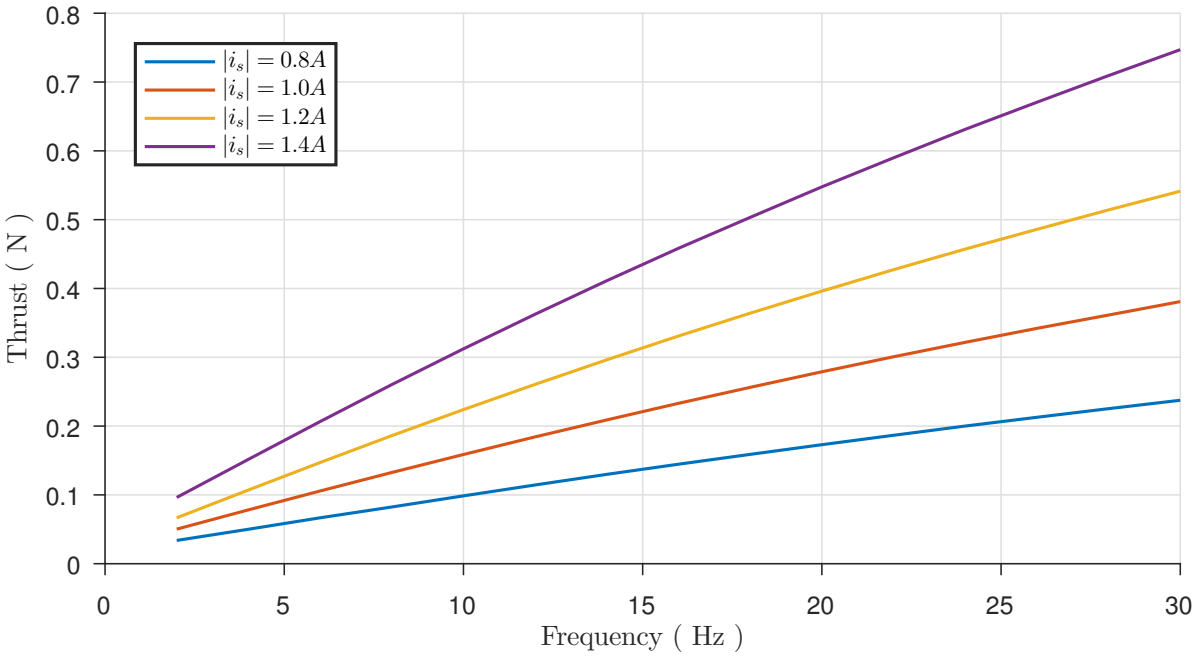

Figure 3.39: Measured force for various stator currents and frequencies

3.3.4. Thrust controller

The concept of FOC allows for direct control of the motors thrust. As shown in (2.4) for a certain flux (computed in (2.48)) the thrust is linearly proportional to the rotor current. In the dq-frame the rotor current is directly proportional to the quadrature current component and thus so is the thrust. The thrust controller can therefore be developed using the three phase current controller developed in the previous section. By aligning the angle of the transformation with the motor flux axis, instead of using a feed-forward electrical frequency, the decoupling of the stator current into the flux producing component (i_d) and the thrust producing current component (i_q), will be achieved.

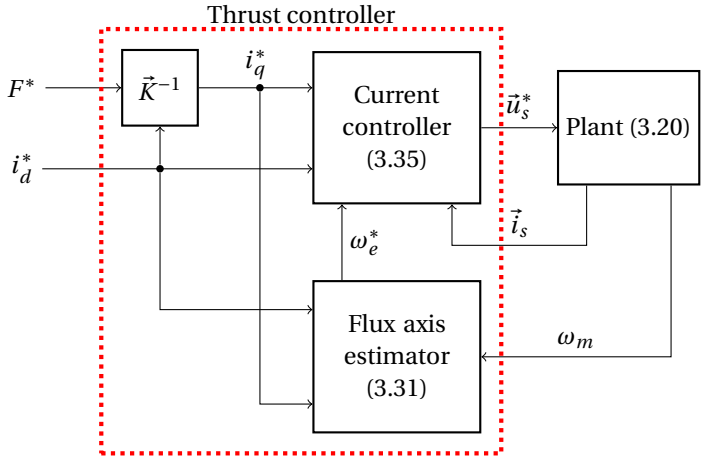

Figure 3.40: Thrust control scheme

One can see that transformation of the space vectors to the dq-frame allows for separate control of both components. Here the direct component is usually kept constant (equal to zero for permanent magnet motors) and the quadrature component reference is proportional to the desired thrust/torque. Apart from the inverse motor constant ($K^{-1}(i_d)$) the only difference with figure 3.35 is the alignment of the i_d current component with the magnetic flux axis.

Essential to a proper decoupling of the two current components and thus thrust control is the estimation of the magnetic flux axis. This is done using the earlier described estimator (figure 3.31). One can see that

the estimated slip frequency (ω_s) is computed using the ratio between the two current components times a certain constant value from the machine model ($\frac{R_R}{L_M}$).

The thrust curves measured earlier, using the less easily saturated analog amplifiers, are decoupled using (3.52) for a certain i_d. One can then compute the necessary ratio $\frac{R_R}{L_M}$ needed to describe the excitation frequency by the flux estimator (assuming $\omega_s = \omega_e$ for the static data) (3.53).

$$i_q = \sqrt{i_s^2 - i_d^2} \tag{3.52}$$

$$\frac{R_R}{L_M} = \frac{\omega_s \cdot i_q}{i_d} \tag{3.53}$$

The result of transforming these thrust curves are depicted in figure 3.41a. The lines depicted should be fully vertical for a correctly modeled estimator, assuming all assumptions made to derive the FOC scheme are valid. From this is seen that for $\frac{R_R}{L_M} \approx 45$ a fairly linear result is obtained, although in the low thrust region the estimator starts to underestimate slip velocity.

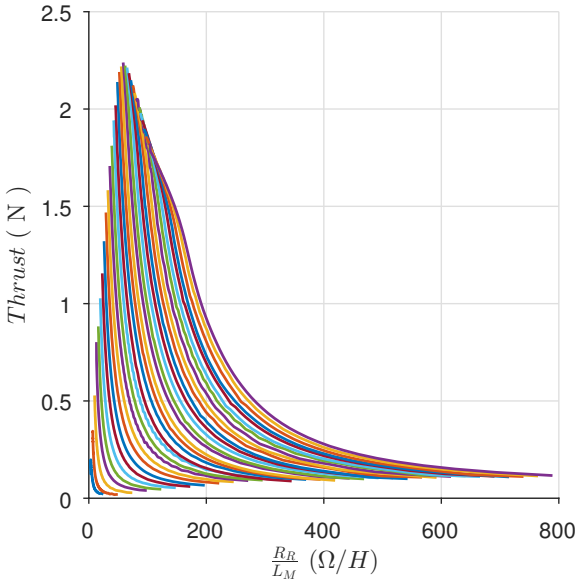

(a) Thrust with respect to estimator parameters, $i_d = 0.5\,\text{A}$

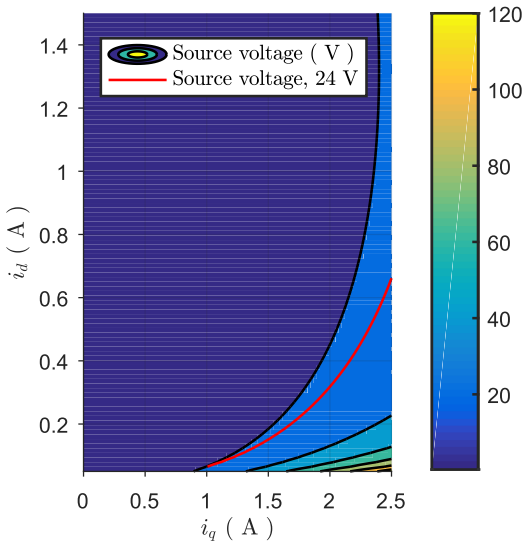

(b) Necessary inverter source voltage with respect to the dq input signal

Figure 3.41: Investigation of the parameters of the flux angle estimator and the resulting inverter saturation given in dq components

Given the machine and estimator parameters one can now also compute the source voltage required to follow a certain current reference in the dq-frame. Figure 3.41b indicates all the reference signals that can be tracked left of the red iso-line. Note the main source of saturation is due to the electrical frequency of the stator current and not the frequency of i_d itself.

Figure 3.43 shows the modeled closed loop frequency response of both current components using the current controllers described above. The reference signal is a constant i_d of 0.5 A and a frequency varying i_q component with an amplitude of 1.5 A.

Under the assumption that the estimate of the flux angle ($\hat{\theta}$) is accurate, this frequency response is accurate also for the thrust response. Figure 3.44 shows that for a certain constant i_d the produced thrust experiences a sinusoidal disturbance around its linear DC-thrust. In the modeling section this harmonic was predicted at double the electrical frequency.

Looking at the time average signal of the controlled thrust in figure 3.45 one can see the thrust is not fully linear with regard to i_q. At the low end of the thrust curve this is caused by an underestimation of the slip frequency by the linear slip estimator. On the high side of the thrust curves, the inverter saturates too early to give a proper verification of the linearity. It seems however that thrust approaches a linear domain before being saturated as was expected from figure 3.41a.

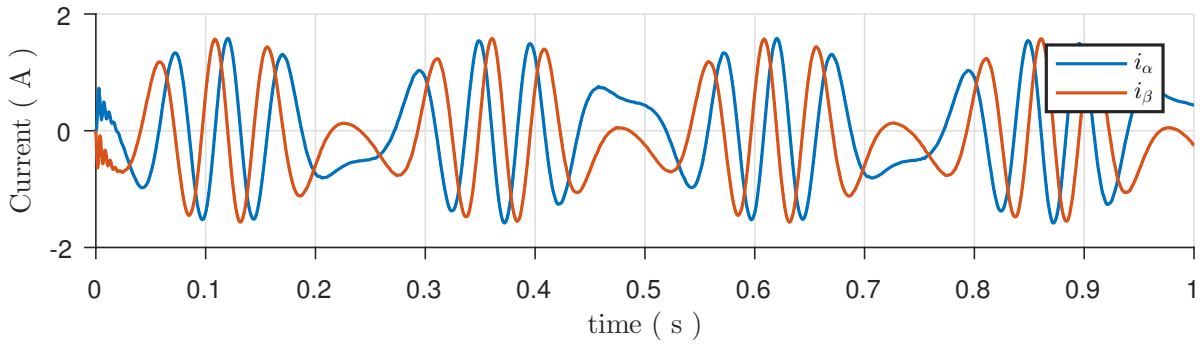

(a) Current components in $\alpha\beta$ reference frame

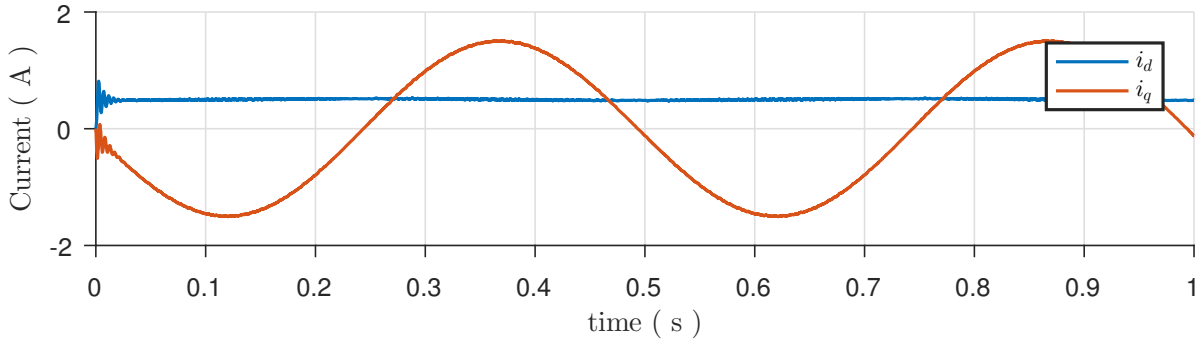

(b) Current components in dq reference frame

Figure 3.42: Time domain signals under reference of: $i_d = 0.5\,\text{A}$ and $i_q = 1.5 \cdot \sin(4\pi)$

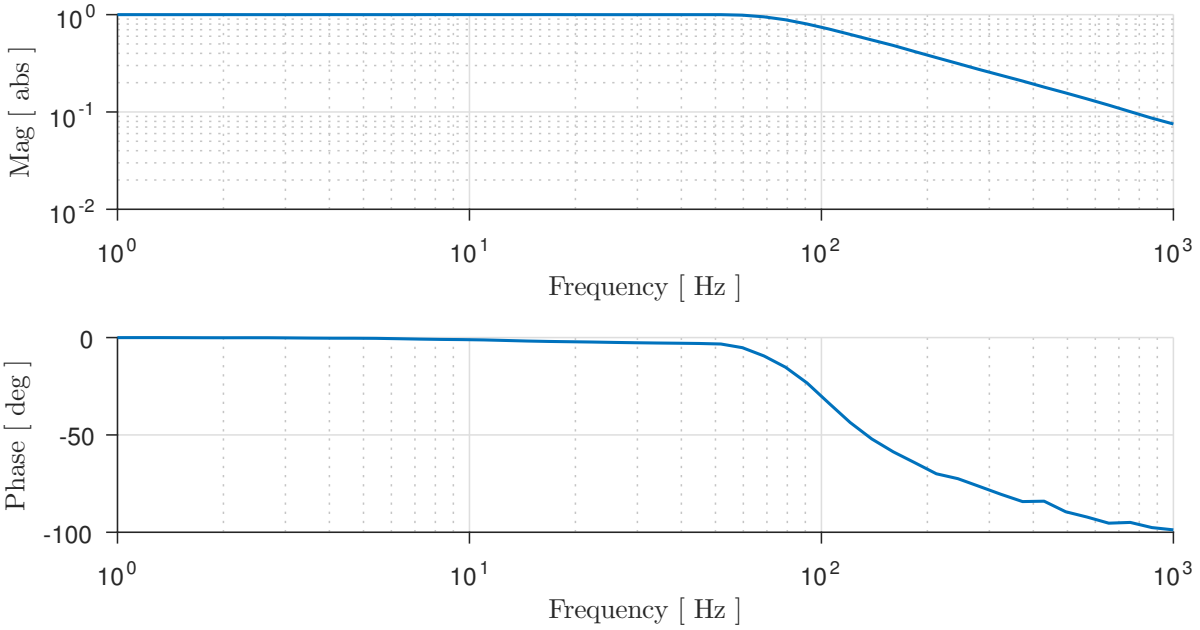

Figure 3.43: Modeled frequency response of dq current components, $i_d = 0.5\,\text{A}$ and i_q frequency dependent with amplitude 1.5 A. The magnitude given is the actual quadrature current versus the reference quadrature current, $\frac{i_q}{i_q^*}$. The direct current component is considered constant and thus the frequency response should be equal to that of the predicted thrust

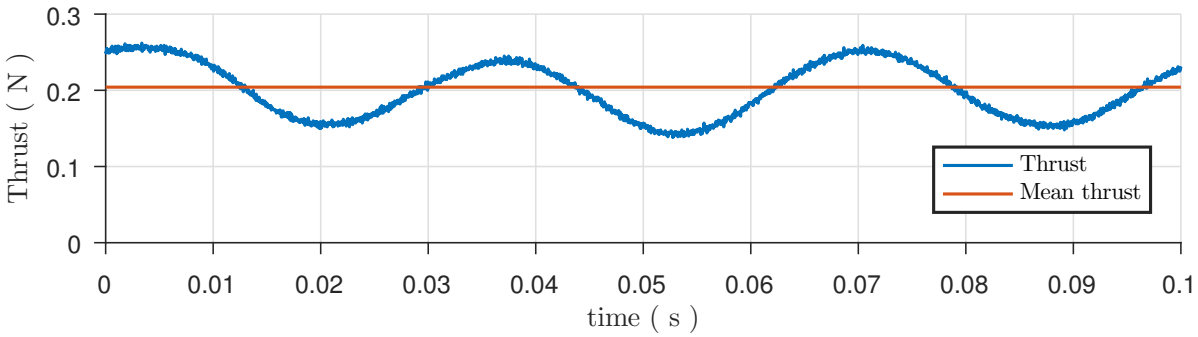

Figure 3.44: Harmonic thrust response, $i_d = 0.5$A, $i_q = 1.0$A

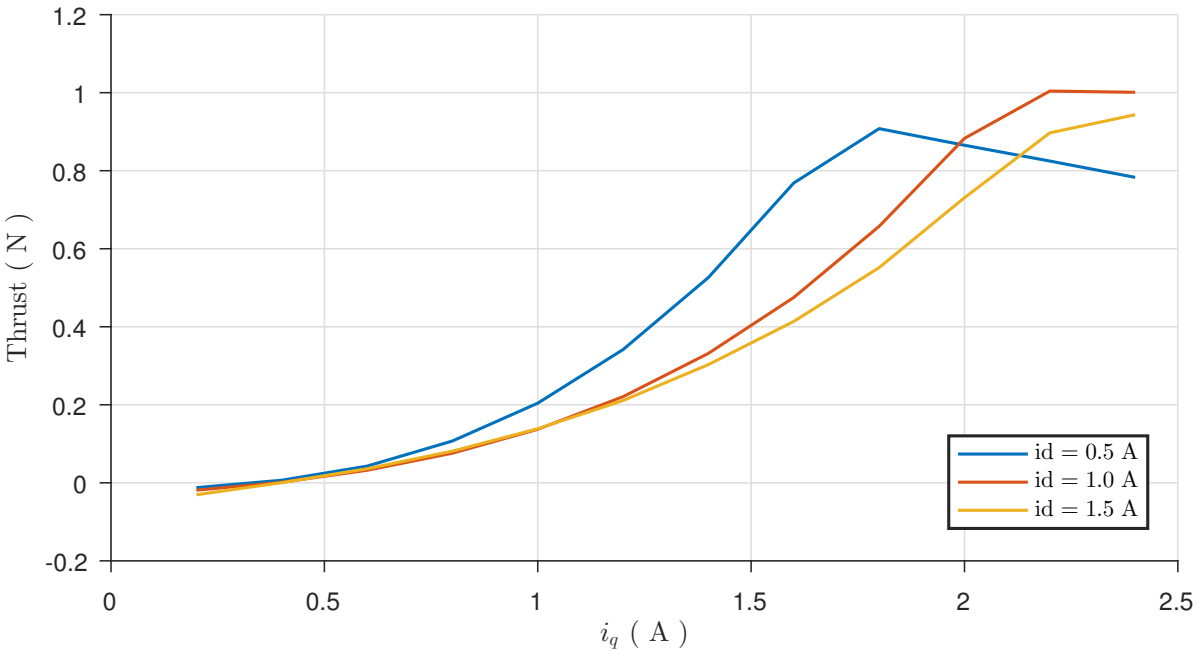

Figure 3.45: Time average thrust with respect to i_q

A very crude approximation is made of the motor constant for an i_d of 0.5 A at a value of $K(i_d = 0.5\,\text{A}) \approx 0.6\,\text{N/A}$. Allowing for implementation of the FOC thrust controller as described above. Note that within the saturation limits of the inverter thrust is more linear with the electrical frequency than with i_d.

3.3.5. Position control

Finally one can add a cascaded position controller around the thrust controller to achieve accurate positioning control. This results in the full scheme that is shown in figure 3.46.

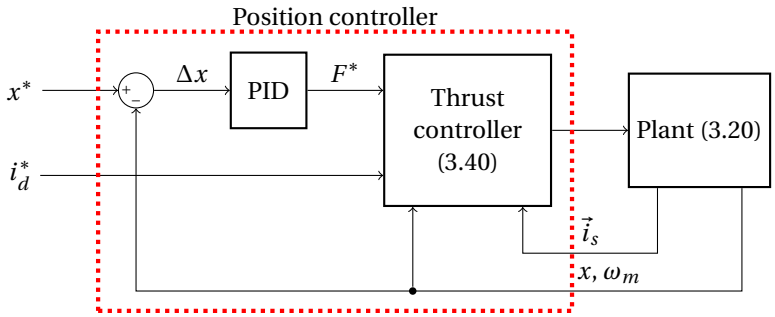

Figure 3.46: Position control scheme

The resulting control is implemented for the dynamic setup. Although the actuator produces a thrust all degrees of freedom except for the in plane rotation are constraint. Therefore the thrust will result in an angular acceleration according to (2.2).

$$\hat{T}(t) = r_0 \cdot F(t) \tag{3.54}$$

The equitation above describes the virtual torque produced by the LIM on the rotor. Here r_0 is the effective arm around the rotors center of rotation. Using (3.54) and the earlier described motor constant, one can now define the transfer function from i_q^* to the mechanical rotor angle (θ_m) as (3.55).

$$H_2(s) = \frac{\theta_m(s)}{i_q(s)} = \frac{K(i_d) \cdot r_0}{I \cdot s^2} \tag{3.55}$$

Using the earlier fitted transfer function of the dq-current components ($H_1(s)$) one can define the open loop response of the positioning system as the product of the two transfer functions that is dominated by the mass-line in the absence of physical stiffness.

$$P(s) = H_1(s) \cdot H_2(s) \tag{3.56}$$

Using the rules of thumb described in [36] the PID controller can be tuned. Due to the coarse resolution of the angle encoder the differential action of the PID controller was omitted. The used PI controller has the shape of (3.57).

$$i_q^* = \left(K_p + \frac{K_i}{s}\right) \cdot \Delta\theta_m \tag{3.57}$$

The system found to be stable for controllers tuned up to a bandwidth of 9.5 Hz. For which the controlled behavior is verified using a set of step responses of the rotor over an angel of 11.25° (or effective translation of 20.09 mm). Figure 3.47 shows various step response obtained by the controller.

The highly repeatable measurements shown in figure 3.47 were averaged to obtain figure 3.48. Here one can see resulting step has an overshoot of 37 % and a peak time (T_p) of 0.355 s. From the earlier description one can see that for a maximum settling time of 0.65 s measurements settle to under one encoder tick (0.35°) of the reference signal.

Using the measurement from the step response given above, one can make an estimate of the control bandwidth using (3.59). The resulting bandwidth is 1.49 Hz.

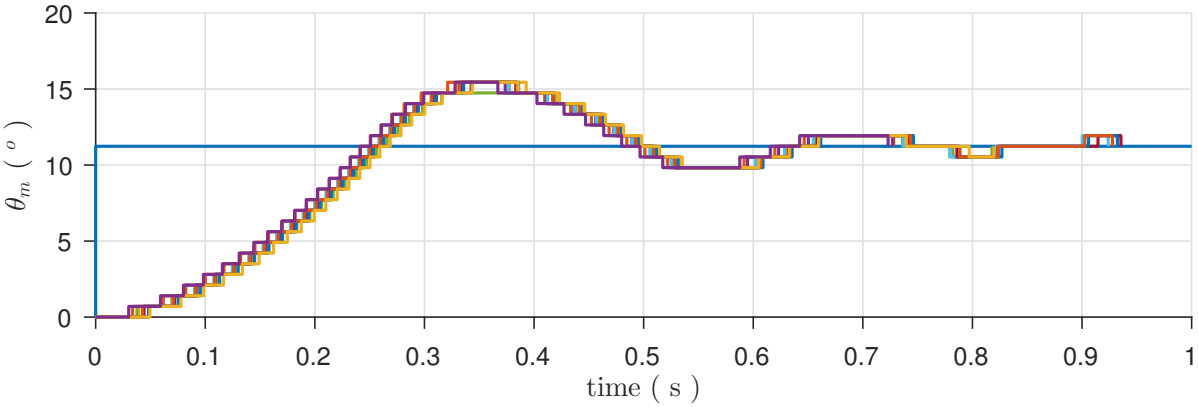

Figure 3.47: Position controlled step responses. One can see the various performed steps have a high repeatability

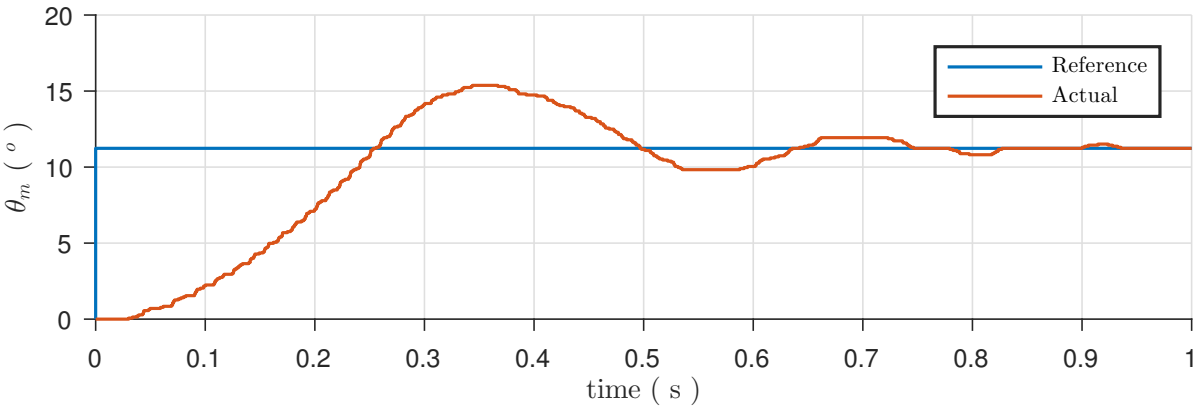

Figure 3.48: Mean position controlled step response

$$\zeta = \frac{-ln(0.37)}{\sqrt{\pi^2 + ln(0.37)}} = 0.33 \tag{3.58}$$

$$\omega_{bw} = \frac{\pi}{T_p\sqrt{1-\zeta^2}} = 9.34\,\mathrm{rad/s} \tag{3.59}$$

The verified bandwidth is lower than that the controller was tuned for, keep in mind the tuning of the controller to the frequency response is only valid for infinitely small amplitudes. As the amplitude of the described steps used for verification were large (as to measure it with sufficient resolution), the saturation of the controller output will naturally increase the peak time upon which the bandwidth was determined.

Finally also the position stability of the controller over time was verified. Measurements show that even the resulting position stability can be kept to ±1 encoder tick. This is equal to a position repeatability and stability of 0.35°3σ.

4

Planar stage design synthesis

The developed linear induction machine was developed for use in 3DOF planar positioning. One of the inherent benefits of linear induction machines is that the principle of generating thrust is independent of the rotor position. This means that the developed actuator has no motor cogging. An even bigger advantage making it ideal for planar positioning is that one can combine multiple LIM's to actuate the same rotor.

Below a theoretical planar stage design using linear induction machines as form of actuation will be covered. A description of the stage requirements, kinematics and control is given.

4.1. Requirements

The design of a planar stage is done for the application of a wafer handler that should be able to perform positioning adequate for inspection of the silicon wafer using microscopy. According to the American high-technology company BBN, the requirements for a laboratory one could expect such a positioning system to be build should comply with the Vibration Criterion A. Stating that the worst-case floor vibrations one can expect in the planar directions is $32\,\mathrm{mm/s^2}$ at a frequency of 10 Hz [1].

For a total moving mass of 1.6 kg (300 grams wafer and 1.1 kg rotor) one can determine the maximal disturbance force that can be expected given by (4.1), here a_d gives the acceleration of the disturbance. Furthermore one can determine that to overcome disturbances as specified by Vibration Criteria A of an amplitude of 10 µm (ϵ) one should have closed loop control stiffness of at least 5.9 kN/m, given by (4.2). Equal to a control bandwidth (ω_{cl}) of 9.7 Hz.

$$F_d = a_d \cdot m = 0.059\,\mathrm{N} \tag{4.1}$$

$$K_d = \frac{F_d}{\epsilon} = 5.9\,\mathrm{kN/m} \tag{4.2}$$

$$\omega_d = \sqrt{\frac{K_d}{m}} = 9.7\,\mathrm{Hz} \tag{4.3}$$

Additional requirements are gathered from the desired throughput of the machine. For this the assumption is made that the maximum dies that are made on a silicon wafer have the dimension of 20 mm × 20 mm. The stage will be required to be able to make the 20 mm steps between dies with a 2 % settling time ($T_{0.02}$) of no more than 1.5 s. Assuming the same damping ration measured in the experimental setup one can compute the maximum force necessary.

$$\omega_{cl} = -\frac{\ln\left(0.02 \cdot \sqrt{1-\zeta^2}\right)}{\zeta \cdot T_{0.02}} = 1.3\,\mathrm{Hz} \tag{4.4}$$

$$F_{\mathrm{step}} = \omega_{\mathrm{step}}^2 \cdot m \cdot \Delta x = 2.1\,\mathrm{N} \tag{4.5}$$

4.2. Stage design

The conceptual stage design combines a set of three previously design linear induction machines spaced respectively 120° from one another along a circle with a diameter of (r_0). Figure 4.1 shows the placement of the three actuators with respect to the stage origin.

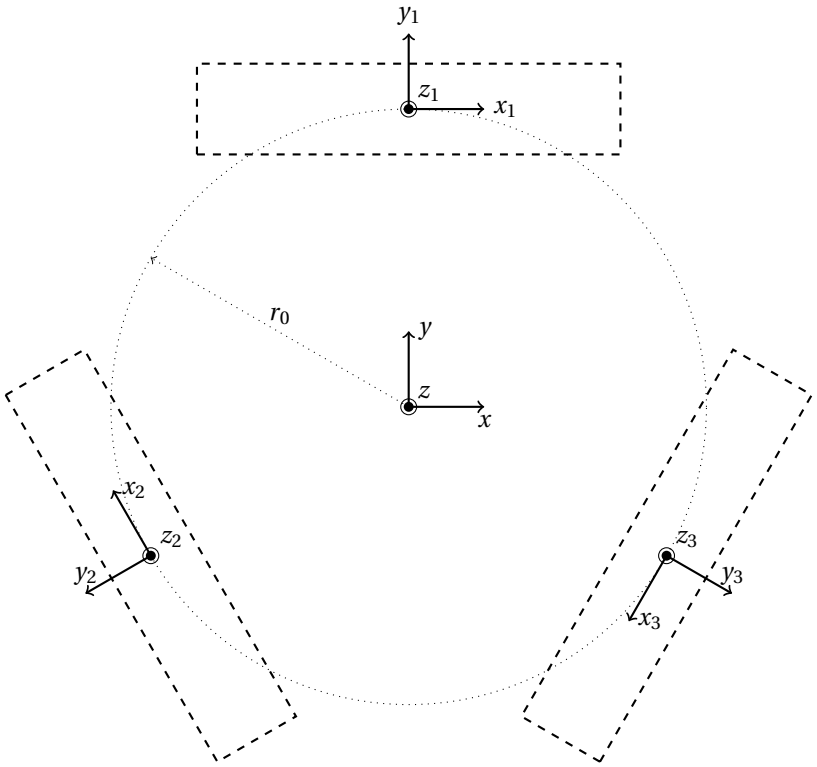

Figure 4.1: Planar arrangement of linear induction machines in a planar stage

The spaced LIM's combined allow for actuation of all three planar degrees of freedom, xy translation and rotation around the z-axis. In combination with, for instance, a planar air bearing arrangement the three DOF range limited only by the rotor dimensions and sensing options.

Due to the transverse field that exists around the linear actuators can be considered negligible after about 40 % of the pole-pitch on either side of the machine. To keep the machines as predictable as possible a distance of 0.4τ should therefore be considered both the minimal rotor overhang and for spacing of the machines to one another.

4.3. Kinematic decoupling

From figure 4.1 one can see the linear machines need to be controlled in a cooperative manner to control the three planar Cartesian degrees of freedom. Below one can see the three thrust vectors of the respective machines (F_{x1}, F_{x12} and F_{x2}) and the three normal forces (F_{z1}, F_{z12} and F_{z2}) described in the global reference frame. Here $\vec{F}_p$ represents forces/moments of the in plane DOF and $\vec{F}_o$ of the out of plane DOF.

$$\vec{F}_p = \begin{bmatrix} F_x \\ F_y \\ T_z \end{bmatrix} = \begin{bmatrix} 1 & -\frac{1}{2} & -\frac{1}{2} \\ 0 & \frac{\sqrt{3}}{2} & -\frac{\sqrt{3}}{2} \\ -r_0 & -r_0 & -r_0 \end{bmatrix} \cdot \begin{bmatrix} F_{x1} \\ F_{x2} \\ F_{x3} \end{bmatrix} = \vec{M}_p \cdot \begin{bmatrix} F_{x1} \\ F_{x2} \\ F_{x3} \end{bmatrix} \tag{4.6}$$

$$\vec{F}_o = \begin{bmatrix} F_z \\ T_x \\ T_y \end{bmatrix} = \begin{bmatrix} 1 & 1 & 1 \\ r_0 & -\frac{r_o}{2} & -\frac{r_0}{2} \\ 0 & \frac{r_0 \cdot \sqrt{3}}{2} & -\frac{r_0 \cdot \sqrt{3}}{2} \end{bmatrix} \cdot \begin{bmatrix} F_{z1} \\ F_{z2} \\ F_{z3} \end{bmatrix} = \vec{M}_o \cdot \begin{bmatrix} F_{z1} \\ F_{z2} \\ F_{z3} \end{bmatrix} \tag{4.7}$$

Note that the thrust vectors of the respective linear machines can be combined to develop all planar thrust vectors. The two planar Cartesian translations F_x and F_y have a respective maximum magnitude that is 2 and

$\sqrt{3}$ times the thrust of a single linear machine. Furthermore the developed torque T_z scales with $3 \cdot r_0$ the actuator thrust and is thus linear dependent with the pitch radius of the actuators. Using the previously obtained thrust using the developed actuator of 1.75 N this would amount to a $F_x = 3.50\,\text{N}$ and $F_y = 3.03\,\text{N}$. And thus is well within the requirements of disturbance rejection and settling-time. Although the bandwidth needed for disturbance rejection will require further verification.

$$\begin{bmatrix} F_{x1} \\ F_{x2} \\ F_{x3} \end{bmatrix} = \begin{bmatrix} \frac{1}{2} & 0 & -\frac{1}{3 \cdot r_0} \\ -1 & \frac{1}{\sqrt{3}} & -\frac{1}{3 \cdot r_0} \\ -1 & -\frac{1}{\sqrt{3}} & -\frac{1}{3 \cdot r_0} \end{bmatrix} \cdot \begin{bmatrix} F_x \\ F_y \\ T_z \end{bmatrix} = \vec{M}_p^{-1} \cdot \vec{F}_p \tag{4.8}$$

$$\begin{bmatrix} F_{z1} \\ F_{z2} \\ F_{z3} \end{bmatrix} = \begin{bmatrix} \frac{1}{3} & \frac{1}{2 \cdot r_0} & 0 \\ \frac{1}{3} & -\frac{1}{4 \cdot r_0} & \frac{1}{r_0\sqrt{3}} \\ \frac{1}{3} & -\frac{1}{4 \cdot r_0} & -\frac{1}{r_0\sqrt{3}} \end{bmatrix} \cdot \begin{bmatrix} F_z \\ T_x \\ T_y \end{bmatrix} = \vec{M}_o^{-1} \cdot \vec{F}_o \tag{4.9}$$

The inverse kinematics will be used to transform the control effort from the global reference frame to the local machine coordinates.

4.4. Planar control

Planar control of the rotor is achieved using a strategy very similar to the control strategy discussed in section 3.3.5. Here the position control is applied in the global coordinate system after which the computed control effort in the global reference frame is transformed to the local reference frame of the three actuators. It is in this local reference frame that the FOC thrust controllers (figure 3.40) control their respective linear machine.

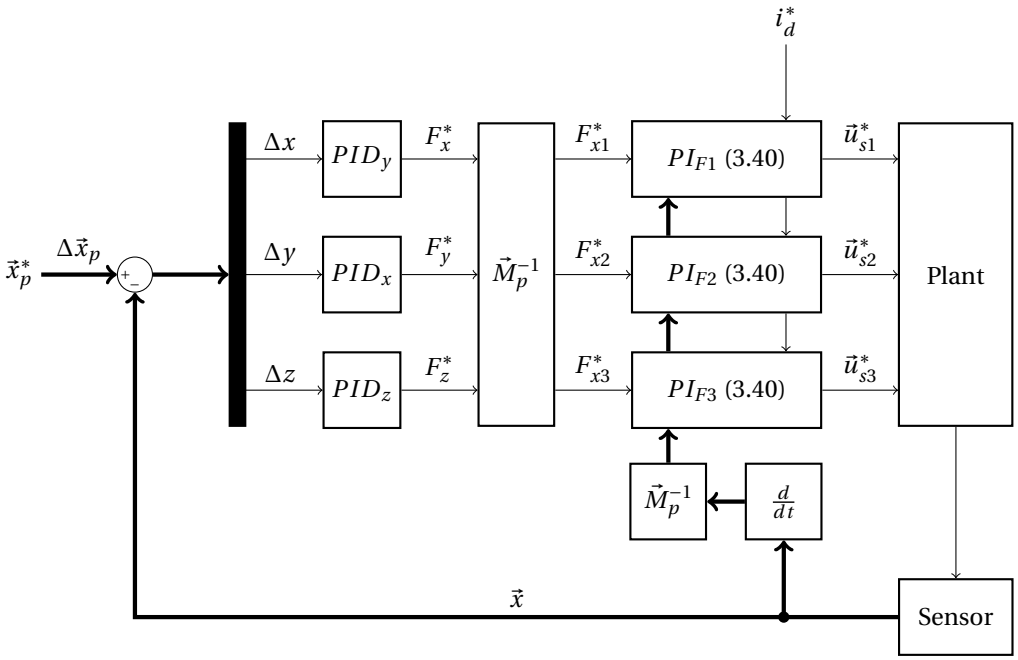

Figure 4.2: Planar position controller scheme, thick arrows represent 3 DOF signals

In figure 4.2 an overview is given of the complete control scheme. Note that the sensing scheme is considered to be in the global reference system and expected to sense all three DOF simultaneous. The same inverse transformation ($\vec{M}_p^{-1}$) can be used on the measured velocities as on the forces to allow for transformation to the local machine coordinates.

Further extension of the scheme in figure 4.2 is possible by controlling both the in and out of plane DOF. Although the range of the out of plane DOF will be limited by the bearing system, one could actively constrain them.

5
Conclusion

Concluding the thesis results will be covered below. The various steps taken in the process with the outcome will be covered. Followed by a discussion on some of the choices made during the research. Finally recommendations for future research will be noted, based on the research as covered in this thesis.

5.1. General conclusion

The main goal of this research was a study of the feasibility of the use of linear induction machines as direct drive actuation method for planar positioning. The main conclusion is that it is indeed very well possible to use linear induction machines for planar positioning.

5.1.1. Machine theory

After an initial description of the physical principles on which linear induction machines are based a description is given on the current state of the art. The trend in research moving away from analytical modeling towards the more detailed FEA models is described together with the renewed interest in linear induction machines for planar actuation.

The machine theory from literature is covered in a 1D analytical model that is compared to 2D numerical models made using FEA. The two models describe a close resemblance for an infinitely long machine. The analytical model is furthermore found to give a thorough understanding of the longitudinal end-effects that occur within a linear induction machine. For an exact prediction of the magnitude of the end effects at low speeds the numerical model is best used.

Verification of the machine behavior and the numerical model using empirical data show an accurate description of machine performance. The transverse effects are however found to be slightly more sensitive to the air-gap than predicted by the FEA model.

Finally the machine is modeled using a lumped parameter model of which the parameters have been fitted to empirical measurements of the physical machine.

5.1.2. Actuator design and implementation

Based on the analytical and numerical model a sensitivity analysis of the design variables of a linear induction machine is performed. Based on the performed analysis a collinear design approach is defined for the development of a LIM optimized for thrust within the constraints of the current supply.

The design approach is then applied to develop the detailed design for a linear induction machine. For which both the mechanical and electronic design are covered in detail. Although some trade-offs with regard to manufacturability have been made a fully working LIM was developed. The machine is found to indeed deliver the designed thrust of 1.75 N under feed-forward current excitation.

The implementation of a cascaded field oriented control scheme is discussed together with the strategies used for real-time implementation on the embedded hardware. The developed current controller is found to have a bandwidth of up to 175 Hz for a current amplitude of 0.5 A. Further development of the cascaded position controller has a verified positioning bandwidth of 1.5 Hz with a repeatability and precision currently limited by the position sensor to within one encoder tick ($\pm 0.35°$).

5.1.3. Planar stage synthesis

Finally the approach to implementing the designed actuator into a planar stage is discussed. Here the considerations that have to be made with respect to the requirements, kinematics and control are discussed.

The developed actuator is found to be applicable to the development of a planar microscopy stage. The kinematics reveal a worst case thrust component of the axisymmetric stage design that is $\sqrt{3}$ times the thrust of a single LIM. Furthermore the available torque is linear proportional to the effective pitch radius of the actuators. The available thrust verifies the applied controllers are sufficient for microscopy inspection of a standard 300 mm wafer.

The kinematic decoupled control strategy proposed allows for decoupled control of the the Cartesian coordinates before transforming the control effort back to the machine coordinates of the FOC thrust controllers.

5.2. Discussion

Below some of the research topics that are covered in the thesis are further discussed. The topics covered, describe trade-offs made during the project and the hind-sight view of them.

5.2.1. Modeling of static longitudinal end-effects

The 1D analytical model used in the thesis gives a good insight in the longitudinal end-effects present in a linear induction machine. At low rotor velocities, as expected for planar positioning, the assumptions, made for the analytical boundary conditions, however hold poorly. Although 2D models have been described that can be solved for this state using a relaxation method there is room for discussion if such a model gives any additional insight over a FEA model opted for in this thesis.

5.2.2. Transverse effects

The effects present in the transverse direction are in this thesis taken into account in the respective 1D and 2D model using reduced effective rotor conductivity. As found in verifying the built machine the effect of the air-gap has proven slightly more severe than expected using the constant compensation for the transverse effects. Although the overall performance is still accurately predicted using the 2D model, one could opt to include the transverse effects in a full 3D model. The added computational cost here proved too much overhead for use in the sensitivity analysis.

5.2.3. Thrust harmonic

As seen in the modeling of the thrust behavior, the thrust is proportional to the product of two sinusoidal waves with a certain phase difference causing a thrust harmonic at a frequency twice the electrical frequency. In the thesis the thrust harmonic is accounted for as if it is a disturbance working on the rotor. The modeled effect could however also be accounted for using a feed-forward control term.

5.2.4. Direct versus indirect field oriented control

As covered in the thesis, there is a trade-off between the two control strategies. Where the direct method requires additional sensors the indirect control method relies on the correct estimation of the motor flux angle.

In this thesis the use of the indirect method is implemented as the electronic design is greatly simplified as well as the flux estimation in the current toothed stator. The added benefit of the direct flux measurement could however benefit the linearity of the thrust especially in the low thrust region.

5.3. Recommendations

As the use of linear induction machines has proven a feasible option for planar positioning several recommendations for further research are given below. Although this thesis has covered a lot of the groundwork necessary for research on linear induction machines within the Mechatronic System Design group, further research can always be performed.

5.3.1. Set-up improvements

The initial recommendation that has to be covered is a set of improvements that can be made to the experimental set-up for research purposes. The current set-up designed as a feasibility study was optimized for

thrust. I would suggest development of a research set-up that is optimized for predictability.

The design of toothless stator core that is several pole-pairs in length would result in a center region that is close to the well described continuous model. Furthermore use of a larger inverter to avoid saturation and a position sensor with a higher resolution would allow for more targeted research of specific characteristics.

5.3.2. Over actuation

As seen throughout the thesis the actuation of a linear induction machine is achieved using a 2 DOF current excitation. Described by its respective amplitude and frequency or the later introduced direct and quadrature components. The thesis however only covers a single variable (thrust) in its control strategy. For rotary machines a strategy developed by Texas Instruments called power warp investigates the use of a non-constant i_d component to minimize the copper losses in the stator under steady-state operation.

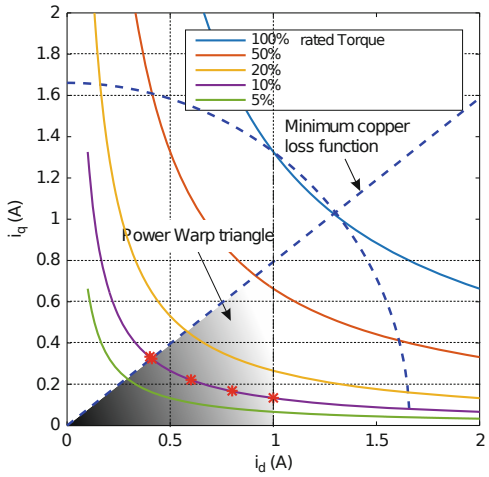

Figure 5.1: Visualization of TI's power warp strategy. Keeping i_d constant for a high dynamic response, the power warp strategy tries to follow the constant torque curve to the point of minimal copper losses while under steady-state operation [8]

It is proposed to look into the possibilities of similar, here called, over actuation strategies that would allow for a more advanced control of the linear induction machines. The most promising aspect of this with regard to planar actuation is for simultaneous actuation of both the thrust and the normal force of the linear induction machine. Achieving this would allow for an actively controlled planar bearing, by controlling the bearing pre-load.

5.3.3. Planar stage

A design synthesis is given of the implementation of a planar stage using linear induction machines, an actual 3 DOF set-up would allow investigation of the full capabilities of such a system.

Also this would allow for further investigation of the control methods used for planar control. The now proposed decoupled control could be improved upon using for instance a multi input multi output position controller.

A

Actuator/Set-up parameters

The tables below describe the parameters of the developed linear induction machine. The same parameters are used in the sensitivity analysis and most of the other figures found in the thesis. Also given are the parts used in the experimental set-up apart from the electronics separately discussed.

Table A.1: Design parameters of the designed linear induction machine

Parameter	Value	Unit	Description
τ	35	mm	Pole-pitch
p	2		Nr. of pole pairs
L	140	mm	Stator length
D	30	mm	Stator depth
n	300		Windings per coil
w	7.6	mm	Coil width
d_w	0.5	mm	Winding wire diameter
d_1	1.0	mm	Rotor conductor thickness
d_2	1.5	mm	Rotor backing thickness
d_3	15	mm	Stator core thickness
Static set-up			
g	2-4	mm	Effective air-gap (including d_1)
m	0.88	kg	Moving mass
Dynamic set-up			
g	2	mm	Effective air-gap (including d_1)
r_0	112.5	mm	Effective torque arm
I	0.050	kg/m^2	Angular inertia around axis of rotation

Table A.2: Components used in experimental set-ups

Component	Part	Description
Load-cell	Futek LSB200	Load-cell used for thrust measurement
Sensor amplifier	Scaime CPJ rail	Amplifier used for load-cell signal
Data acquisition	NI USB-6211	16 bit analog data acquisition thrust measurement
Angular encoder	Avago HEDS-9140	10 bit rotary encoder

B

Parameter estimation

To achieve a correct tuning of the controllers in the setup an accurate model of the actuator is necessary. Below a model will be fitted to empirical data. The parameters will be estimated for a per phase model often used with rotary induction motors: the five parameter model [8]. As the name suggests and can be seen in figure 2.28 a set of 5 parameters will have to be evaluated. Furthermore the slip (s) is defined as:

$$s = \frac{\omega_s - \omega_m}{\omega_s} \tag{B.1}$$

Static phase resistance

One can start with a simple DC measurement of the phase resistance. Doing this gives one the value for R_s. In the case of the motor this amounts to $R_s = 2.8\,\Omega$ per phase.

No load test

In a rotary machine the "no load" case is described as the state the machine is in with a slip close to 0. This means that the mechanical frequency (ω_m) of the machine as approximately the same as the electrical frequency (ω_s) of the machine. As can be seen in figure 2.28 this will cause $\frac{R_r}{s} \to \infty$ and thus the equivalent circuit for this state can be simplified to figure B.1a.

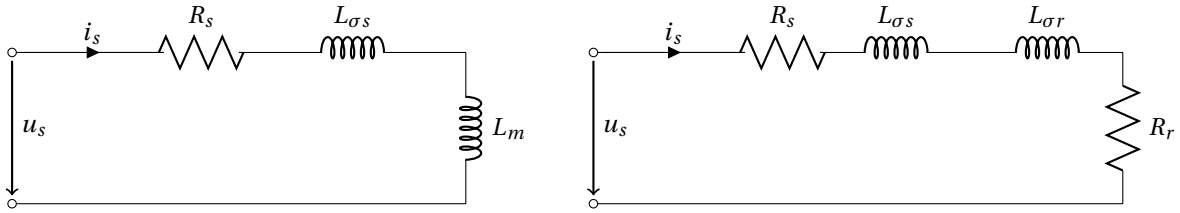

(a) No load circuit approximation

(b) Locked rotor circuit approximation

Figure B.1: Simplification of 5 parameter model under different experimental tests cases

To perform the "no load" test one normally lets the motor spin freely without any additional load attached. In the case of the static set-up this freedom of motion is not permitted. Therefore a second rotor was developed comprising of only the iron backing layer. This means the rotor has no conducting layer and thus $\frac{R_r}{s}$ indeed approaches infinity.

In figure B.2 one can see the results of the no load test performed. Here the magnitude is given by the stator current divided by the input voltage ($H_{nl} = \frac{I_s}{u_s}$). Also the bandwidth of the system is indicated with the dotted line at 25.95 Hz. The current system can be modeled by (B.2).

$$H_{nl}(j\omega) = \frac{1}{R_s + L \cdot j\omega} \tag{B.2}$$

$$H_{nl}(j\omega_{nl}) = \frac{H_{nl}(0)}{2} \tag{B.3}$$

Defining the bandwidth as the frequency at which the magnitude is crosses the -3 dB line results in the following motor values:

$$L_{nl} = L_{\sigma s} + L_m = \frac{R_s}{\omega_{nl}} = 17.2\,\text{mH} \tag{B.4}$$

The zero that can be seen in the measurements is due to a filter capacitance in the voltage measurement of the voltage supply.

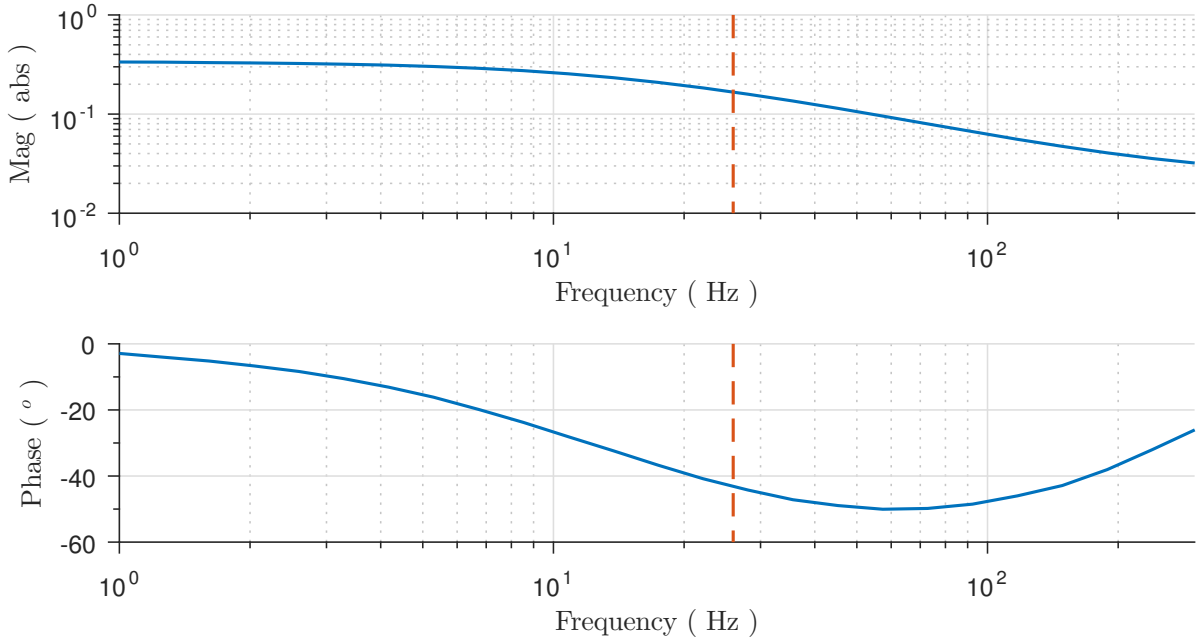

Figure B.2: No load measurement data

Locked rotor test

Performing a frequency analysis as done in the section above but for a locked rotor allows for the estimation of the final parameters. The rotor resitance is now characterized by the limit described in (B.5).

$$\lim_{s \to 1} \frac{R_s}{s} = R_s \tag{B.5}$$

Under the assumption that the rotor resistance is much smaller than the core resistance [22] one can simplify the equivalent circuit to figure B.1b. Figure B.3 indicates the measured behavior of the machine with the new bandwidth indicated at 25.30 Hz. Using (B.6) one can compute the rotor resistance and the locked rotor inductance as 18.57 mH.

$$R_r = R_{lr} - R_s = \frac{1}{H_{lr}(0)} - R_s = 0.15\,\Omega \tag{B.6}$$

$$L_{lr} = L_{\sigma s} + L_{\sigma r} = \frac{R_{lr}}{\omega_{lr}} = 18.57\,\text{mH} \tag{B.7}$$

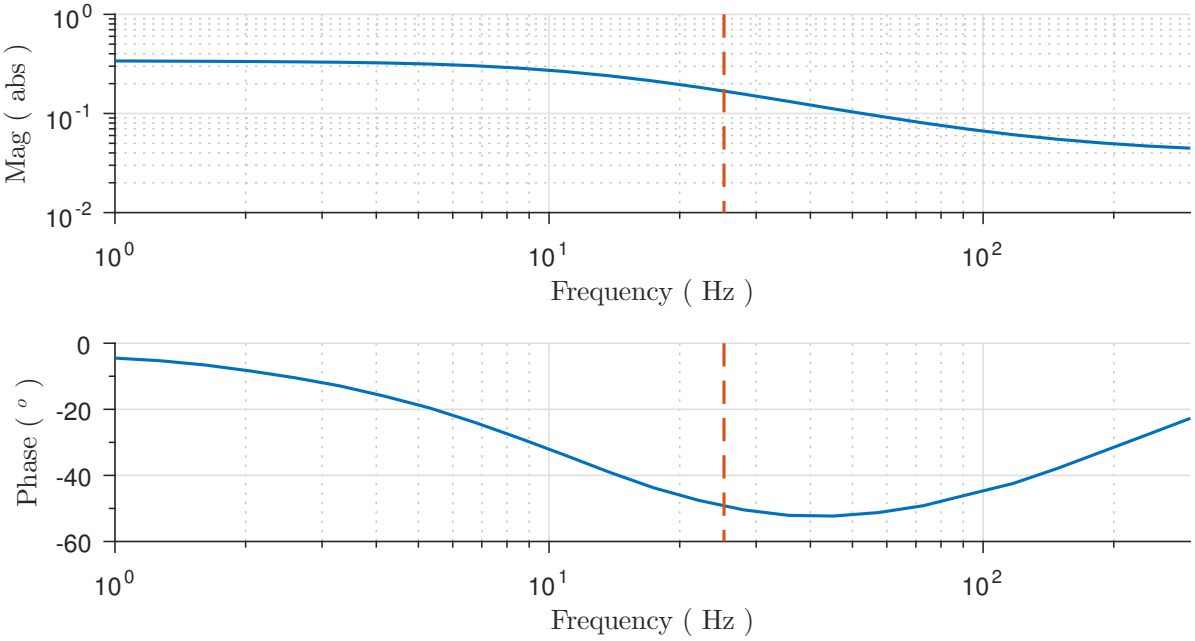

Figure B.3: Locked rotor measurement data

Parameter estimation

Under the assumption that the leakage inductance of the stator is approximately equal to the leakage inductance of the rotor (B.8) one can solve all the parameters of the equivalent circuit.

$$L_{\sigma s} = L_{\sigma s} = \frac{L_{lr}}{2} \tag{B.8}$$

Table B.1 describes the final parameters estimated for the equivalent circuit model. Take into account this is a steady-state model and no verification of the transient behavior is given. Also the equivalent parameters of the 4 parameter model are given.

Table B.1: Estimated motor parameters of the developed linear induction machine

(a) Equivalent circuit parameters of the 5 parameter model

Parameter	Value	Unit
R_s	2.8	Ω
R_r	0.15	Ω
$L_{\sigma s}$	9.29	mH
$L_{\sigma r}$	9.29	mH
L_m	7.91	mH

(b) Equivalent circuit parameters of the 4 parameter model

Parameter	Value	Unit
α	0.46	
L_σ	13.55	mH
L_M	3.64	mH
R_R	0.032	Ω

C

Amplifier verification

Initial measurements were performed using a set of three linear amplifiers designed by Paul Ouwehand [31]. Figure C.1a shows the main design of the amplifier.

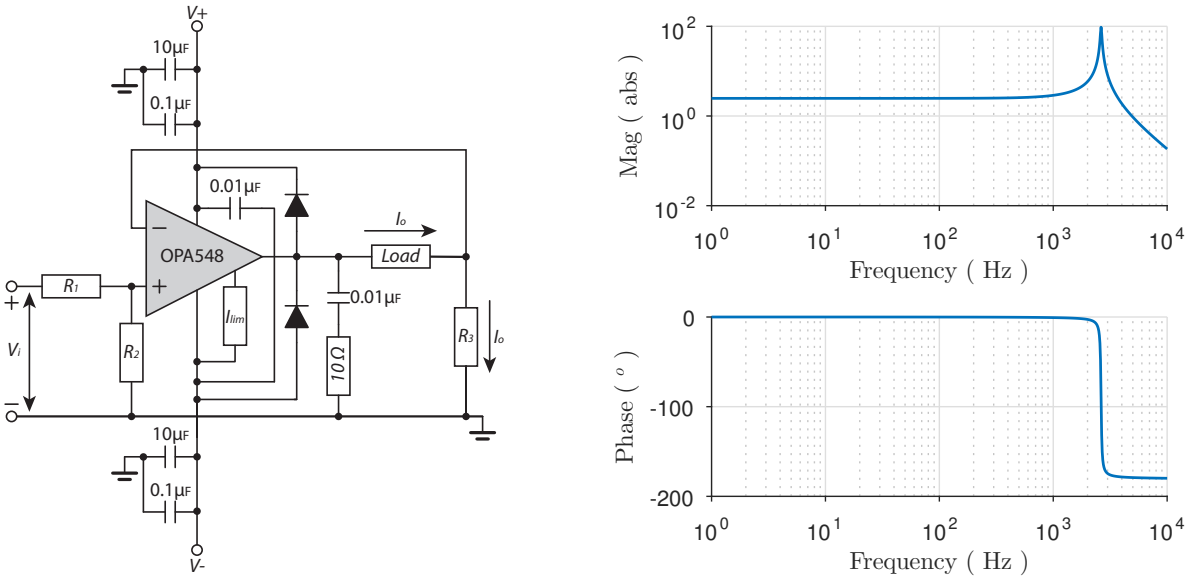

(a) Detailed amplifier design

(b) Main amplifier design

Figure C.1: Linear amplifier schematics and behaviour

Confirming the desired behavior of the amplifier is done using LTspice. From this one can confirm that for the specified L-R load of the actuator phases the amplifier has a bandwidth of about 2.75 kHz what is more than sufficient.

After testing the amplifier behavior however seemed to be heavily deteriorated by the self inductance of the load. The behavior seen in figure C.1b is valid only for small amplitudes and does not take into account the amplifier saturation. As can be seen below in figure C.2 the signal tracking accuracy of the amplifier is deteriorated far below the amplifier bandwidth.

Amplifier saturation occurs once the voltage required to match the reference is higher than that of the power supply. For this specific system the system is powered with: $V = \pm 24\,\mathrm{V}$. One can describe the required source voltage by the (C.1) for an L-R load.

$$u_{DC} = 2 \cdot I\,(R + \omega_e \cdot L) \tag{C.1}$$

One can now determine the reference signals that the amplifier can follow without saturating. Figure

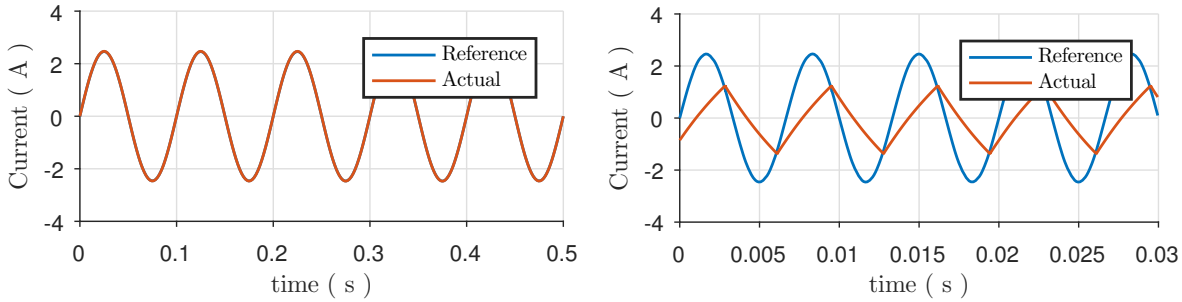

(a) Amplifier behaviour, 2.5 Hz at 10Hz

(b) Amplifier behaviour, 2.5 Hz at 150Hz

Figure C.2: Amplifier reference tracking for various frequencies

shows the working range of the amplifier together with the required minimal source voltage required. Everything underneath the red contour line indicating a source voltage of ±24V.

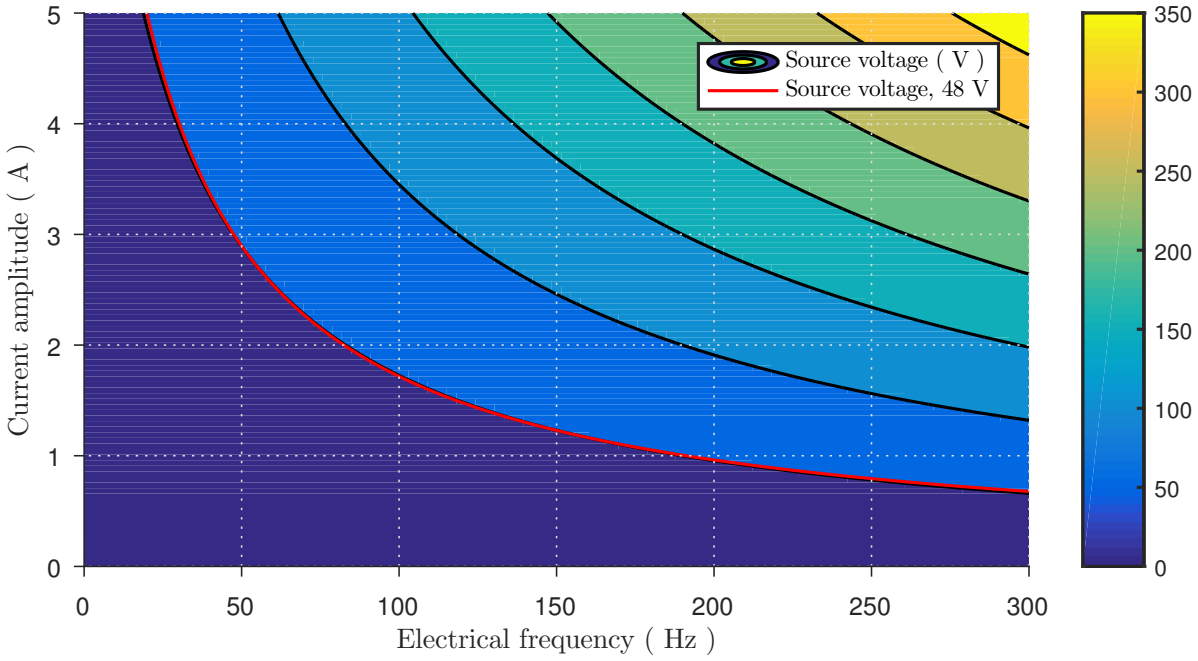

Figure C.3: Minimal power supply voltage

D

Load-cell verification

In the static set-up use is made of a Futek LSB200 load-cell to measure the produced thrust. And although the load-cell has a good linearity (0.1 % of the range) some sensor noise is measured for static measurements. In figure D.1 shows the spread of the measured signal with a standard deviation of $\sigma = 5.65 \times 10^{-4}$ N.

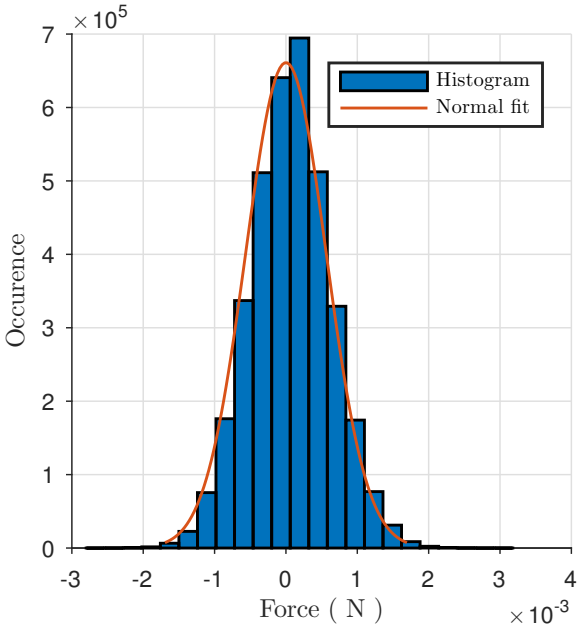

Figure D.1: Signal

Furthermore during measurement of the thrust characteristics as described in section 3.1.4 a disturbance was measured at about 30 and 60 Hz. Using the stiffness of the load-cell in combination with the moving mass leads to believe that it might be due to the eigenfrequence of the system.

To verify the assumption the response is measured for a system excited by a small impact excitation. As seen in figure D.2a the time response matches that of a mass-spring-damper system. A frequency analysis of the response confirms the eigenfrequency lies at 60 Hz. The measured disturbance is thus assumed to be due to the thrust harmonic excitation of the systems eigenfrequency.

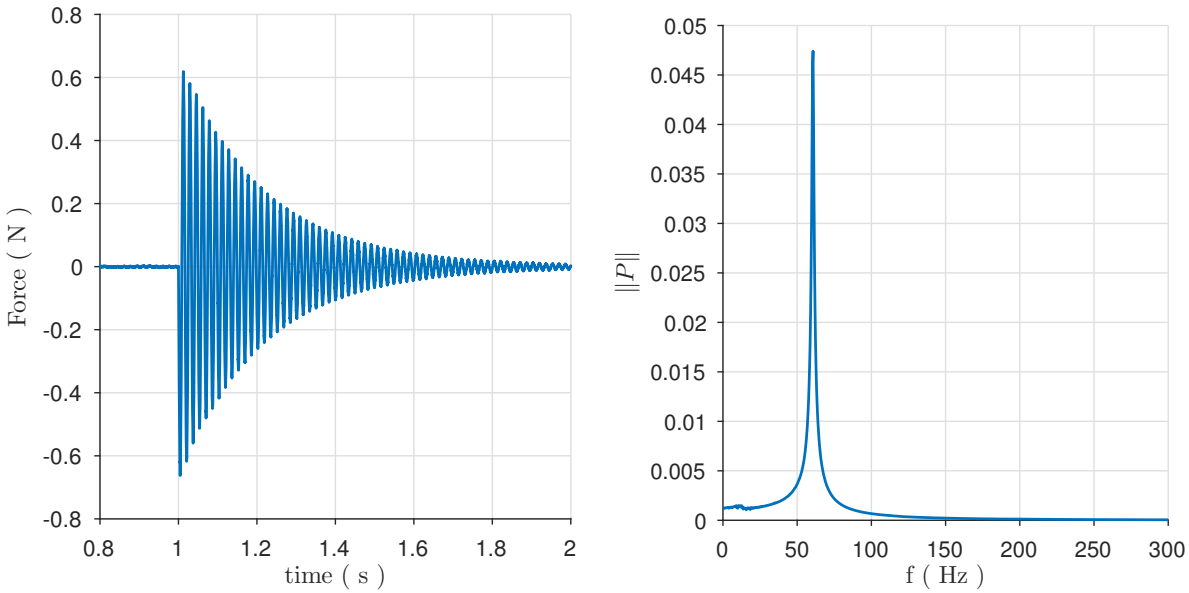

(a) Time response of impact excitation at $t = 1$

(b) Frequency domain of the measured impact response

Figure D.2: Frequency analysis of the eigenfrequency of the static set-up

E

Stator fabrication

The in-house built of an induction machine has proven no easy feat. Below some of the steps taken in the production of the final stator is described.

As seen before the stator is build using a set of coils, a stator core and stator teeth. For the fabrication of the coils copper wire is used that has a thermal curable coating that allows for bonding of the wires. For the winding process a special jig was developed to allow for winding on the winding machine depicted in figure E.1b. It is found that a taper of 1.5° on the jig core allows for easy removal of the coils after curing.

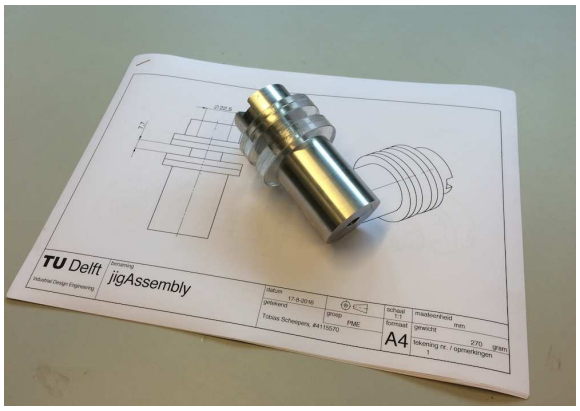

(a) Winding jig made for the stator coils

(b) Winding process on the winding machine

Figure E.1: Manufacturing of the stator coils on a winging machine

Once the coils (figure E.3a) are finishes they are mounted on the machined stator core in combination with the laser-cut stator teeth (figure E.3b) as depicted in figure E.2.

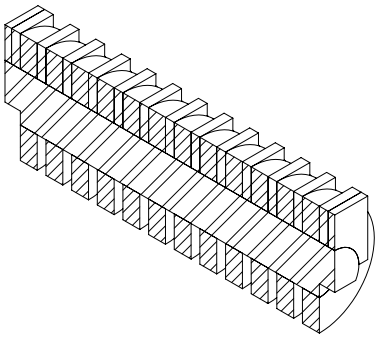

Figure E.2: Section of the stator assembly

(a) Stator coil

(b) Laser-cut stator teeth

Figure E.3: Stator components before assembly

Finally after fitting the stator assembly into the machined base a final step is performed to improve the thermal conductivity from the coils to the base. The base is filled using a gel-like resin with a high thermal conductivity. The top layer is covered using standard casting resin to mechanically fix the parts in place and avoid contamination of the gel-like resin.

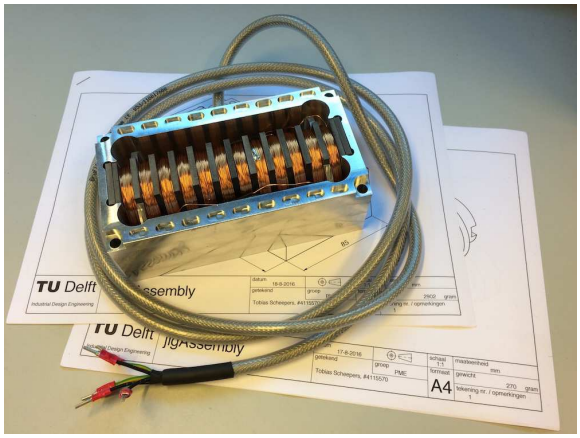

(a) Empty stator

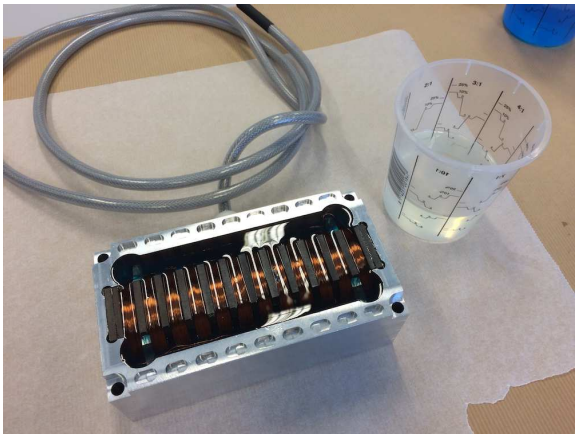

(b) Filled stator

Figure E.4: Filling of the stator using thermal resin for heat dissipation

F

Mechanical drawings

The most essential mechanical components fabricated for the different setups are shown below. The rotor encoder mount used in the dynamic set-up is shown below in more detail followed by a couple of the mechanical drawings used during production.

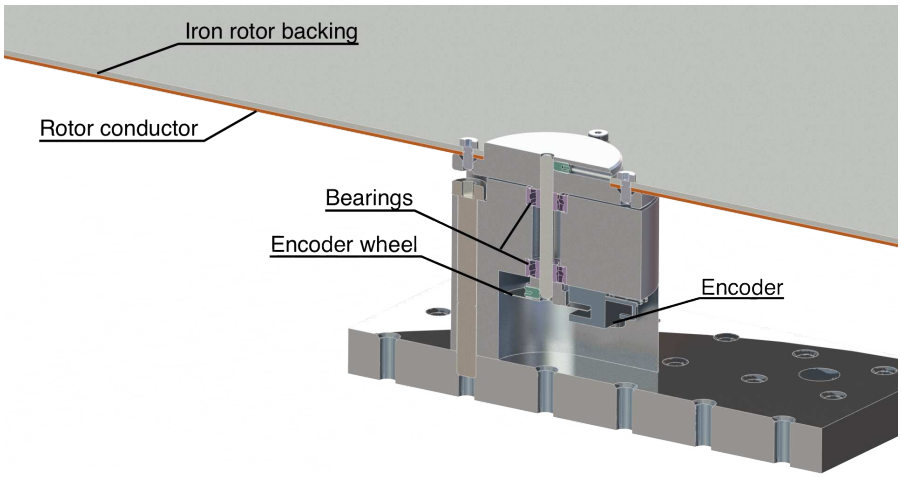

Figure F.1: Sectional view of the encoder mount of the dynamic set-up

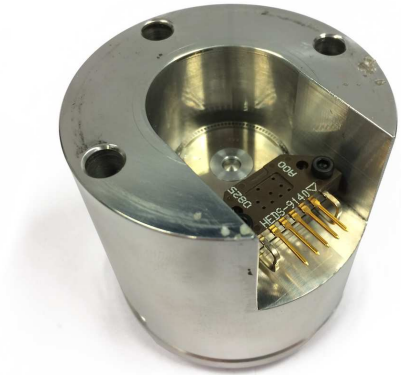

(a) Bottom view of physical encoder assembly

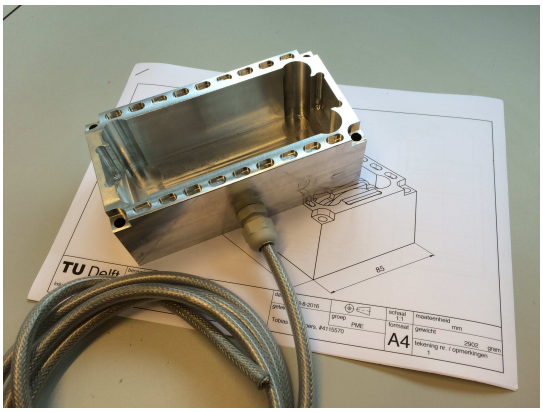

(b) Milled stator base

Figure F.2: Machined mechanical components after fabrication

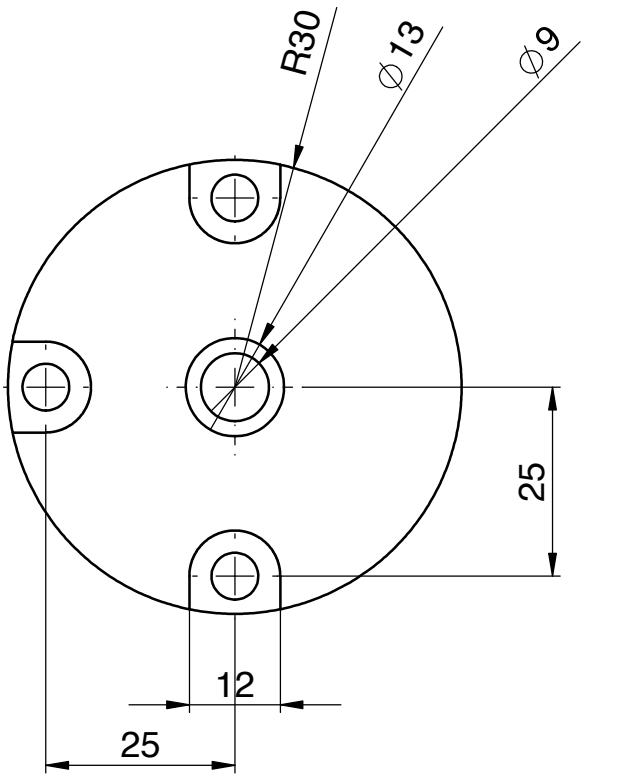

Mat.: 1060 Alloy
1

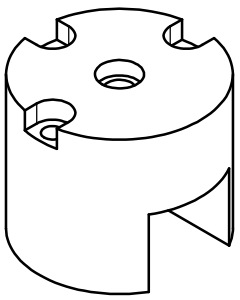

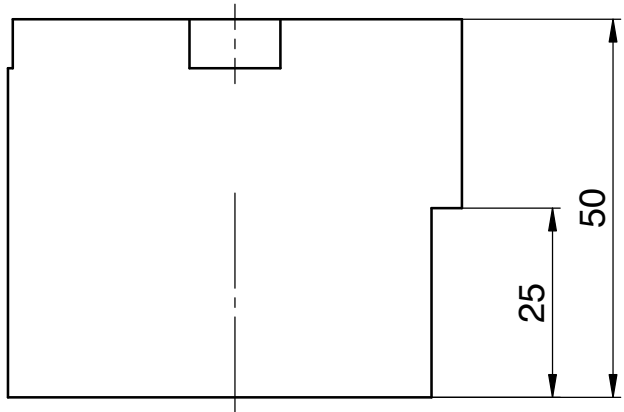

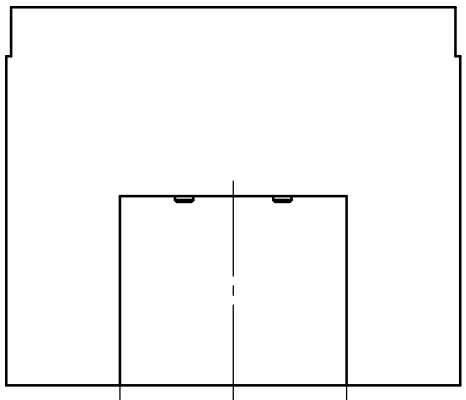

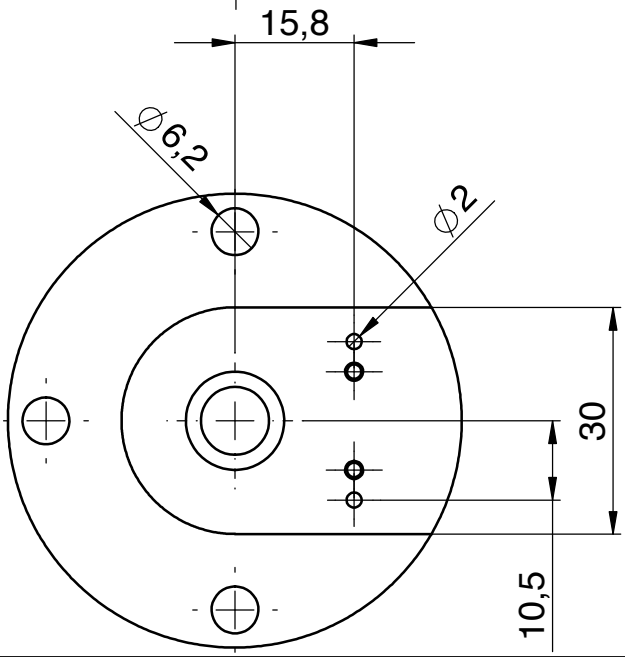

benaming **encoderMount**				maateenheid mm
			formaat A4	tekeningnummer 1
TU Delft Industrial Design Engineering	schaal 1:1	datum 1-12-2016	gewicht 277 gram	
	getekend Tobias Scheepers, #4115570			groep PME

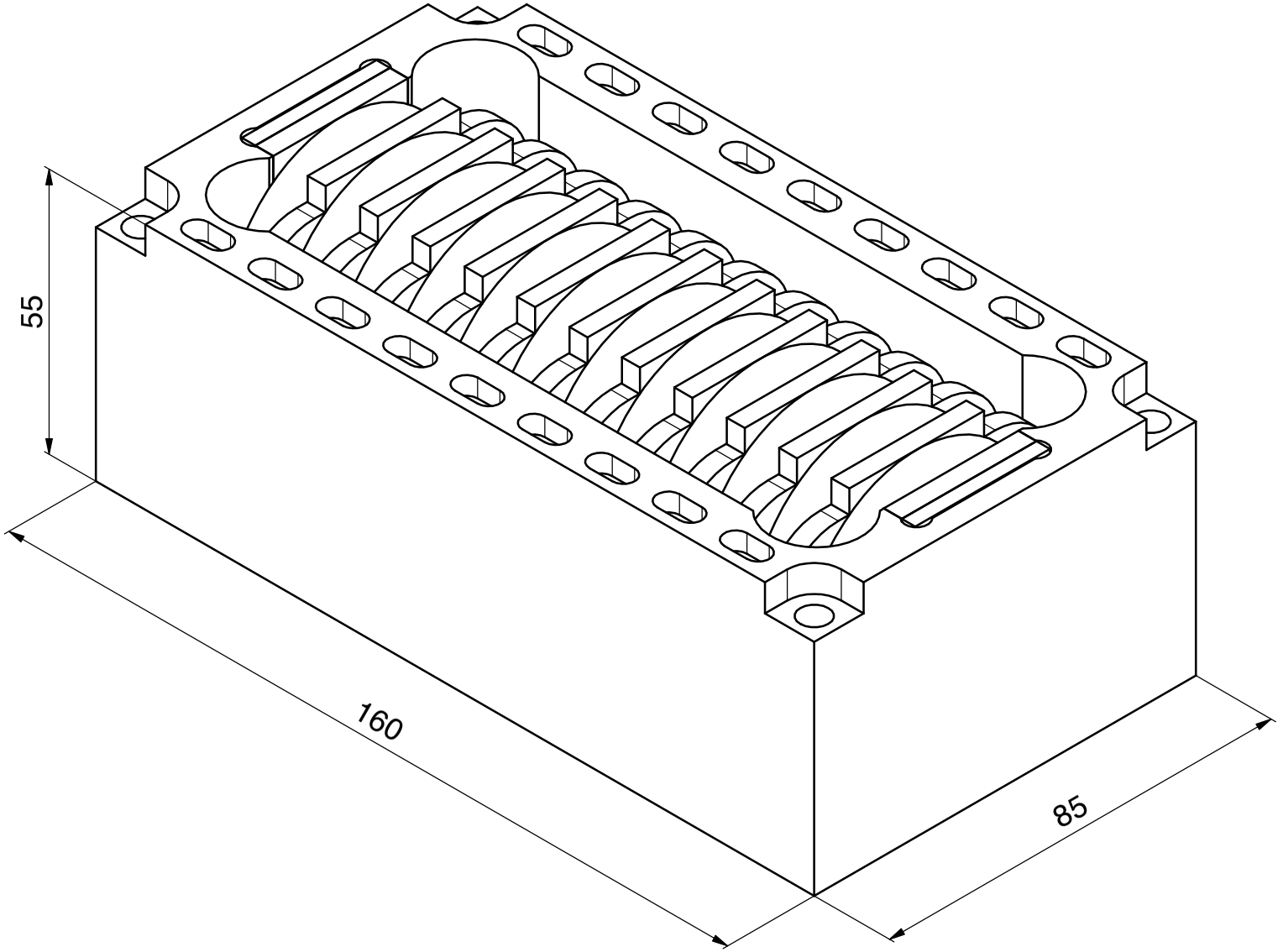

TU Delft Industrial Design Engineering	benaming slimAssembly	datum 18-8-2016		schaal 1:1	maateenheid mm
		getekend Tobias Scheepers, #4115570	groep PME	formaat A4	gewicht 2902 gram
					tekening nr. / opmerkingen 1

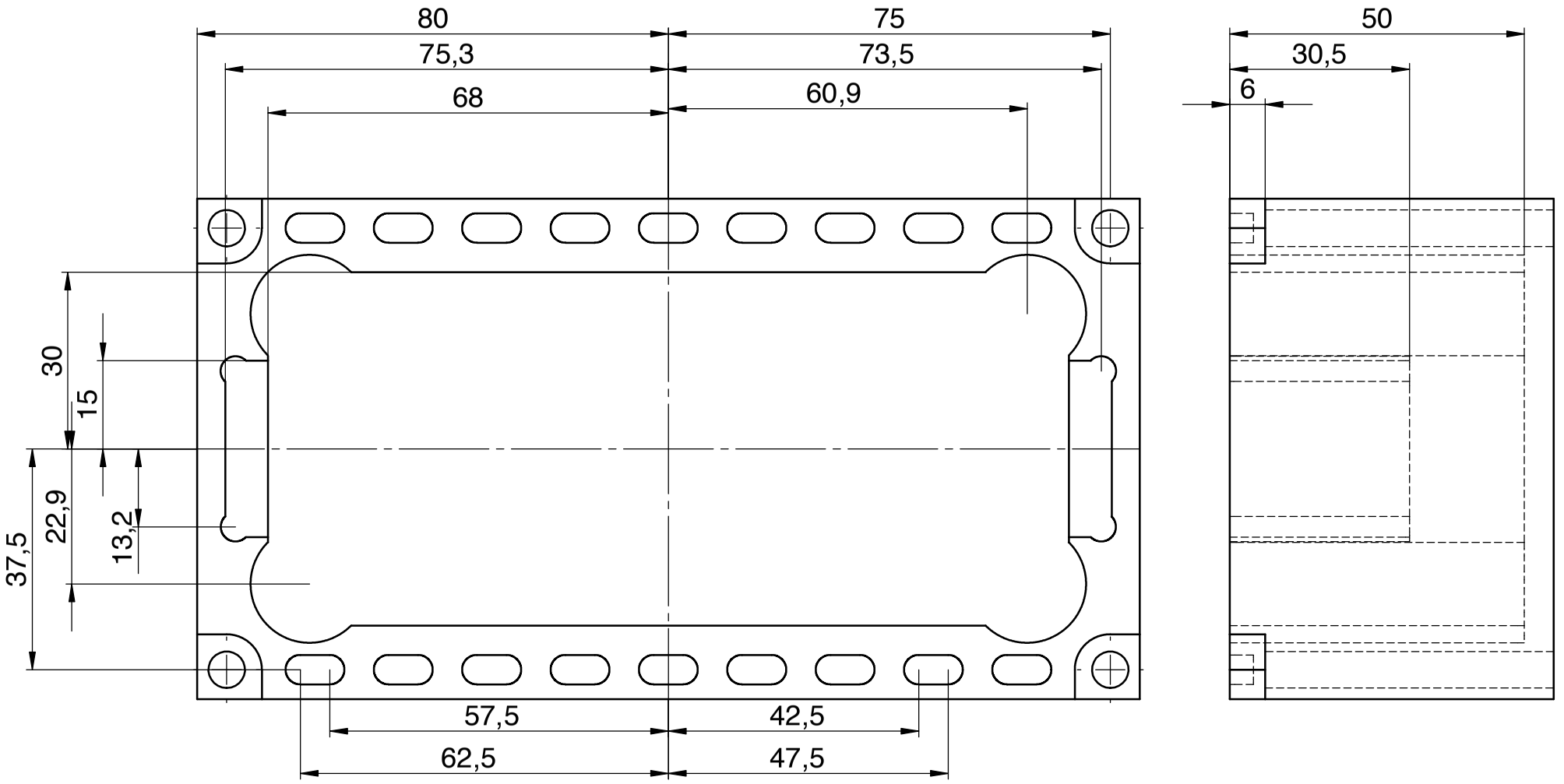

TU Delft Industrial Design Engineering	benaming slimAssembly	datum 18-8-2016		schaal 1:1	maateenheid mm
		getekend Tobias Scheepers, #4115570	groep PME	formaat A4	gewicht gram
					tekening nr. / opmerkingen 2

Bibliography

[1] Bjarni Bessason, Christian Madshus, Hans Arne Frøystein, and Henning Kolbjørnsen. Vibration criteria for metrology laboratories. *Measurement science and technology*, 10(11):1009, 1999.

[2] M. Binnard. Planar motor with linear coil arrays, September 3 2002. URL `https://www.google.com/patents/US6445093`. US Patent 6,445,093.

[3] A. Boglietti, A. Cavagnino, M. Lazzari, and M. Pastorelli. Predicting iron losses in soft magnetic materials with arbitrary voltage supply: an engineering approach. *IEEE Transactions on Magnetics*, 39(2):981–989, Mar 2003. ISSN 0018-9464. doi: 10.1109/TMAG.2003.808599.

[4] H Bolton. Transverse edge effect in sheet-rotor induction motors. In *Proceedings of the Institution of Electrical Engineers*, volume 116, pages 725–731. IET, 1969.

[5] Bimal K Bose. *Modern Power Electronics and AC Drives*. Pearson Prentice Hall Computin, 2001. ISBN 0130167436. URL `http://www.ebook.de/de/product/3658021/bimal_k_bose_modern_power_electronics_and_ac_drives.html`.

[6] S.N.Mahendra Subrahmanyam Maddula Chandan Kumar, R.K.Shrivastava. Comparison of analytical mmethod of analysing linear induction motors. 2013.

[7] Surajit Chattopadhyay, Madhuchhanda Mitra, and Samarjit Sengupta. Harmonic assessment by area based technique in clarke and park planes. In *Electric Power Quality*. Springer, January 2011. ISBN 978-94-007-0634-7. doi: 10.1007/978-94-007-0635-4_15. URL `http://dx.doi.org/10.1007/978-94-007-0635-4_15`.

[8] Rik De Doncker, Duco WJ Pulle, and André Veltman. *Advanced electrical drives: analysis, modeling, control*. Springer Science & Business Media, 2010.

[9] P. Dittrich and D. Radeck. 3 - dof planar induction motor. In *2006 IEEE International Conference on Electro/Information Technology*, pages 81–86, May 2006. doi: 10.1109/EIT.2006.252173.

[10] W. C. Duesterhoeft, M. W. Schulz, and E. Clarke. Determination of instantaneous currents and voltages by means of alpha, beta, and zero components. *Transactions of the American Institute of Electrical Engineers*, 70(2):1248–1255, July 1951. ISSN 0096-3860. doi: 10.1109/T-AIEE.1951.5060554.

[11] J Duncan. Linear induction motor-equivalent-circuit model. 130(1):51–57, 1983.

[12] EM Freeman and C Papageorgiou. Spatial fourier transforms: A new view of end effects in linear induction motors. 125(8):747–753, 1978.

[13] N. Fujii and M. Fujitake. Two-dimensional drive characteristics by circular shaped motor. In *Conference Record of 1998 IEEE Industry Applications Conference. Thirty-Third IAS Annual Meeting (Cat. No.98CH36242)*, volume 1, pages 167–173 vol.1, Oct 1998. doi: 10.1109/IAS.1998.732278.

[14] Nobuo FUJII and Toru KIHARA. Surface induction motor for two-dimensional drive. *IEEJ Transactions on Industry Applications*, 118(2):221–228, 1998.

[15] Nobuo Fujii, Yasuaki Sakamoto, and Takeshi Kayasuga. Effect of magnet rotator type compensator for linear induction motor for new urban subway. *International Journal of Applied Electromagnetics and Mechanics*, 15(1-4):169–174, 2001.

[16] Kamel Idir, Graham E Dawson, and Anthony R Eastham. Modeling and performance of linear induction motor with saturable primary. *IEEE transactions on industry applications*, 29(6):1123–1128, 1993.

[17] Texas Instruments. Scalar (v/f) control of 3-phase induction motors. Technical report, 2013.

[18] Texas Instruments. Instaspin-foc^{TM} and instaspin-motion^{TM}. Technical report, 2013.

[19] J. W. Jansen, C. M. M. van Lierop, E. A. Lomonova, and A. J. A. Vandenput. Ironless magnetically levitated planar actuator. *Journal of Applied Physics*, 103(7):07E905, 2008. doi: 10.1063/1.2832310. URL `http://dx.doi.org/10.1063/1.2832310`.

[20] Andrew Peter Johnson. *High speed linear induction motor efficiency optimization*. PhD thesis, Cambridge, Massachusetts; Massachusetts Institute of Technology, 2005.

[21] Kwang Suk Jung and Yoon Su Baek. Study on a novel contact-free planar system using direct drive dc coils and permanent magnets. *IEEE/ASME Transactions on Mechatronics*, 7(1):35–43, Mar 2002. ISSN 1083-4435. doi: 10.1109/3516.990885.

[22] Sinisa Jurkovic. Induction motor parameters extraction. *Michigan State University*, 2007.

[23] Masaaki Kumagai and Ralph L. Hollis. Development and control of a three dof spherical induction motor. In *ICRA*, 2013.

[24] Eric R Laithwaite. Linear electric machines - a personal view. *Proceedings of the IEEE*, 63(2):250–290, 1975.

[25] Eric Roberts Laithwaite. *Transport without wheels*. 1977.

[26] Barnes Malcolm. Practical variable speed drives and power electronics. *Primera edicion*, 2003.

[27] M Mirsalim, A Doroudi, and JS Moghani. Obtaining the operating characteristics of linear induction motors: A new approach. *IEEE Transactions on magnetics*, 38(2):1365–1370, 2002.

[28] B Srinu Naik. Comparison of direct and indirect vector control of induction motor. *International Journal of New Technologies in Science and Engineering (IJNTSE)*, 1(1):110–131, 2014.

[29] SA Nasar and L Del Cid. Certain approaches to the analysis of single-sided linear induction motors. In *Proceedings of the Institution of Electrical Engineers*, volume 120, pages 477–483. IET, 1973.

[30] S Nonaka and N Fujii. Simplified two-dimensional analysis of linear induction motors. *IEEE Transactions on Magnetics*, 23(5):2832–2834, 1987.

[31] Paul Ouwehand. Novel nanometer precision planar positioning stage using pre-sliding friction. Master's thesis, Delft University of Technology, Department of Precision and Microsystems Engineering, 2015.

[32] R. H. Park. Two-reaction theory of synchronous machines generalized method of analysis-part i. *Transactions of the American Institute of Electrical Engineers*, 48(3):716–727, July 1929. ISSN 0096-3860. doi: 10.1109/T-AIEE.1929.5055275.

[33] Marcello Pucci. Direct field oriented control of linear induction motors. *Electric Power Systems Research*, 89:11–22, 2012.

[34] D.W.J. Pulle, P. Darnell, and A. Veltman. *Applied Control of Electrical Drives: Real Time Embedded and Sensorless Control using VisSimTM and PLECSTM*. Power Systems. Springer International Publishing, 2015. ISBN 9783319200439. URL `https://books.google.nl/books?id=NImQCgAAQBAJ`.

[35] B.A. Sawyer. Magnetic positioning device, July 22 1969. URL `https://www.google.nl/patents/US3457482`. US Patent 3,457,482.

[36] R Munnig Schmidt, Georg Schitter, and Adrian Rankers. *The Design of High Performance Mechatronics-: High-Tech Functionality by Multidisciplinary System Integration*. IOS Press, 2014.

[37] A. H. Selcuk and H. Kurum. Investigation of end effects in linear induction motors by using the finite-element method. *IEEE Transactions on Magnetics*, 44:1791–1795, July 2008. doi: 10.1109/TMAG.2008.918277.

[38] Abbas Shiri and Abbas Shoulaie. Design optimization and analysis of single-sided linear induction motor, considering all phenomena. *IEEE transactions on energy conversion*, 27(2):516–525, 2012.

[39] Michael A Soltz, Y.Lawrence Yao, and Jehuda Ish-Shalom. Investigation of a 2-d planar motor based machine tool motion system. *International Journal of Machine Tools and Manufacture*, 39(7):1157 – 1169, 1999. ISSN 0890-6955. doi: http://dx.doi.org/10.1016/S0890-6955(98)00085-6. URL http://www.sciencedirect.com/science/article/pii/S0890695598000856.

[40] F. Tahri, A. Tahri, E. A. AlRadadi, and A. Draou. Analysis and control of advanced static var compensator based on the theory of the instantaneous reactive power. In *Electrical Machines and Power Electronics, 2007. ACEMP '07. International Aegean Conference on*, pages 840–845, September 2007. doi: 10.1109/ACEMP.2007.4510559.

[41] F. Treviso, M. A. Da Silveira, A. F. F. Filho, and D. Dorrell. An induction planar actuator for surface inspection. In *2015 IEEE Magnetics Conference (INTERMAG)*, pages 1–1, May 2015. doi: 10.1109/INTMAG.2015.7157679.

[42] Felipe Treviso, Marilia A. Silveira, Aly F. Flores Filho, and David G. Dorrell. Theoretical and experimental analysis of an induction planar actuator with different secondaries - a planar driver application for metallic surface inspection. *Sensors*, 16(3):407, 2016. ISSN 1424-8220. doi: 10.3390/s16030407. URL http://www.mdpi.com/1424-8220/16/3/407.

[43] J. Wesselingh. *Contactless Positioning Using an Active Air Film*. Technical University of Delft, 2011. ISBN 9789090264370.

[44] Sakae Yamamura. Theory of linear induction motors. *New York, Halsted Press, 1979. 246 p.*, 1979.